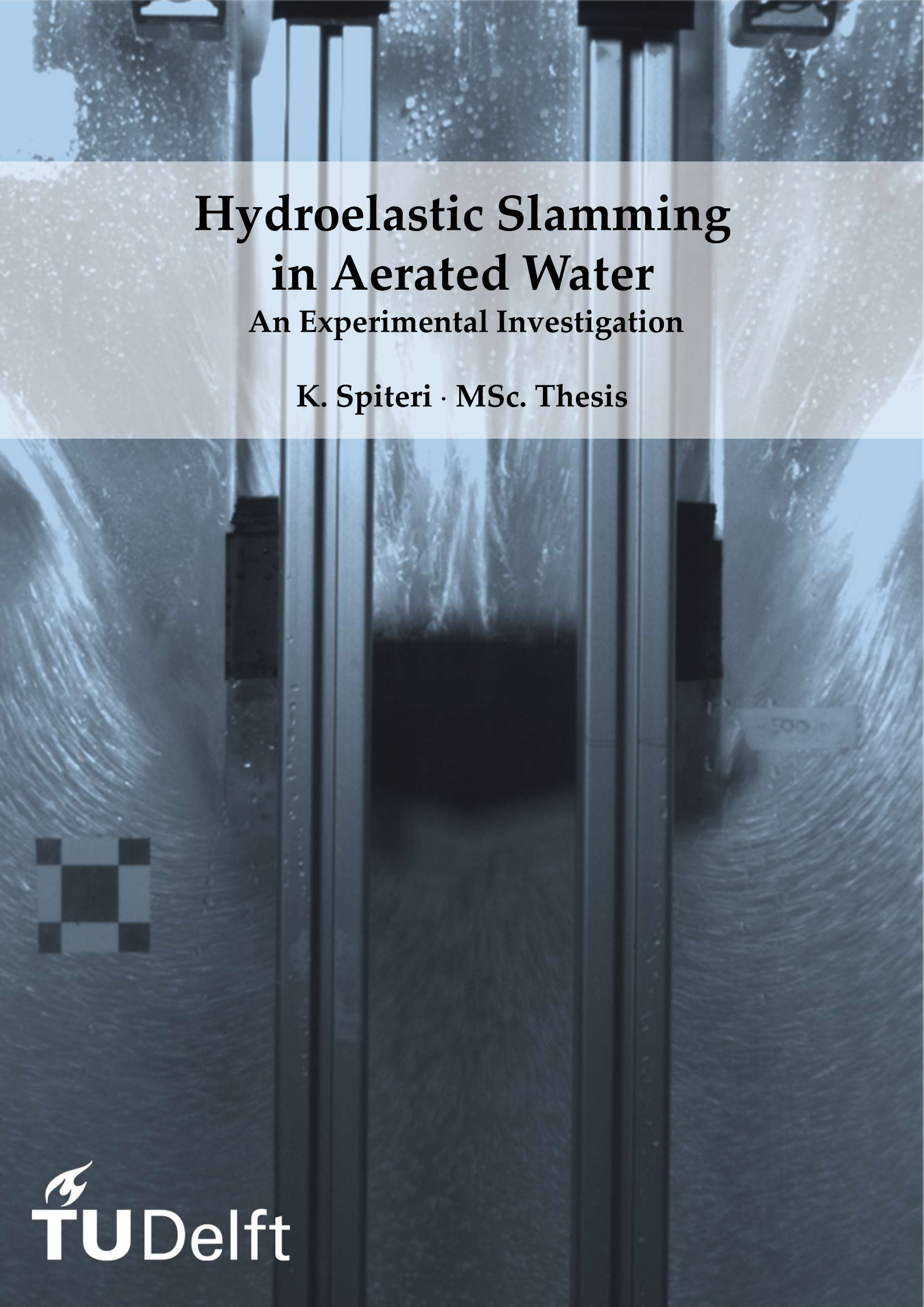

Hydroelastic Slamming in Aerated Water

An Experimental Investigation

K. Spiteri · MSc. Thesis

TU Delft

Thesis for the degree of MSc in Marine Technology
in the specialization of *Ship and Offshore Structures (SAOS) / Ship Hydromechanics (SH)*

Hydroelastic Slamming in Aerated Water - An Experimental Investigation

By

Kurt Spiteri

This thesis (**MT.25/26.002.M**) is classified as confidential in accordance with the general conditions for projects performed by the TUDelft.

Date of Exam: 26.09.2025
Faculty of Mechanical Engineering, Delft University of Technology

Thesis Exam Committee:

Chair:	Dr.ir. P.R. Wellens
Committee Members:	Dr. A. Grammatikopoulos
	Ir. M.M. Bockstael
	B. Font PhD
	Dr. A.M. Aragón

Author details:

Student number: 5914663

Abstract

Maritime vessel slamming into aerated water is a significant area of study for high speed and lightweight craft. Upon impact with water, safety risks can lead to structural failures, endangering human life and resulting in economic losses. The design must be optimised for material usage with appropriate safety factors based on accurate knowledge of the loading and response under several impact conditions. Structural flexibility makes hydroelastic effects unavoidable, with the magnitude governed by impact type, velocity, and structure geometry. Entrained air from free-surface breaking renders the water weakly compressible, further altering the slamming dynamics. This work presents a physical foundation and experimental dataset for validating numerical models of more realistic impact conditions.

In this work, a novel experiment was set up for a combined evaluation of hydroelastic slamming in aerated water. A wedge with a 15° deadrise angle was designed and constructed to represent ship bow slamming. The wedge bottom consisted of interchangeable steel plates of varying stiffness. Contact and optical measurement techniques were used to capture and visualise the loading and response over the plate width. Experimental test conditions include plate thicknesses between 1 and 3 mm, impact velocities between 2 and 5 m/s and an air fraction in water between 0 and 2%.

The results show that structural stiffness and impact velocity, captured by the hydroelasticity factor R_F jointly govern the slamming response. The air fraction in water redistributes impulsive loads over time and modifies the wetted natural frequency through the influence of water density. For high-velocity impacts with significant plate deformation, as well as for impacts approaching the quasi-static regime, a lower peak strain was found for impacts in aerated water. Furthermore, for the condition where the wetting time approaches the first wetted natural period of the structure, response amplification due to hydroelastic effects was observed, with a further increase in load for the aerated water condition. This study demonstrates that aeration can amplify structural response, making it essential to take into account the physical aeration effects in the design of ship plating for slamming conditions. The structural response was found to capture the underlying physical behaviour more reliably than the pressure measurements alone. The effects of the small-scale experimental setup on the results were also identified and documented in detail.

Acknowledgements

This thesis marks a culmination of my journey at TU Delft over the past two years. The project would not be possible without several individuals to whom I am deeply grateful. First, I want to thank my supervisor Peter Wellens for your guidance and expertise in the field of hydroelastic slamming, for always being available to help with technical and practical matters, and for sharing my curiosity and enthusiasm for the project throughout our meetings. I would like to thank all the staff at the Ship Hydromechanics laboratory for your help and support with setting up the experiments and the instrumentation system, and for your interest in the project. To my friends in Delft, thank you for your companionship, all the good times we've shared, and for making these years both memorable and meaningful. To my girlfriend Mikela, thank you for your unwavering support and for always being there, no matter the distance. Finally, I owe my deepest gratitude to my parents Robert and Antoinette, who have instilled in me the values of discipline, hard work, resilience and humility.

I hope that you enjoy reading my report.

Kurt Spiteri

Delft, September 2025

GOVERNMENT
OF MALTA

FONDI.eu

The research work disclosed in this publication is partially funded by the Endeavour II Scholarships Scheme. The project is co-funded by the ESF+ 2021-2027

Co-funded by
the European Union

ENDEAVOUR
SCHOLARSHIPS SCHEME

Contents

List of Figures

List of Tables

Nomenclature

Symbol	Description	Unit
A_{nn}	Added mass coefficient for mode n	kg
D	Flexural rigidity	$\mathrm{N{\cdot}m^2}$
E	Young's modulus	Pa
g	Acceleration due to gravity	$\mathrm{m/s^2}$
h	Drop height wrt. the undisturbed water level.	m
I	Section moment of inertia	$\mathrm{m^4}$
K_{nn}	Structural stiffness coefficient for mode n	N/m
L	Plate length	m
M	Mass of plate	kg
P	Pressure	Pa
P_n	Pressure sensor numbering (1–3) (chine - keel)	-
R	Hydroelasticity factor (general)	-
R_F	Hydroelasticity factor from Faltsinsen	-
R_S	Hydroelasticity factor from Stenius	-
R_Ω	Electrical resistance	Ω
T_{LP}	Structure loading period (same as t_w)	s
T_{NP}	Structural first wetted natural period (same as T_w)	s
T_w	First wetted natural period	s
V_i	Impact velocity	m/s
V_o	Excitation voltage across bridge	V
V_{in}	Output voltage from bridge	V
$a_n(t)$	Modal amplitude for mode n	m
t	Time	s
t_{in}	Time at light gate rising signal	s
t_{out}	Time at light gate falling signal	s
t_p	Plate thickness	m
t_w	Structure wetting time	s
$w(x', y', t)$	Deformation of the plate in z'	m
$\overline{w}_{,t}$	Mean velocity of the deforming plate surface	m/s
x	Absolute Cartesian spatial coordinate	m
x'	Cartesian spatial coordinate aligned with plate	m
α	Deadrise angle of wedge	$^\circ$
α_{gf}	Strain gauge temperature correction factor	1/K
β_g	Gas (air) volume fraction in water	-
β_n	Wavenumber for mode n	1/m
Δ	Change	-
γ	Ratio R_S/R_F	-
ε	Strain	-
ε_m	Measured strain (no temperature correction)	-
ε_c	Corrected strain gauge measurement	-

Symbol	Description	Unit
ε_s	Thermal output polynomial strain influence	-
ε_f	Temperature coefficient mismatch influence	-
ε_{exp}	Final corrected experimental strain	-
ν	Poisson's ratio	-
ρ	Density (general)	kg/m^3
ρ_w	Density of water	kg/m^3
ρ_a	Density of air	kg/m^3
σ	Standard deviation	-
f_{hs}	Hydro-structural natural frequency	Hz
$f_{he,n}$	Hydroelastic natural frequency, mode n	Hz
Ma_{edge}	Edge Mach number	-
μ_{NP}	Wetted natural period boundary condition factor	-
$\overline{m}$	Plate structural mass	kg
$\overline{m}_a$	Uniformly distributed added mass	kg
c_f	Speed of sound in aerated water	m/s
c_a	Speed of sound in air	m/s
c_l	Speed of sound in liquid (water)	m/s
$\Psi_n(x)$	Mode shape function	-

Abbreviation	Meaning
S.G.	Strain Gauge
G.F.	Strain Gauge Factor
DIC	Digital Image Correlation
DAQ	Data Acquisition System
DAF	Dynamic Amplification Factor
DoF	Depth of Field
ICP	Integrated Circuit Piezoelectric (sensor type)
NI	National Instruments
FPS	Frames Per Second
FvK	Föppl–von Kármán plate theory
SA-Z	Photron FASTCAM SA-Z high-speed camera
PCB	PCB Piezotronics (sensor manufacturer)
RSD	Relative Standard Deviation
TB	Terminal Block (NI module)

1 Introduction

1.1 Overview

Water slamming is a complex fluid-structure interaction (FSI) phenomenon that occurs due to high relative motions between a structure and the surface of a body of water over a very short time period [26]. Understanding and mitigating the effects of slamming and extreme water impacts is necessary to ensure the structural integrity and operational safety of maritime vessels and offshore structures in unpredictable sea conditions. Water impact events consist of a complex interaction of free surface and hydrodynamic effects with structural dynamics [69, 94]. Entrapped air pockets can cause a vibratory response leading to various structural damages, including indentation or rupture of shell plating, buckling or detachment of supporting members, and deformation of main structures [35]. For maritime vessels, these damages can cause flooding in certain compartments, destruction of equipment or deck houses located near the bow, or failure of mooring systems, which can have further serious consequences for the vessel and to the detriment of human life [105].

Dias and Ghidaglia [21] characterize slamming scenarios as either (1) water entry problems or (2) wave breaking against a structure. In the former case, a body moving at a velocity interacts with the water surface, as is the focus of this research. In the latter case, the kinetic energy results from a liquid with high velocity interacting with a structure. In the context of maritime vessels, examples of severe water impacts include bow slamming of high-speed craft [1], wet deck slamming in catamarans [18], free-fall lifeboats undergoing large deceleration when entering the water [6]. Wave breaking against structures includes sloshing in liquid cargo containers [21], green water on deck hitting a superstructure [7] and waves breaking against offshore platforms [10, 114]. Violent water impacts are also highly relevant for offshore wind turbines [40], wave energy converters [33], breakwaters, sea walls, coastal sea defences [21], and offshore bridges [110]. Further applications of slamming include aeronautical cases such as water landings [21]. Historically, wave loads have compromised maritime structures [2] and have caused failure [30, 109]. In the maritime context, wave loads have also led to loss of life [42, 60, 101].

During such violent impact events, the complex configuration of the free surface can cause air and water interaction such that air is entrained and large air pockets are entrapped. By entrapping an air pocket between the water and the structure, the pocket can have a cushioning effect on the peak pressure [8, 83]. On the other hand, the pressure oscillations in the air pocket can increase pressure levels on the structure being impacted, increase the force acting on the structure during wave impact and induce resonant fluid-structure interaction [8, 67, 69]. The latter phenomena can have severe consequences on structural integrity and lifespan. Consequently, the physics of compressibility is also highly relevant in problems of wave impacts on maritime structures [98]. The structural implications of such aerated water impacts have not been studied explicitly, introducing additional uncertainties in this regard. Standard design practices do not account for slamming into aerated water [19, 20]. This may result in over-engineering due to load over-estimation or unanticipated catastrophic failure due to a lack of knowledge of combined effects. As highlighted previously, understanding the physical effects of violent wave impacts on offshore structures is crucial for improving design and safeguarding human life. Consequently, this knowledge will result in more robust maritime structures capable of higher performance, longer structure functional lifetimes and higher safety for humans on board. The additional complexity in analysing water-wave impacts due to entrained air is the starting point of this thesis.

Hydroelastic slamming and impacts into aerated water have been treated separately due to the inherent physical complexity [92]. A systematic literature study has indicated that the relative importance of certain physical effects is usually assumed to be negligible, depending on the scope of the work. The combined effects of structural deflection and fluid compressibility due to aeration are therefore

not well understood. The combined effects of the physics can potentially result in higher loading on the structure. The main objective of this research is therefore to bridge the gap between these two fields and to evaluate the combined hydrodynamic and structural effects in the context of a ship bow slamming into the water represented by a wedge-like structure. Furthermore, this study aims to determine if any distinction of the effects of structural flexibility and water compressibility on a maritime structure in a slamming condition can be made. As per van der Eijk and Wellens [95] a combination of analytical, experimental and numerical modelling approaches must be used due to the complexity of physical phenomena and the interdependency of these approaches for developing physical insight, verification and validation. The present study serves as the first step to the interdependent approach through addressing the experimental component.

1.2 Thesis Outline and Report Structure

The subsequent chapters of the thesis are organised as below:

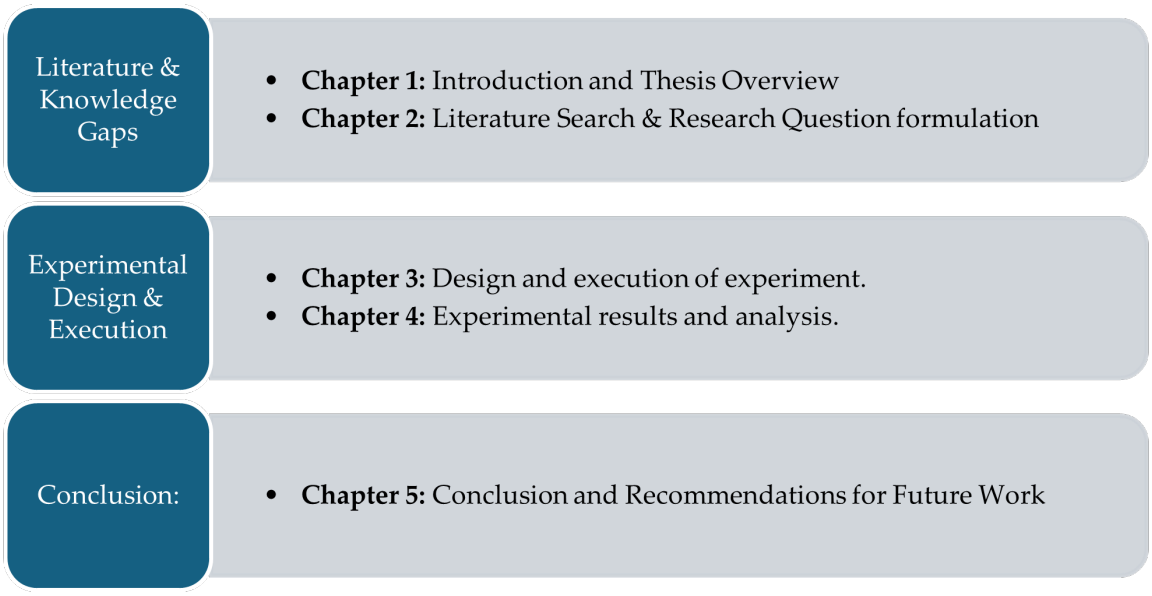

Figure 1: Overall project structure and organisation.

2 Literature Review

The first part of the literature review provides an overview of the physical phenomena that occur during wave impacts on a flexible structure. First, slamming into aerated water and hydroelasticity are addressed separately in Sections 2.1 and 2.2 respectively. The challenges associated with combining the two effects are then identified in Section 2.3, leading to the novelty addressed in this thesis.

2.1 Presence of Air in Water

2.1.1 Entrapped Air

Air entrapment occurs when a pocket of air is enclosed between a body of water and a structure due to a breaking wave impact [111], as per Figure 2, or due to the overtopping of breaking waves and subsequent splashes [47] as shown in Figure 3.

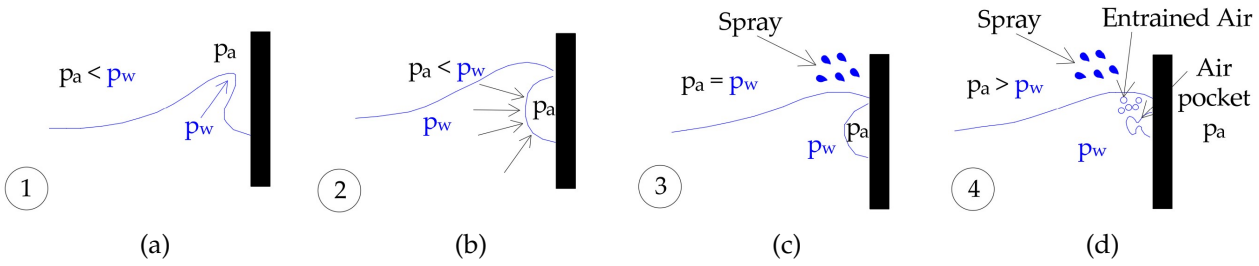

Figure 2: Inclusion of air during (rigid) structure interaction. Adapted from Wemmenhove [111].

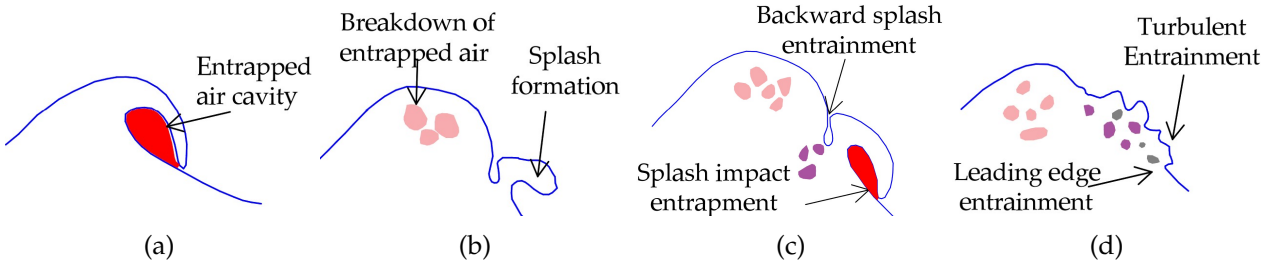

Figure 3: Inclusion of air during breaking waves. Adapted from Kiger and Duncan [47].

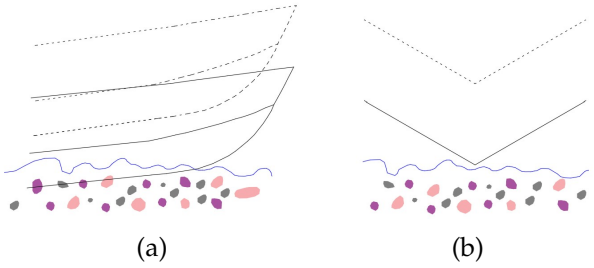

Figure 4: Visualizations of ship slamming into aerated water from the (a) side and (b) front.

2.1.2 Entrained Air

Air entrainment occurs when air bubbles are dispersed through the water. The mixture of air bubbles and water is referred to as aerated water [47]. As the jet from the plunging breaking wave in Figure 3a drags air into the water, the entrapped air breaks down and entrainment occurs, as shown in Figure 3b. Subsequent impacts of the forward splashes will also result in entrapment, as shown in Figure 3c. The backside of the splash and the upper surface of the plunging jet can also cause additional entrainment. Furthermore, shown in Figure 3d, air is entrained throughout the breaking

regions when the wave surface fragments into ligaments and droplets, particularly in highly energetic or long-wavelength waves. Additionally, air is entrained at the leading edge of the turbulent breaking region during the later stages of the breaking process. The air collapse mechanics for entrained air formation are also visible in Figure 2d, where the air pocket is unstable and collapses into smaller bubbles [111]. Other processes generating air bubbles in water are biological production and decomposition of organic compounds, white capping and air entrainment by capillary waves [47, 54].

The Hinze scale is a critical threshold in turbulent flows such as breaking waves, distinguishing two bubble formation mechanisms and the associated bubble size [17]. The scale depends on the turbulent dissipation rate and the fluid properties, and is useful to compare air bubble creation and size in laboratory and oceanic conditions. Bubbles larger than the Hinze scale are formed by turbulent fragmentation, and bubbles of smaller size are formed by jet/drop impacts.

Aeration measurements for full-scale wave impacts on a breakwater in the Atlantic Ocean by Bullock et al. [11] reported values of up to 14.4 % air content in the vicinity of the water surface. Air bubble retention was found several wave time periods after impact. Deane and Stokes [17] have measured bubble size and distribution for breaking waves in the open sea, and found that the generated dense bubble plumes that can penetrate over 0.5 m beneath the surface, with air void fractions exceeding 10%. Bubbles were found to vary in size from micrometre scale to centimetre scale. Consequently, for a maritime structure slamming into water, as per the schematic in Figure 4, aeration will be present and requires further evaluation. The slamming interaction will in itself generate further air entrapment and entrainment.

2.1.3 Physical Relevance

Entrapped air had a cushioning effect on a hydrodynamic impact, where the pressure peak is reduced. The air pocket will interact with the surrounding fluid through pulsating motions [67]. Experimental testing of moving structures on aerated water [57, 58] show that the compressibility of aerated water can cause a lower peak load but a higher load duration in comparison to an equivalent incompressible case. The change in aeration was also found to have a more pronounced effect on the peak pressure loading rather than on the impulse. A small amount of aeration can have significant effects on water compressibility [112]. The compressibility also allows for the generation of density waves. van der Eijk and Wellens [98] define a density wave as short-period oscillations of density and pressure propagating through the mixture with the speed of sound. The reflection of density waves can lead to additional loading oscillations and resonance.

2.1.4 Challenges

Scaling

Challenges in reproducing compressible effects with experimental studies of aeration at small-scale were anticipated by van der Eijk [96]. The level of aeration increases with scale. Current scaling laws are limited with reproducing entrained air effects at full scale. Froude scaling, which accounts for inertial and gravitational forces but neglects viscosity, surface tension, and air effects overestimates forces in small models by more than 10% due to increased aeration at larger scales. To address compressibility, Cauchy scaling considers inertial and elastic forces, but maximum pressure is underestimated and the rise time is overestimated, failing to conserve pressure impulse [11].

Air Distribution

In practical conditions, air bubbles would have different diameters and the distribution would not

be homogeneous due to the dynamic nature of breaking waves. In addition, at higher values of aeration, the air bubbles can affect each other. To simplify the problem, the percentage of aeration in the water must be a carefully controlled experimentally and used as an input to the numerical simulations [92]. Furthermore, air bubbles are three-dimensional. However, numerical simulations of aeration are often conducted in 2D due to computational efficiency [5, 98]. Dissipation effects on pressure oscillation amplitudes are inherently present experimentally and challenging to reproduce numerically [98].

2.2 Hydroelasticity

2.2.1 Overview and Classification

Maritime structures are inherently flexible. Hydroelasticity occurs due to coupled interaction between a flexible deformable structure and a water surface [23, 35, 72]. On impact, structural deflection results in vibrations which cause pressure oscillations [38, 45]. The interaction between the structural dynamics and the hydrodynamic loading of a slamming event depends on the impact velocity, deadrise angle and structural stiffness [35].

The time scale of the structural response serves as an indication of the relevant physics governing a slamming interaction of an elastic structure. The dimensionless Dynamic Amplification Factor (DAF) is used to this extent. This is a ratio of the real and the quasi-static structure response, where no coupling between the loading and the response is considered in the latter [35, 45]. The quasi-static response is defined by a DAF of unity. The DAF depends on the ratio between the wetted excitation time t_w and the characteristic first structural natural period of the structure in the water T_w [70, 86], with the relationship and interaction regimes shown in Figure 5. The quantity on the horizontal axis is a scaling. Different setups and impact scenarios will yield variations depending on the analytical theories used.

In the Impulsive interaction regime, there is a significant reduction of the structural response with respect to the quasi-static, and short-duration high pressures are filtered [23, 45]. In the dynamic regime, structural responses show an increase with respect to the quasi-static solution [45]. Finally, in the Quasi-Static regime, the response under hydrodynamic pressure loading is approximately equal to the static response for an equivalent rigid structure [61].

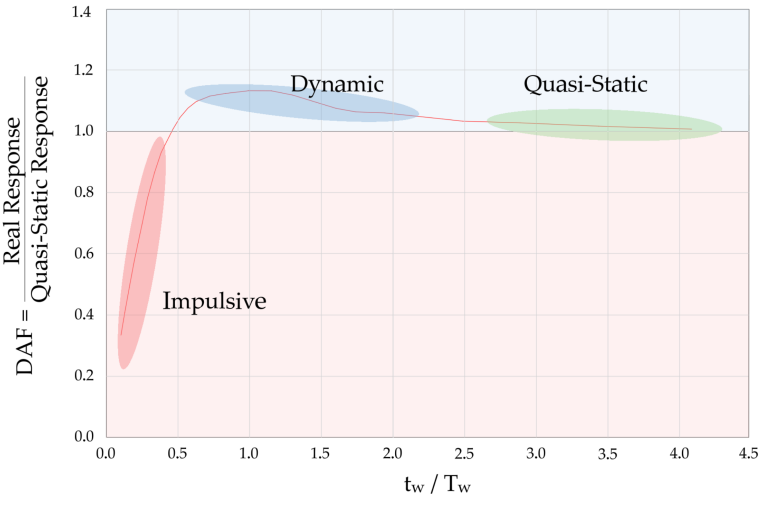

Figure 5: Hydroelastic interaction regimes. Adapted from Malenica et al. [61].

2.2.2 Hydroelasticity and the Free Surface

Hydroelastic interaction of a flexible structure under water impact and the corresponding vibrations can induce additional phenomena related to air entrapment and void formation [25, 35]. Consider the surface of a flexible structure as per Figure 6. Note that no boundary conditions are specified for the purpose of a visualisation of the physical phenomena. In Figure 6a, the structure is shown at time t after the initial point of impact with non-aerated water has occurred. At this stage, some deflection of the plate is already possible due to the inertia at this stage of the impact. Depending on properties such as the structural stiffness, impact velocity and deadrise angle, the following may occur:

i. No air effects

The entire wetted portion of the wedge stays in contact with the water, and no air is entrapped in between the solid and the fluid [74] as shown in Figure 6b, with some deflection being experienced. This response is only theoretically possible for stiff structures under low impact speeds.

ii. Void Formation

A low pressure cavity starts to form when the body surface is already in contact with the fluid [85]. Under certain conditions, the right edge of the beam can come in contact with the disturbed fluid flow before the plate is completely wetted [50]. A cavity is therefore produced and will collapse if no air enters. The cavity may occur due to the shape of the free surface, and can be enhanced by additional deflection due to hydroelasticity, shown in 6c. Panciroli et al. [75] also state that during very severe impact cases, successive pockets are generated and subsequently collapse, with the size of the pocket decreasing over time. Void formation can also affect the acceleration of the body [26].

iii. Ventilation

Ventilation occurs due to detachment of the fluid flow from the plate such that air entry occurs as shown in Figure 6d. An air cushion is therefore set up [74]. Faltinsen [23] attribute ventilation to large under-pressures under the plate during initial impact phases and low submergence, and in turn causes a reduction in the wetted length.

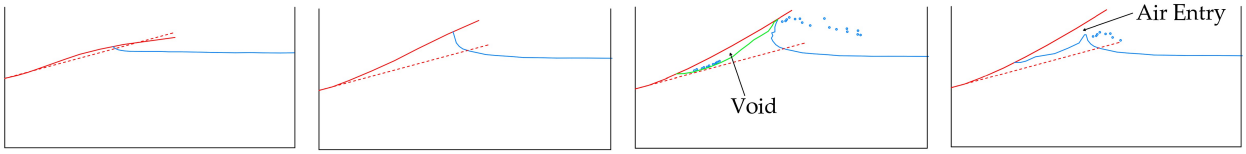

(a) Onset. (b) Attached. (c) Cavity entrapment. (d) Ventilation.

Figure 6: Interaction between air and free surface in hydroelastic slamming. The solid line represents deformed plate shape and the dashed line represents rigid plate. Adapted from experimental and numerical results of Panciroli et al. [75].

2.2.3 Cavitation

Franc and Michel [28] broadly define cavitation as the breakdown of a liquid medium under very low pressures. In literature, the terms void/cavity formation and cavitation are often used interchangeably. The scientifically correct notation will be used consistently throughout this manuscript.

Relevant to the problem at hand, cavitation can occur due to a reduction of pressure below the vapour pressure at approximately constant temperature. The vapour pressure for water at 20^o was reported by Kaye and Laby [44] as 2.3 kPa. Cavitation in hydroelastic slamming problems typically occurs around the fluid-body contact interface during the decrease of the body velocity during impact where the fluid is displaced and accelerated. Consequently, the hydrodynamic pressure is reduced [85].

Combined effects of cavitation and ventilation were observed by Faltinsen [23] during the second half of the first wet natural oscillation period. However, Panciroli et al. [75], Ma et al. [57] and Reinhard et al. [85] state that this will only occur for light bodies entering the water with high impact velocities.

2.2.4 Physical Relevance

Higher structural deflection causes a lower peak pressure, with the peak being reached as a later stage of impact with respect to a stiffer construction. This effect is more pronounced for higher impact velocities and lower deadrise angles due to higher impact severity. During the impulsive interaction regime, the quasi-static method will overestimate the structural response resulting in over-engineering. On the other hand, the extent and relevance of the dynamic interaction regime is of interest particularly in cases of moderate structural stiffness [35, 75]. In addition, vibrations due to hydroelasticity can pose additional risks to structures due to resonances.

2.2.5 Challenges

Coupling

The inherent structural flexibility and the intensity of slamming impacts result in a coupled interaction between hydrodynamic pressure and structural response, where each influences the other. A fully coupled methodology to assess the interaction is required [92]. The problem is non-linear due to the wetted region which evolves with the impact [46]. Additionally, the shape of a cavity and the physical positions at which it is formed must also be captured in the coupling [46, 85].

For extreme impact conditions, cavitation can result in subsequent re-loading of the flexible body such that numerical models fail to handle these fluctuations. Furthermore, reproducing such events experimentally requires a highly robust setup to reproduce high velocity slamming events [57] and is beyond current capabilities.

Scaling

Ten et al. [92] state that modelling and capturing hydroelasticity at small scale is challenging with limited repeatability due to high sensitivity to fluid details [61], confirmed in the experimental synthesis in Section 2.4.2. Experimental constructions must be sufficiently flexible such that the phenomena described in Section 2.2.2 can be discriminated. In addition, water impact on an elastic panel will have double curvature subject to the set physical boundary conditions. Assimilating 3D fluid flow with 2D panel is therefore anticipated to be a challenge [45].

Interaction between air bubbles and cavitation

In Section 2.2, plate flexibility was demonstrated to further contribute to the presence of air in the water while presenting a unique set of challenges. A key limitation is anticipating the conditions under which the aeration phenomena will occur and reproducing it numerically. Challenges are anticipated with modelling cavitation phenomena due to relatively low pressures [73] and will possibly be enhanced by aeration [57]. Reinhard et al. [85] state that cavities may develop at fluid pressures higher than the vapour pressure because the air bubbles already present in the fluid are able to grow in

such low pressure zones. On the other hand, Panciroli et al. [75] state that the presence of entrapped air in the fluid should inhibit cavitation. Both claims have not been adequately substantiated by the respective authors and require further investigation.

2.3 Novelty

The slamming problem of interest in this study is of a hull slamming into aerated water, highlighted in Figure 4. The novelty of addressing the effects of hydroelasticity and slamming with aerated water on a structure's impacts poses a unique set of challenges that are addressed experimentally in this study.

The hydroelasticity effects on entrapped air as described in Figure 6 are directly linked to the generation of aeration in the water. However, the interaction between a flexible structure slamming into aerated water is unknown at present. An experimental approach is required to validate future numerical models. The effects of the vibrations from aeration and from the plate may cause resonances that must be captured and quantified. Additionally, the generation and interaction between density waves and the structure is unknown at present. An instrumentation system to capture the structural and hydrodynamic aspects of the slamming is required.

The experimental setup as described in Chapter 3 aims to combine pressure measurements across the bottom of the wedge with the water free surface, structural deflection and optical and physical strain measurements across the wedge. The different fluid-structure interaction regimes described in Figure 5 will be tested to provide a more complete understanding of the aeration across the entire fluid-structure interaction spectrum. Using two strain measurement techniques will also serve as a cross-check and allow an assessment of the two-dimensionality of the experiment. This work aims to transition from pressure development and propagation in aerated water to a quantification of structural effects, as highlighted by Khabakhpasheva et al. [45]. They noted that highly instantaneous pressure fluctuations can be filtered out by structural dynamics, also confirmed experimentally by Faltinsen [23]. To this extent, Ten et al. [92] state that risks for a structure to be compromised are mainly due to a combination of structure properties such as natural periods and damping together with the spatial and temporal pressure distribution. This statement is investigated and documented throughout this work.

2.4 Literature Synthesis

The Literature Synthesis provides a critical and in-depth overview of relevant scientific works in the analytical, numerical and experimental domains. A summary of the works and key scientific aspects addressed is provided in Table 1. Note that works marked with an asterisk include a semi-analytical approach, where an analytical theory was developed into a numerical model. The novelty proposed in this study is also highlighted. Sections 2.4.1, 2.4.2 and 2.4.3 are highly interdependent due to the complex nature of the slamming problem [95]. The separation is, however, important at this stage for critical analyses of different methodologies and how to combine aeration and hydroelasticity.

Table 1: Summary of the scientific aspects of relevant works.

Author	**Hydroelasticity**	**Aeration**	**Analytical**	**Numerical**	**Experimental**
Aghaei et al. [5]	x	x		x	
Ma et al. [57]		x		x	x
Mai et al. [58]		x			x
Mai et al. [59]	x	x		x	x
van der Eijk and Wellens [95]		x	x	x	x
van der Eijk and Wellens [98]		x	x	x	x
Chen et al. [13]	x			x	x
Faltinsen [23]	x		x		x
Hosseinzadeh et al. [35]	x				x
Hosseinzadeh et al. [36]	x			x	
Huera-Huarte et al. [39]	x				x
Khabakhpasheva and Korobkin [46]	x		x		
Korobkin and Khabakhpasheva [50]	x		x		x
Panciroli and Porfiri [70]	x		x		x
Panciroli et al. [75]	x		x		x
Reinhard et al. [85]	x		x		
Ren et al. [86]	x		x		x
Shams et al. [87]*	x		x	x	x
Sun et al. [90]*	x		x	x	
Ten et al. [92]*	x	x	x	x	
Wang et al. [106]	x				x
Wang et al. [107]*	x		x	x	
Wang and Guedes Soares [108]*	x		x	x	
Present study	x	x	x		x

2.4.1 Analytical

Von Karman [102] studied the water entry problem initially by applying the momentum theory to predict slamming loads acting on a two-dimensional wedge model. Assumptions of this theory include neglecting buoyancy and air effects and treating water as incompressible when a deadrise angle is present. Changes in water elevation, acceleration of water mass in the spray sheets, pressure variations over time and elastic structural responses are not accounted for. Wagner [104] developed the Von Karman [102] analytical model further by considering the effect of wetted surface deformation such as free surface jets on the hydrodynamic pressures. The free surface boundary conditions are linearized and imposed on the undisturbed conditions of the free surface. The model is limited to scenarios of small deadrise angles as the hydrodynamic loads are approximated by using a flat disk assumption. In addition, comparisons to experimental data resulted in over-predictions of hydrodynamic loads and stresses due to omitting higher order terms [91].

Faltinsen [23] developed an asymptotic hydroelastic theory for a nearly horizontal beam impacting the water at a wave crest. An Euler beam model was used to model the part of a ship plating between two adjacent transverse stiffeners. The fluid was modelled using a potential flow theory. An initial structure inertia phase and a subsequent free vibration phase were assumed. Negligible forward speed was assumed for cases of wet deck slamming based on experimental results by Kvalsvold et al. [51] where the deadrise angle was the dominant factor in slamming scenarios. The developed analytical theory did not match experimental results for pressure peak magnitude and time of occurrence. The analytical theory also predicted a pressure drop that can cause cavitation. This coincided precisely with the experimental values and was shown to occur at the same instant after impact. However, no sensitivity testing was conducted. The under-pressure was also over-predicted during the second half of the first oscillation period, with the pressure development being sinusoidal due to the free vibration assumptions. Additionally, ventilation and cavitation that cause a reduction in oscillation period are not reproduced in this theory. Due to a significant reduction in the oscillation period in experiments, Faltinsen [23] postulate that it is impossible to be purely due to damping effects.

Subsequent developments use a semi-analytical approach, where an analytical formulation for the fluid mechanics is combined with a numerical model for the structure and solved iteratively. These models require consideration due to the strong non-linear nature of the coupled interaction during the wetting stage. Semi-analytical models are inherently limited to the assumptions of the underlying theories used.

Korobkin et al. [49] directly coupled the Wagner [104] representation of the hydrodynamic loads during impact with a Finite Element Method (FEM) to represent an elastic wedge with low deadrise angle in 2D during the initial stages of interaction. The calculations of the velocity potential were reduced within the FEM to evaluation of the added mass matrix. For the FEM, the beam was divided into several elements. By considering only the wetted portion of the model, this approach is based on the simultaneous computation of structural deflections and hydrodynamic pressures. The velocity potential was evaluated across the wetted area to determine the structure's deflection and bending stress distribution. The Fourth-Order Runge-Kutta method was used for the time integration of the displacements of the beam elements and the coordinates of the contact points. In addition to limited use cases, this method was found to be computationally inefficient. The added mass due to the wetted nodes caused non-diagonal dominance of the added mass matrix making the system of equations more complex to solve, scaling this with the number of nodes being used in the FEM. Additionally, the authors anticipate challenges with the simultaneous computation of the structural and hydrodynamic effects particularly for violent impact conditions. This was compared to a modal approach, where the dry structural modes were first computed and the mass, stiffness and displacements of the interface were transferred to the hydrodynamic solver. The dynamic equations were integrated

in time and transferred back to the FEM code. In comparison to the directly coupled approach, the computational efficiency was directly dependent on the number of modes retained. However, for high-impact loads, over 100 modes were required to capture the interaction resulting in computational inefficiency. In addition to these shortcomings, the model is subject to the assumptions of the Wagner [104] theory.

On the other hand Korobkin and Khabakhpasheva [50] used a linear potential-flow theory and a simply-supported Euler Beam representation in 2D with a normal-mode method. Conditions for the plate impacting the wave with the centre aligned with a wave crest and with the wave crest impacting at an arbitrary location were considered. The practical implications of this approach are also explained in Section 2.4.2. Despite the authors explicitly pointing out the possibility of air cavity formation, the presence of air in the cavity was not taken into account. Time-dependent functions were used to track the position of the cavity, with the positions governed by ordinary differential equations. The high-pressure effects on cavity collapse are noted but not accounted for. Numerical calculations of peak bending stresses were compared against experimental measurements. The computational model tended to overestimate the contribution of higher-order vibrational modes. These effects were attributed to limitations with modelling the wetted surface development over time.

Ten et al. [92] used a semi-analytical model for the hydrodynamics and a three-dimensional finite element model for the structural component. The simplified approach for the fluid flow was justified in allowing more control over the fluid parameters thus isolating the relevant physical effects and flow characteristics while focusing on the structural response to the most critical impact conditions. No model tests for validation were used in this study. To this extent, the authors state that small-scale experiments are required for better control over impact geometry and aeration, however, high sensitivity to impact conditions can yield non-representative results. To develop the model, (a) a Wagner type impact, (b) a steep wave impact without aeration, (c) a Bagnold-type impact with an overturning wave just before encountering the wall thus entrapping air, and (d) a steep wave with entrained air were considered. For case (c), it was assumed that during the initial stage, the shape of the air bubble does not change significantly with time and the cavity thickness is small compared with the dimensions of the flow region.

For case (d), relevant to this study, compressibility was taken into account. The aerated fluid was treated as a fictitious volume with reduced speed of sound and density, beyond which the fluid was treated as homogenous and incompressible. The solution to the system of equations requires truncation and a fourth-order Runge–Kutta method due to the number of unknowns. This case was found to be the most severe, with the strains exceeding case (b) which represents an identical loading condition but without the aeration component. The formulations presented in this study were the only ones to analytically account for aerated water impacts on flexible structures.

Khabakhpasheva and Korobkin [46] argue that simplified models found in preceding literature are only suitable for some finite conditions of impact, with the underlying assumptions not always clearly documented. They combined the Euler-Bernoulli beam theory and the Wagner [104] model of water impact to investigate stresses in the elastic wedge entering water at a constant speed. Despite both hydrodynamic and structural models being linear, the interaction is inherently non-linear. The accuracy of the added-mass matrix calculation was investigated by varying the number of auxiliary functions in the expansions of the normal mode. They derived analytical formulae for elements of the added mass matrix of elastic modes of a uniform beam with different edge conditions and a differential equation for the size of the wetted part of the elastic wedge, which made calculations fast even when including a large number of modes. However, this model did not take into account the effects of air entrapment. Additionally, the developed model was adjusted to account for sprung boundary conditions with linear springs on the plate. The limitations of such a setup are documented extensively in Section 2.4.2.

Sun et al. [91] used a semi-analytical model for 2D hydrostatic slamming of symmetric flexible bodies. The flexible wedge was modelled as either two simply-supported or clamped-free Euler beams. The analytical Modified Logvinovich Model (MLM) was used to compute the hydrodynamic loads while accounting for the elastic deflections along the surface of the body. A modal approach was used to describe the elastic deflections. A partitioned coupling strategy was used, where the finite element model by Korobkin et al. [49] was used for the elastic wedge. Constant velocity and free-drop cases were used for validation with the vertical forces, structural deflection and strains. The developed semi-analytical model was found to be most suitable for the initial slamming stage, however, was unable to handle larger flow deformation and deep penetration into the water surface. Sun et al. [91] claim that such an approach was found to be more time efficient than BEM and SPH while providing results of comparable accuracy.

van der Eijk and Wellens [95] account for the shape of the body as in the MLM method to capture body contours other than wedges. A curved fictitious boundary condition (FBC) was used to account for object asymmetry and cavity formation during the initial impact stage. The added mass formulation is also modified to account for the submerged volume of the wedge based on the wetted length. Fourth-Order Runge-Kutta time integration was used to solve the system of equations. The method was also extended to account for air cavities at the closure stage of the buoyant wedge by changing the FBC. It was found that the FBC depends on the velocity and different coefficients must be adopted throughout the beginning of separation and closing stages of impact being required. The formulation presented in this paper requires insights from numerical models is therefore limited as a stand-alone tool. To summarise, the relevance of analytical models is recognised at the experimental design stage and as a starting point for the numerical implementation of hydroelastic slamming into aerated water.

Analytical - Summary

Analytical studies were found to establish the foundational understanding of hydroelastic slamming by coupling beam theory with idealized hydrodynamics. The strength lies in offering clear, parametric insight into key interaction variables such as structural stiffness, impact velocity and wedge geometry, and for high level design considerations. However, these models are based on physical assumptions that limit their validity to specific parameter ranges and prevent the capture more complex phenomena like free-surface dynamics or aeration effects. As of the time of writing, no analytical model to account for the effects of aeration on the impact was found.

2.4.2 Experimental

Various approaches are reviewed in the build-up of an experimental set-up to capture the combined effects of aeration and hydroelasticity. Experiments mainly consist of waves incident on a structure [12, 48, 55, 59, 67] or of a structure being dropped with a certain velocity onto a body of water [13, 35, 75, 95, 98]. The latter case is of interest for this study. Hosseinzadeh et al. [35] provide a complete summary of the key experimental set-ups highlighting critical dimensions, mass, materials and test conditions. Despite the focus of this work being on structures slamming into the water, this review focuses on certain principles of implementation to provide further insight into the problem at hand.

Sprung Structures and Boundary Conditions

Springs are implemented extensively to incorporate structural elasticity, tune the stiffness of boundary conditions and take measurements of structural deflection [32, 59]. Mai et al. [59] used two variations of experimental set-up: (i) a free-falling 12 mm flat plate representing a hull bottom and (ii) wave impacts on a 12 mm vertical wall representing a hull plate section. Both set-ups were tested with springs and with a rigid boundary condition. In the flat plate slamming set-up, pressure sensors were used to measure the pressure distribution on the plate, displacement sensors were used for the springs, a load cell was used to measure the local force and accelerometers were used to measure the structural vibrations. Velocities between 1-7 m/s were tested. The vertical wall set-up was loaded via breaking, high aeration, flip-through and slightly breaking wave profiles, thus also testing variations in wave energy distribution. The position of the wall set-up was changed to interact with the wave at different phases of the breaking wave propagation [59]. Wave gauges were used to measure the wave profile. Such a set-up is anticipated to impose challenges with repeatability and with controlling and evaluating the effect of the aeration properties due to the dynamic characteristics of the water surface, particularly for the flip-through condition.

For the flat plate, the elasticity in the sprung case was found to reduce impact pressure and force for impact velocities over 5 m/s. Below this impact velocity, a consistent trend could not be established. The authors postulate that the spring stiffness is significant in comparison to the stiff mounting, and this is plausible. The elasticity was however found to cause post-impact pressure oscillations. Impulse loading during the first phase while the force does not change direction was found to decrease with the softest spring configuration tested. For the sprung wall under the high aeration, flip-through and slightly breaking wave impacts, the total impact force was observed to decrease in comparison with the rigid wall. However, the impact pressure was only found to decrease for the condition where the air pocket was completely entrapped by the breaking wave on impact, as per Figure 2a.

This set-up only captures compliant spring displacement rather than hydroelasticity as defined in Section 2.2, with no discrimination made between the two. Additionally, load cell measurements for the force over the entire set-up does not directly account for the structural effects of hydroelasticity on the structure, thus failing to capture the structural dynamics [23]. Comparison to other set-ups such as Ma et al. [57] and Panciroli et al. [75] implies that the plate was not sufficiently flexible for the effects of hydroelasticity to be well defined. In conclusion, this approach is very limited to representing and capturing hydroelasticity phenomena of flexible bodies. Kimmoun et al. [48] used the same test conditions but for a flexible wall while capturing the pressure distribution on a flexible wall, deflection of the wall and details of the flow. Liao et al. [55] conducted a dam break experiment at a small-scale on a structure that was clamped at the bottom with the top being free to deflect and oscillate. The impulsive impacting force was found to cause maximum deformation with the first mode of vibration being dominant. The violent turbulent flow in the air cavity during breakdown was found to induce oscillations in the impact load and vibrations to higher modes. The higher modes of vibration were found to be sensitive to the violent turbulent flow motion in the air cavity. The latter mentioned two approaches directly take into account the effect of an impact of a body of

water with a free surface on a structure.

Khabakhpasheva and Korobkin [46] discuss a *blockage* effect for elastic impacts of a plate connected to a main structure with springs due to a sudden change of the region in contact with the water. Consequently, a sharp peak of the hydrodynamic loads occurs close to the end of the impact stage. Furthermore, [50] state that under certain plate flexibility and loading conditions, the plating ends can be forced into the liquid prior to complete wetting due to the combined effects of the springs and the variation in body shape. The elastic deflection can consequently cause a high added mass increase due to contact with the free surface leading to high hydrodynamic loads in the contact region [46, 50]. The latter phenomenon could artificially enhance the formation and collapse of cavities altering hydrodynamic load peaks.

Kvalsvold et al. [51] also used drop tests with a steel plate of 8 mm thickness and an aluminium plate of 5 mm thickness with springs at the boundaries of the plate. Measurements for the pressure and strain throughout the length of the plate and global and local vertical accelerations were taken. Waves of different steepness were generated and the spring-loaded plate was then dropped onto the wave crest. This approach is anticipated to introduce challenges with perfectly aligning the centre of the wave crest and the centre of the plate repeatedly. Challenges are anticipated with extending such an approach to also introduce and control the aeration component due to the inherent motion of the wave crest. Due to the plates tested in these experiments being significantly thinner than those tested by Mai et al. [58] and Hendriksen [32], the plate deformation was found to significantly affect the interaction.

A significant reduction in the deflection and oscillation period were found in the second half of the first oscillation period, which Kvalsvold et al. [51] attributed to the ventilation and cavitation. High pressures were measured during the initial stages of impact. The maximum bending stress was found to be proportional to the drop velocity and not sensitive to the location of wave impact of wave crest curvature. Furthermore, negative pressures relative to atmospheric and wetted length reduction were found in the second half of the first natural oscillation, thus indicating the possibility of cavitation and ventilation while also possibly affecting the deceleration of the plate into the water, as observed by Panciroli et al. [75]. The experiments by Kvalsvold et al. [51] indicate that the peaks in pressure do not correspond to the development of stress under certain interaction regimes. Faltinsen et al. [26] further confirm that maximum pressures are highly sensitive to the impact conditions and that slamming-induced stresses are strongly influenced by the dynamic hydroelastic effects. To this extent, Khabakhpasheva et al. [45] recommend that strain measurements are taken for a complete overview of the effects of hydroelasticity.

Similar to Mai et al. [59], Hendriksen [32] designed a deformable folding wedge about the keel with springs at the chine. The experiment attempted to quantify the effect of dynamic deformation of a structure on the maximum pressure at the wedge surface by measuring rotational deformation, pressure and acceleration under different impact speeds and deadrise angles. A higher deadrise angle was found to decrease the maximum pressure acting on the body. Higher dynamic deformation of the structure during impact was found to decrease the maximum pressure in comparison to a rigid structure. Pressure oscillations after the initial impact were also captured. However, it was not possible to generate a conclusion regarding the structural response as no structural measurements were taken. The experimental set-up used only accounted for the rotation of the plates about the central hinge, rather than hydroelastic deformation of the plate due to the impact, thus limiting the application of the results for validation of hydroelastic numerical models. A direct relationship between hydroelasticity and the impact loads cannot be made with such a set-up.

Hendriksen [32] observed that the peak pressure did not directly correspond to the peak rotational motion. It is possible that the pressure peak was filtered by the dynamics of the structure while

also being affected by the sprung boundary conditions [23]. Additionally, no strain gauges were placed to capture deformation along the plate. It is therefore not possible to make a conclusion about this effect. Visual inspection of high-speed camera videos indicated that the plate experienced some deformation, but this was not quantified. Hendriksen [32] proposes the use of high plate rigidity such that only the effects of the spring are being taken into account, however, this will further limit the extent to which hydroelastic effects are reproduced and captured. They also comment about the damping effects of the potentiometers on the motion of the wedge plates at low impact velocity, although these effects are not evaluated. A pressure overshoot was also observed at a later stage to the initial pressure peak. Through this literature search, the present author attributes this effect to the blockage phenomenon described by Khabakhpasheva and Korobkin [46].

Synthesis of experiments of hydroelasticity with sprung boundary conditions indicate incomplete conclusions on pressure development and spring deflection together with incomplete hydroelasticity phenomena. The use of sprung boundary conditions to represent vessel plating does not correctly represent practical boundary conditions. For a structure that is inherently flexible, the compliance in springs, and possible damping from transducers will add another source of uncertainty to measurements of deflection while interfering with hydroelastic phenomena and altering the natural modes of the coupled system. Consequently, such a set-up will be avoided, in favour of a set-up with minimal interference of the metrology, measurements for the stain effects on the structure and representative boundary conditions.

Fixed Edge Boundary Conditions for Hydroelasticity

Ren et al. [86] used 12.7 mm and 3.2 mm 6061-T6 aluminium sheets to serve as rigid and flexible respectively, and a 3.3 mm E-Glass reinforced Epoxy composite wedge with a 20^o deadrise angle at different drop heights to reproduce hydroelastic slamming phenomena. The wedge set-up used consisted of a structural body made out of a rigid welded frame onto which the different wedge models were mounted. Each model weighed 40.65 kg. Pressure sensors were mounted into the wedge bottom to measure the hydrodynamic pressure. A high-speed camera was used to capture spray root propagation and 3D-digital image correlation (S-DIC) was used to measure the wedge displacement field and thus measure the structural response. The instruments were calibrated and the systematic uncertainty of the set-up was evaluated as per Coleman and Steele [14]. A DAQ was used for synchronization to 100 ns was achieved. Such a synchronization rate is four orders of magnitudes of the expected timescale of slamming phenomena, which is on the order of 1 ms thus being suitable for the conditions being tested [86]. The instrumentation system used for this study allows for a direct correlation of the hydrodynamic and structural phenomena.

Ren et al. [86] noted a reduction in peak pressure with a lower flexure rigidity. This effect was found to be more pronounced for higher drop heights. The authors attribute this to more absorption of impact energy under flexibility. Maximum deflection and strain were found to occur while the chine was still not wetted. Furthermore, flexure was found to delay the occurrence of the peak pressure on each pressure sensor. The authors attribute this to the prolonged propagation of a pressure wave across a deformed structure. Consequently, the flexibility also increased the wetting time to reach the chine. The authors therefore note a direct effect on the flexibility and the spray root velocity. The peak hydrodynamic pressure was found to be proportional to the square of spray root velocity. Chen et al. [13] used a similar approach with a three-dimensional wedge steel structure with stiffeners with a deadrise angle of 45^o. The wedge was constructed out of 5 mm steel plates. Transverse frames and longitudinal stiffeners were added. Baffle plates were added to the longitudinal ends to prevent longitudinal flow effects. This approach attempts to constrain fluid flow within the bounds of the body of the wedge thus somewhat restricting 3D end effects. However, visual measurements are limited and the baffles introduce a structural stiffness distribution throughout the length of the wedge.

Hosseinzadeh et al. [35] used an asymmetric wedge construction similar to Chen et al. [13] made out of 4 mm aluminium panels to compare a stiffened and unstiffened base plate. Pressure sensors and strain gauges were placed at various longitudinal intervals to assess the pressures and strains in three dimensions. For the stiffened panel case, hydroelasticity was only significant at high impact velocities. For the unstiffened panel, the effects hydroelasticity were always found to be more pronounced. Higher peak pressure was found for the stiffened plate, with the pressure peak for the unstiffened plate being reached at a later stage. These effects were enhanced for high impact velocities and low deadrise angles. Higher strain values were recorded for the unstiffened plate as expected. Elastic vibrations were more prominent for heavier wedges and for the unstiffened plates at higher impact velocities. The maximum strain and deformation were also observed during the wetting phase for both plates. The influence of the clamped boundary conditions longitudinally was also found to be significant, with the strain at the centre of the plate, thus at the furthest point from the clamped ends being the highest. This effect is anticipated to be more pronounced for experiments at smaller scales. Additionally, asymmetric structural stiffness and weight distribution will result in a moment on impact was was not quantified.

Free Edge Boundary Conditions for Hydroelasticity

Panciroli [69]-[73] have conducted multiple experimental investigations on deformable wedges to assess the slamming phenomena experienced during water entry. The set-up used consisted of a drop weight machine with a central mechanism to adjust the deadrise angle. The far ends of the wedges were free. The provided justification for this boundary condition was that hydroelasticity is more prone to appear for structures with a longer natural period, as would be for a free end as opposed to a pinned or clamped end. Consequently, hydroelastic effects could be observed at lower impact velocities and were more visible thus easier to measure using this set-up [72]. While valid from a practical point of view, these boundary conditions do not accurately represent slamming of maritime structures into the water.

This set-up is limited to wedge entry hydrodynamics with the focus being on hydroelasticity. The lack of enclosed wedge means that buoyant wedge entry as described by van der Eijk and Wellens [95] cannot be reproduced. Additionally, once the chine is wetted, water spillover would occur, limiting the possibility of using optical non-contact measurement techniques. Panciroli et al. [73] used Particle Image Velocimetry (PIV) to evaluate the pressure field and capture the vibrations of the wedges. The total hydrodynamic force was found to attain negative values during certain stages of the impact, resulting in the wedge being sucked in by the fluid. A change in the direction of the pressure were also observed by Mai et al. [58]. Furthermore, Panciroli et al. [73] found that the values and location of the magnitude and minimum pressure acting on the flexible wedges were dependent on the flexibility of the structure, and that structural vibrations affected the hydrodynamic load magnitudes and direction. Due to limitations with computational memory, imaging was only conducted on half of the wedge. The authors therefore assume perfect symmetry throughout. For a case of aeration, the entire wedge should be filmed, allowing a more complete overview of the shock waves while also accounting for bubble stochastics [15].

Experiments with Aerated Water

As highlighted in Section 2.1.4, aeration levels on model scale are not representative to full scale and applying conventional scaling laws to small-scale experiments yield limited conclusions. However, artificially aerating water at small-scale allows the effects of aeration to be preliminarily investigated while having the percentage of aeration in the water as a controlled variable.

Ma et al. [57] considered a 12 mm rigid flat plate impacting pure and aerated water. The set-up consisted of the impact plate connected to two driver plates, with impact velocities between 4 and 7 m/s

being achievable. Aeration was controlled by adjusting the injection pressure of an air compressor into a bubble generator. Air flow rate measurements were used to determine the air void fraction. A limitation of this approach is that aeration was only measured at 250 mm below the water surface and assumed homogeneous. The variation of air bubbles near the free surface were not taken into account. Furthermore this approach does not use any optical measurements to detect bubble concentrations and collapses. The authors characterise the stages of impact landing on rigid plates as (1) shock loading and peak pressure, (2) fluid expansion loading with very low sub-atmospheric pressure, and (3) secondary reloading with super-atmospheric pressure. Ma et al. [57] also claim that the three stages observed in hydrodynamic impacts of aerated water are very similar to underwater explosion observed, where primary shock loading, low-pressure cavitation loading, and the subsequent violent re-loading due to the collapse of cavitation. This claim requires further investigation, particularly for the existence of an analytical model that can be adapted slightly for use of verification in this study. Furthermore, the authors recommend careful analysis of strong acoustic noise on impact. Aeration of 1.6% was found to reduce the local pressure peak by half. Aeration was also found to increase the rise and fall of the peak pressure load. Consequently, the impulse was found to be comparable to the pure water case. The variation in impulse was found to be most sensitive to the change in peak loading rather than the change in aeration.

The state-of-the-art experiments with aerated water are the fall tower drop tests by van der Eijk and Wellens [95, 98]. The wedge with 15^o deadrise angle was constructed out of 12 mm plywood. Air bubbles were created using 12 air diffusers. Both experimental results and numerical simulations demonstrated that increasing aeration reduces the magnitude of the initial pressure peak, while dispersing the load over a longer duration due to fluid compressibility. The extent of pressure reduction was strongly dependent on the air volume fraction, with even small levels of aeration producing measurable declines in peak pressure. Additionally, aeration led to secondary oscillatory loads associated with density waves, which became more prominent as aeration increased, with the amplitude of these waves increasing and their frequency decreasing.

The presence of air bubbles was found to influence the free surface dynamics both before and during impact. Rising bubbles induce upward fluid motion that can pre-condition the flow field during the impact. Hong et al. [34] reported that for a rigid structure impacting aerated water, the jets tend to rise vertically in pure water but deflect outward in aerated conditions. Similarly, Wu et al. [113] observed that bubble-induced surface currents, driven by the lateral motion of bubbles from the tank centre toward the sidewalls, impart horizontal momentum to the jets in aerated water, causing a lateral spread of the impact-generated flow. Additionally, bubble interactions are expected to disrupt the smoothness of the water jets, producing a fragmented and non-uniform free surface.

Experimental - Summary

Relevant experimental approaches and instrumentation techniques for a set-up combining hydroelasticity and aerated loading have been critically evaluated. For a representative assessment of hydroelasticity, the plates constituting the wedge section must be able to deflect without influence of flexible boundary conditions. Instrumentation techniques which directly penetrate the wedge will have an inherent effect on the structural properties and the interaction. The influence is expected to be more significant for smaller structures with higher numbers of pressure sensors. Consequently, optical techniques must be considered.

2.4.3 Numerical

Khabakhpasheva and Korobkin [46] state that numerical models must be used when the deformations of the flow region cannot be treated as small, beyond the remit of the analytical theories being extended into a semi-analytical model. Different numerical approaches to coupling have been developed for elastic body impacts on a fluid surface allowing applications across a wider range of impact conditions. Complete numerical modelling of the fluid-structure interactions during slamming impacts is also highly complex. Consequently, simplifications are often made, with aspects such as fluid compressibility and aeration being assumed negligible unless specifically within the scope of the work [38, 92]. Decisions have to be taken regarding which physics is the most relevant to the problem at hand and how this will affect the structural effects on the structure [92]. This critical review serves to provide a comprehensive overview of different numerical methods while addressing the suitability of implementing physical aeration phenomena, as per the challenges highlighted in Sections 2.1.4 and 2.2.5. Furthermore, this section of the literature review demonstrates the relevance of the experiment described in this work as a basis for providing a validation case.

Coupling Strategies

In the monolithic approach, the entire domain is solved as a single system of equations with all entities advancing simultaneously in time. In a partitioned approach, the solid and fluid domains are decoupled and the interfaces are communicated and synchronised during each time step [5, 31]. For partitioned solutions, weak and strong coupling are possible. For strong coupling, an iterative loop is required per time step. Figure 7 shows different coupling strategies for solving such FSI problems. In this Figure, **F** is a differential operator, ξ and ς are the variable systems for the structural and the fluid domain respectively.

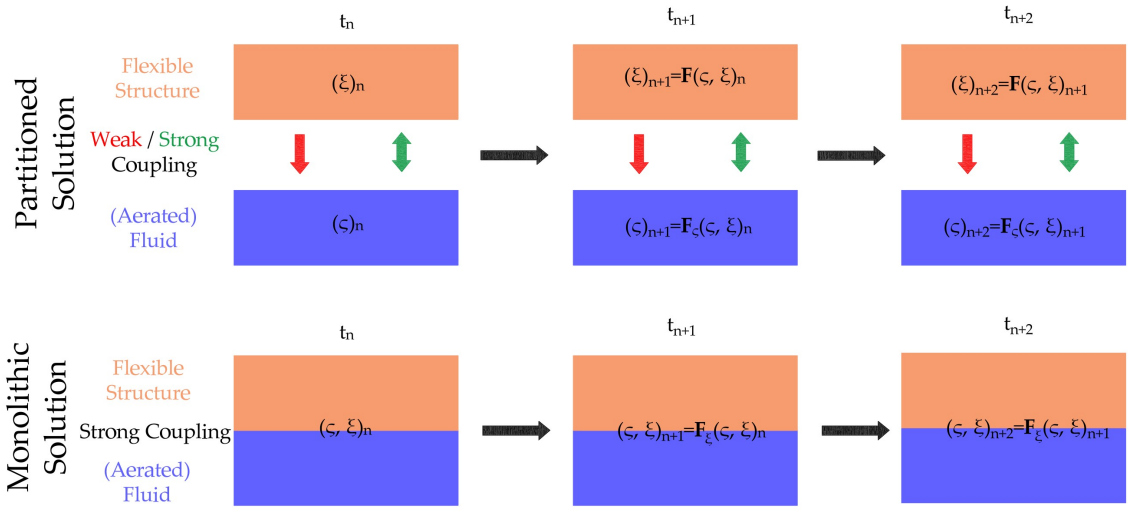

Figure 7: Coupling strategies for FSI problems. Adapted from [5, 13, 31].

Coupling of Hydroelasticity in Pure Water Impact

Panciroli et al. [71] used a coupled Finite Element Model (FEM) and Smoothened Particle Hydrodynamics (SPH) implementation in LS-Dyna. Compressibility, air cushioning and air entrapment were neglected, and symmetrical impact was assumed. Homogeneous SPH spacing of 2.5 mm was used and shell elements with 4 integration points were used for the flexible wedges. Validation was done by comparison to experimental measurements of deflection by PIV and of strain from strain gauges on the surface of the plates and wedges [73]. Furthermore, three experimental runs were conducted, but the experimental uncertainty was not quantified. This implementation was found to highlight key challenges in representing physical phenomena associated with hydroelastic interac-

tion of very flexible structures. The numerical method predicted the occurrence of an initial peak in strain, however, the magnitude and time of the peak were not correctly predicted under all the impact conditions tested. Furthermore, the subsequent strain oscillations were not captured correctly. For higher impact speeds and lower deadrise angles, fluid detachment was observed numerically and higher plate vibrations were obtained in comparison to experimental results. The model limitations were evident in capturing the dynamic features of the elastic vibration, especially at the later stage of slamming. Additionally, the deformation predicted by the SPH implementation was found to be flatter than experimental and analytical results. A small amount of entrapped air was found to significantly modify the shape of the water surface numerically, highlighting the importance of accounting for ventilation and cavitation. Consequently, this numerical method was shown to be limited in capturing the physics.

Chen et al. [13] used a partitioned CFD-FEM two-way coupled method to simulate the slamming and water entry problem of a wedge with stiffeners. CFD solver STAR-CCM+ and FEM solver Abaqus were coupled within the SIMULIA co-simulation engine. Convergence at each time step was assessed using the root mean square (RMS) residual value or a maximum of internal time steps. Implicit coupling and iterative stagger were applied to ensure strong coupling and convergence. The CFD and FEM solvers operated in parallel with multiple iterations per time step. For the FEA, deformable three-dimensional shell elements were used for the hull plate and stiffened panels. Chen et al. [13] state that when maintaining a constant FEM scheme, and varying the CFD scheme, the uncertainties associated with the latter solver were the dominant source of numerical uncertainty. The high-frequency whipping responses in the stress and acceleration were well reproduced by the developed coupled method and distributed across the same frequency bands in the conditions tested.

Hosseinzadeh et al. [36] tested (1) an explicit non-linear LS-DYNA FEA method incorporating a Multi-Material Arbitrary Lagrangian-Eulerian (MMALE) solver and (2) a strongly two-way coupled technique using RANS CFD and FEA solvers by STAR-CCM+ and ABAQUS commercial solvers. In the former approach, air and water were idealised in the same element and coupling occurs between the fluid and the solid at the interface. Nodal velocities on the fluid and structure are to be equal and coupling occurs between the fluid and the solid at the interface. A master-slave penalty contact method was used for conservation of momentum and energy. The penalty coupling allows for parallel fluid flow to the structure without penetration. In the latter approach, during each time step, the pressure load and shear stress from the CFD model are first computed and then applied as a surface load in the FE model and the calculated nodal displacement of the structure is transferred back to the fluid domain. Therefore, the fluid domain mesh can be updated for the next time step using a mesh morphing technique based on the deflection and vertical translation of the structure.

The two methodologies were validated by direct comparison to the experimental results in [35]. Discrepancies between the experimental and numerical approaches were found for the maximum values of pressure and strain responses, particularly at the points corresponding to sensors in proximity to the chine due to the added complexity of the free surface. The comparison for the maximum value of pressure should not be treated as absolute due to the possible structural filtering effects as explained by Ten et al. [92] and Faltinsen [23]. However, the comparison for maximum strain requires some consideration. It was not possible to establish a consistent trend in the behaviour of the numerical models, while also highlighting the relevance of the 3D effects along the longitudinal axis of the wedge. The MMALE was found to have larger numerical fluctuations, due to high dependency on free surface contact forces, penalty coupling algorithm and damping factors. Additionally, comparing 2D and 3D simulations indicated lower values of the maximum slamming force coefficients for the 3D case.

Aeration

A significant body of work is available on the development of fully compressible finite volume methods (FVMs) for interaction between compressible aerated water and rigid moving bodies [95]-[98]. The numerical method was built from scratch, verified, validated and improved to ensure the correct physics is captured, free surface artifacts were minimized and the physics of the fluid under impact was well captured and the method is computationally efficient. The latest developments include a cut cell method to account for parts of the domain where the body's contour intersects the cells with the air and fluid domain. Furthermore, an additional fraction field was defined to account for homogeneously distributed air in water in combination with a new formulation for the multiphase speed of sound prevent over-prediction of compressibility by artificial air entrainment [98]. Finally, the numerical model was adapted using a novel bilinear interface reconstruction algorithm (BLIC) to capture highly-curved interfaces more accurately on structured grids without a significant increase in computational costs. Furthermore, an unsplit donating quadrant advection (DQA) scheme was used to prevent spurious interface velocities, negative densities, and instabilities by allowing fluid to enter and exit a cell in a time step [97]. The reader is referred to van der Eijk [94] for further details about these models. The model was validated using the setup described in [95]. The numerical simulations accurately represented experimental forces, with acceleration differences up to the closure stage remaining within 8%. Additionally, simulations provided clear identification of structural frequencies and reliable visualizations of free surface elevation.

Aeration and Hydroelasticity

Aghaei et al. [5] implemented a 2D partitioned approach in OpenFOAM to simulate the strongly-coupled interaction of elastic bodies with a compressible homogeneously aerated fluid under slamming of a plate. This study was unique in that no previous study specifically considering impacts of a flexible structure on an aerated body of water was conducted. The Wallis equation was used to capture the speed of sound, and the aerated fluid was considered as one aggregate field with one momentum equation for the entire domain. An Arbitrary Lagrangian Eulerian (ALE) kinematical description of the domains was used. Laplace smoothing equations were used for the mesh to follow the movement of the fluid-solid interface. The authors state that at the time of publication, no experiments combining flexible structures impacting on an aerated body of water were available. Validation was therefore attempted by separately evaluating the physics behind hydroelasticity and aerated impact phenomena.

The flexible plate water entry experiment by Faltinsen et al. [26] was used to validate the physics of hydroelasticity during water entry using the strain and pressure evolution during impact time. The developed model did not capture the pressure peak and the fluctuations in pressure over time at the plate centre, albeit the same trend is followed. Furthermore, the phase and magnitude of strain oscillations beyond 10 ms after initial impact were not well captured. Aerated and pure water entry of a rigid flat plate was assessed using the experiment for the free-fall of a rigid plate on an aerated fluid by Ma et al. [57]. The phases and magnitudes of pressure during impact, defined by Ma et al. [57] as a high pressure shock load, fluid expansion induced sub-atmospheric loading, and the weaker second pressure peak were well captured. For an aeration level of 0.8%, the peak pressure rise time was not captured and the peak was out of phase for the side pressure probes. An occurrence of sub-atmospheric pressure was also captured. Aghaei et al. [5] attribute this to the presence of air cushioning and possible asynchronous physical pressure measurements. Furthermore, uncertainty due to the angle of impact is not accounted for numerically.

This approach to validation is limited as the physics behind the interaction of aeration and structural flexibility is not captured holistically, and thus the numerical method cannot be considered as properly validated. Despite this limitation, a systematic parameter study was conducted. A low value

of aeration was found to reduce slamming forces but over a longer impact duration. A reduction in the effect of plate flexibility on slamming loads in aerated water was found. The effects were found to diminish for aeration levels over 5%. For the conditions tested in this study, the authors therefore conclude that in breaking wave load impact, strong coupling may be redundant. This claim is based on a study carried out using a non-validated numerical model, at experimental scale, and thus cannot be generalized for all conditions. Further work is required to validated the numerical model with purposefully designed experiments.

Numerical - Summary

Key numerical techniques to solve fluid-structure interaction and aeration impact problems have been summarised and evaluated. Significant challenges remain in accurately reproducing physical conditions near the free edge of flexible structures, particularly due to complex free-surface behaviour and localised compressibility effects. No existing study presents a dedicated solver that couples flexible structures with a compressible, aerated fluid domain in a fully validated framework. In addition, no complete experiment to serve as a validation case has been conducted in the past. Consequently, this poses a challenge when designing an experiment to investigate the physics as the combined effects cannot be accounted for holistically.

2.5 Summary of Literature and Research Question

The literature review reveals that impact conditions and the level of fluid aeration in the impact zone for a vessel slamming into water can potentially cause significant variations in local impact dynamics. While hydroelastic impacts have been extensively studied, and some works have examined rigid-body slamming into aerated water, the combined case of flexible structures slamming into a weakly compressible medium has never been investigated. Addressing this gap is essential for representing more realistic environmental loading conditions in slamming. The development and generation of an experimental dataset from a state-of-the-art setup will serve as the first step towards developing validated numerical models. Based on these objectives, the following research question is formulated:

How does the aeration component in water influence the structural loading and response during hydroelastic slamming events?

This research question is broken down into two sub-parts:

Sub-Question 1: How do structural stiffness, impact velocity, and aeration jointly govern structure loading and strain response?

Sub-Question 2: To what extent can the individual effects of hydroelasticity and aeration be distinguished, and across which conditions does each dominate?

3 Experimental Methodology

3.1 Overview

The experimental campaign to answer the Research Question is executed using the fall tower setup, located at the Ship Hydromechanics lab at Delft University of Technology. The setup consists of the stiffened fall tower connected to a fluid domain box and a wedge, as shown in Figure 8. The wedge is mounted onto a carriage which is hoisted up with a pulley to the specific release height and held in place by an electromagnet. The carriage fits into the guide rails and is released when the system is triggered. The reader is referred to [94] for complete details of the fall tower.

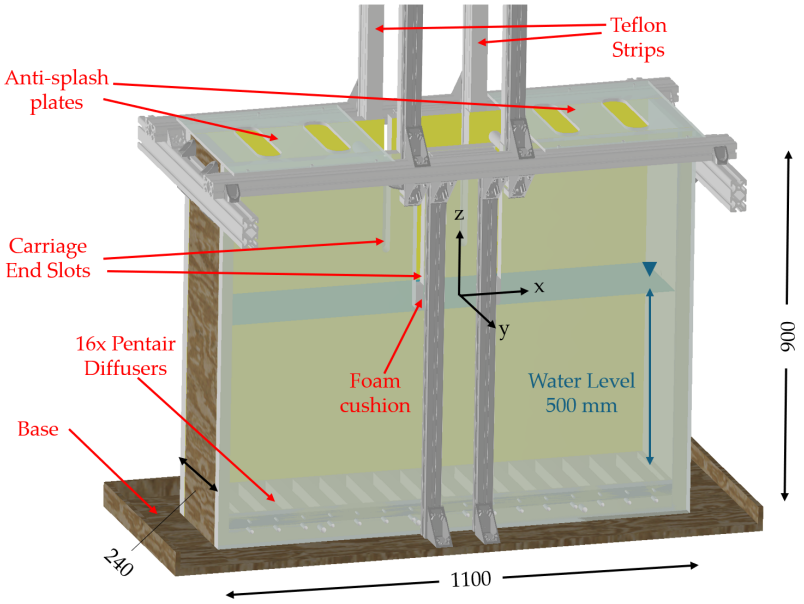

(a) Domain box containing water.

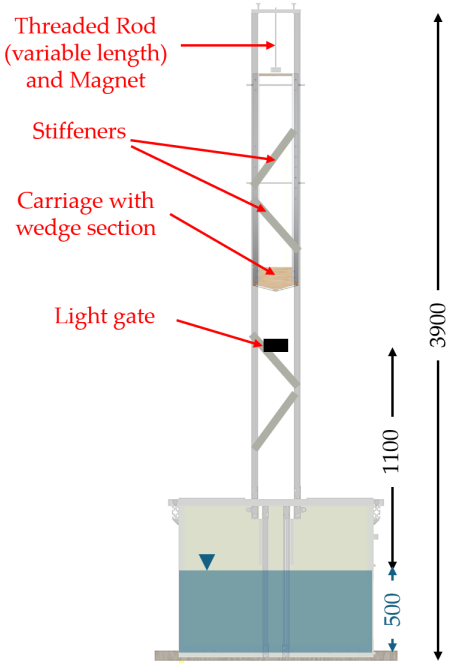

(b) Stiffened fall tower.

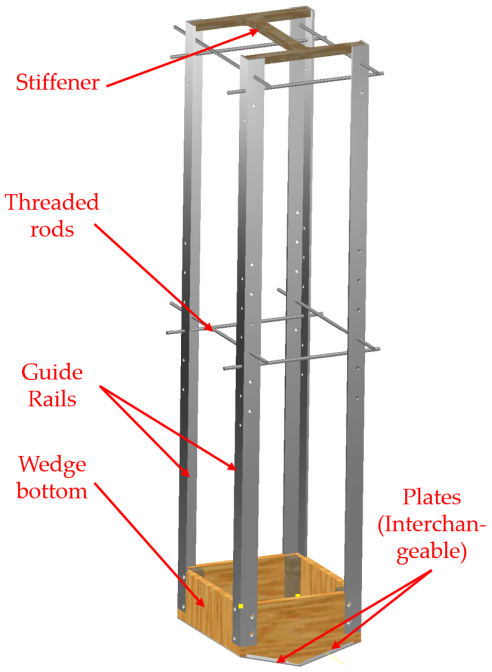

(c) Carriage with wedge attachment.

Figure 8: Overview of experimental setup.

The starting point for the design of the experiment was the setups described in Hendriksen [32] and van der Eijk and Wellens [95]. The novelty in this experiment is related to the hydroelastic properties of the wedge bottom plates and the ability to test out interaction in different hydroelastic regimes. To represent accurate conditions of ship structural member, a clamped-clamped condition along the x axis, with stiffeners at the keel and chine are required. For a setup to be fully 2D, the influence of the y-dimension on the deflection and stress propagation must be negligible, such that the pressure and stress distributions are approximately equal throughout the length, and the plate can be approximated as a 2D beam. To achieve this, the boundary conditions at the fore and aft of the wedge must have negligible influence on the bending of the plate. The two edges at the fore and aft were kept as free to this extent. Physical 3D effects of interaction are inevitable, as demonstrated by Hosseinzadeh et al. [35] and Wu et al. [113]. Aeration, free surface flows and fluid phenomena at the ends of the domain box are also expected to enhance the 3D effects. The strain gauges and DIC will quantify the effects across the plate during the impact. Furthermore, having the bottom plates clamped on all 4 ends would result in excessive stiffness and high vibration modes as per Young and Budynas [115] while also hindering the 2D effects on the plate due to multiple deformation modes along the x and y axis, particularly at small scale. In addition, higher frequencies of vibration result in higher required sampling and frame rates for data acquisition, required as per the Nyquist theorem [86].

3.2 Design of Experiment

The new wedge design with deadrise angle $\alpha = 15^o$ and with flexible bottom plates is shown in detail in Figures 9 to 11. The flexible bottom plates were only clamped at the keel and chine via a bolted connection, and the fore and aft ends of the plates were kept free.

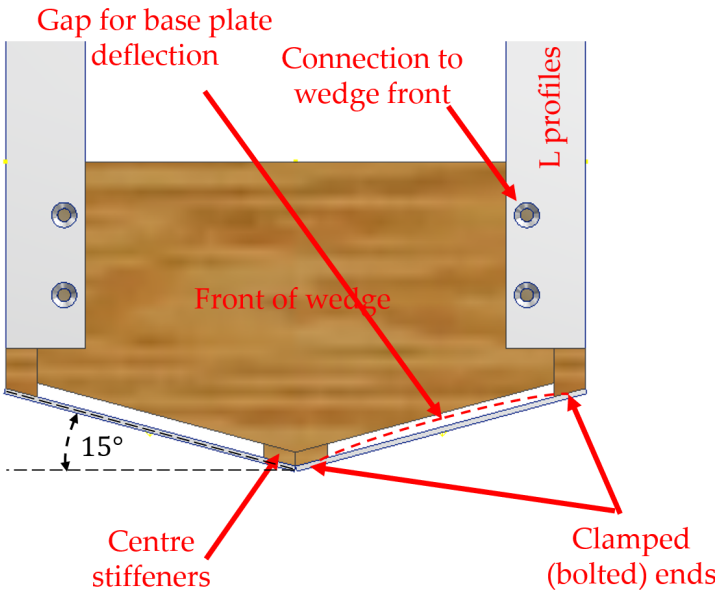

Figure 9: Wedge front view.

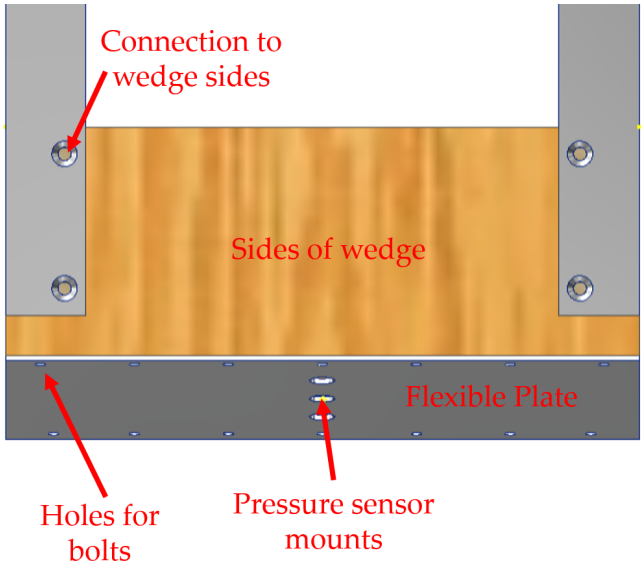

Figure 10: Wedge side view.

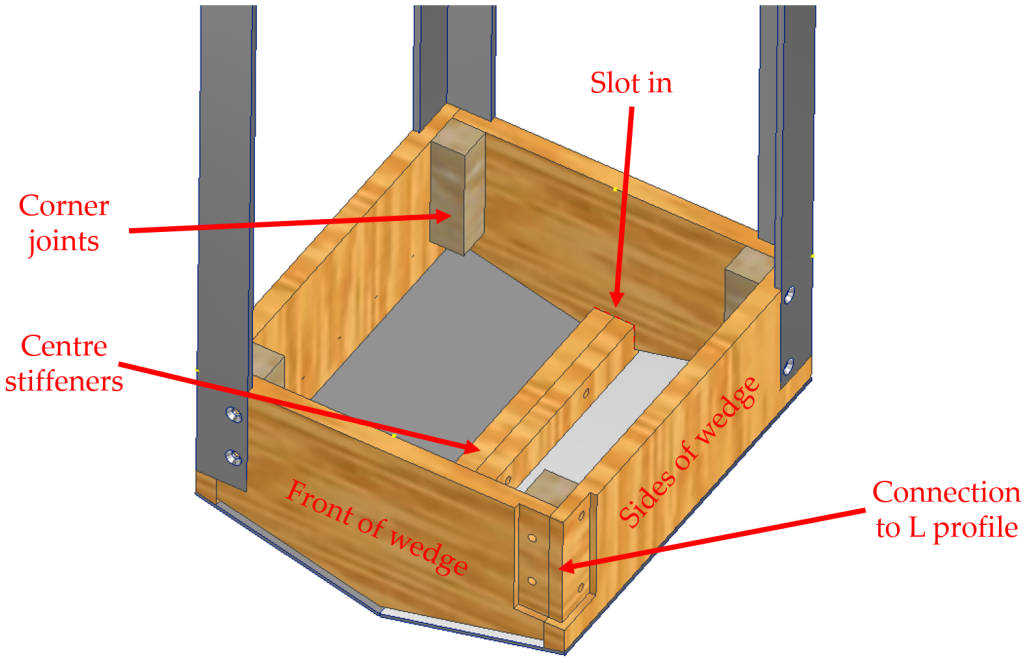

Figure 11: Three dimensional view of the wedge.

The gap was specifically sized to 5 mm such that no contact with the plates occurs on bending. The analytical model described in the following section was used to compute the deflection, however, based on Figure 5 and experimental results by Hosseinzadeh et al. [35], sufficient allowance for the clearance was made. The open gap will allow for water ingress. The gap was however designed such that water ingress is limited during the initial contact due to the placement of the fore and aft panels. Experience with previous experiments shows this will only be relevant once substantial deceleration and immersion have occurred, thus being beyond the remit of this investigation. All the sensors on the plate were waterproofed due to the complete wedge immersion and the open top, as described in Section 3.6. The reader is referred to Appendix 1 for complete schematics of the wedge.

3.2.1 Analytical Approach

The hydroelastic effects were starting point for the design of experiment. An analytical procedure was used to determine the base plate thickness to ensure that a range of hydroelastic regimes can be tested without structural failure. The analytical approach used is based on wedge simplification to a clamped-clamped beam under uniform load [35, 69, 86, 89]. The location of peak stress is defined at the clamped end, and peak deflection occurs at the plate midpoint as per beam theory.

Hydroelastic Interaction Regimes

The hydroelastic interaction regimes as explained in Figure 5 are characterised based on the ratio of the wetting time t_w and the wetted first natural period T_w of the structure. In this manuscript, R is used in the broader context of the hydroelasticity factor. The analytical theories developed by Faltinsen [24] and Stenius [88] were used to classify hydroelasticity, denoted by R_F and R_S respectively. Both theories capture the same physical quantity, however, R_F represents a non-dimensional scaling and R_S is scaled with the boundary conditions. The classification of the hydroelastic interaction regimes in both works is summarised in Figure 12. The DAF as defined in (1) is plotted on the vertical axis as a ratio of the maximum measured experimental strain and the strain obtained via the quasi-static approach using beam theory at the centre of the plate. The strain ε was chosen specifically for the DAF in Figure 12 due to the direct strain measurements from the strain gauges.

$$\text{DAF} = \left. \frac{\varepsilon_{\text{experimental, max}}}{\varepsilon_{\text{quasi-static, max}}} \right|_{\text{centre of plate}} \tag{1}$$

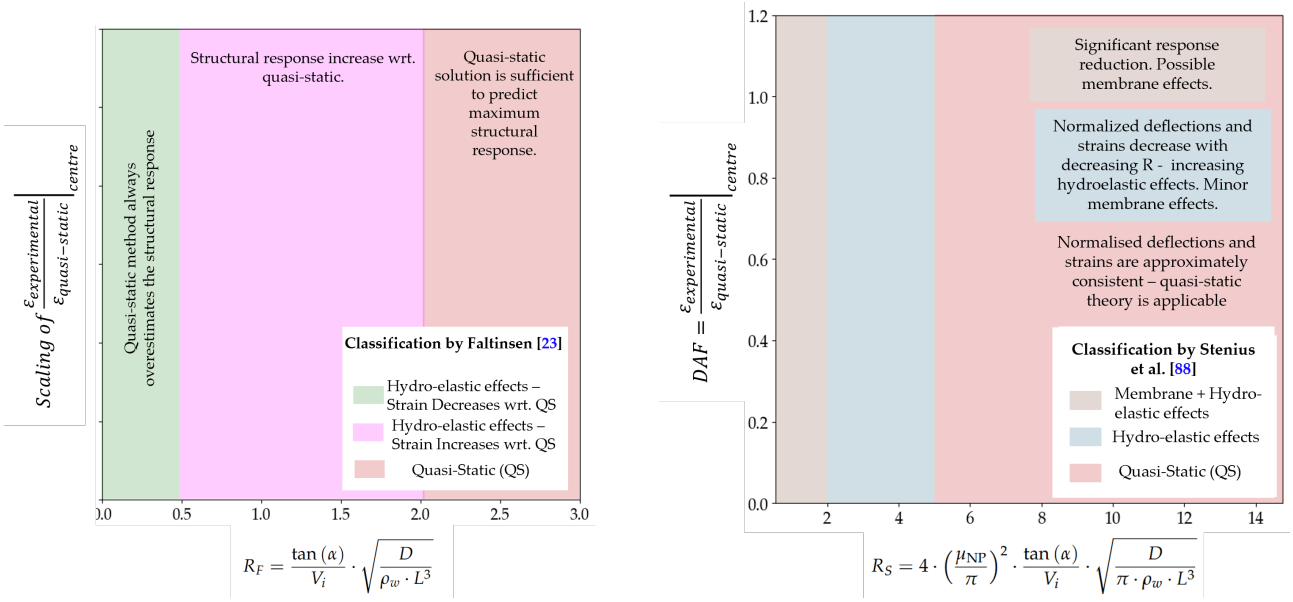

(a) R_F classification [24]. (b) R_S classification [24, 88, 89].

Figure 12: Hydroelasticity regime classification.

Faltinsen [24]

The formulation for R_F in (2) was derived for an orthotropic panel with an aspect ratio of length from keel to chine to width of 1.31 [24]. This theory has been used extensively for the design of hydroelastic slamming experiments. The underlying assumption is that the impact velocity remains constant during impact and that the structure is rigid. The formulation represents a non-dimensional scaling, and thus any constants are omitted. The peak response was experimentally shown to occur

at $R_F = 1$, where the wetting time during the impact is equal to the first wetted natural period of the structure [24]. Beyond $R_F \approx 2$, the strain was shown to converge towards the quasi-static solution. The scaling omits the different boundary conditions and experimental setups, making the formulation applicable across several constructions and boundary conditions [70]. The vertical axis in Faltinsen [24] also shows a non-dimensional scaling of the load. In the present study, the DAF will be used due to the direct usability in a practical context.

The equation for R_F for the non-dimensional structural response is given below, where L is the length between the clamped ends along the chine, ρ_w is the density of water, V_i the impact velocity, α the deadrise angle and D is the plate flexural rigidity. Within D, t_p is the plate thickness, and ν is the Poisson's ratio.

$$R_F \propto \frac{\tan(\alpha)}{V_i} \cdot \sqrt{\frac{D}{\rho_w \cdot L^3}} \tag{2}$$

where

$$D = \frac{E \cdot {t_p}^3}{12 \cdot (1 - \nu^2)} \tag{3}$$

The design criterion given by Faltinsen [24] is that hydroelasticity is crucial for $R_F \leq 0.25$. Hosseinzadeh et al. [35] carried out experiments based on the values of R_F at a similar scale. The response increase was observed between $2 < R_F < 3.5$, citing a weakly coupling between the fluid and structure. Hydroelasticity was shown to be significant for $R_F < 2$.

Stenius [88]

R_S is defined the ratio of loading period T_{LP} and first (wetted) natural period T_{NP}. The notation of T_{LP} and T_{NP} as used in [24] represents the same quantities as t_w and T_W respectively in this manuscript.

$$R_S = \frac{T_{\mathrm{LP}}}{T_{\mathrm{NP}}} \tag{4}$$

Figure 13 shows a simplified schematic of a rigid wedge undergoing an impact into still water, on which this derivation is based.

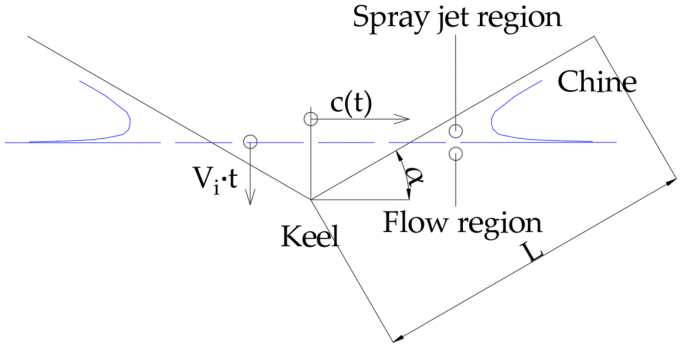

Figure 13: Schematic for c(t) of wedge based on simplified analytical model.

The von Kármán [43] approximation for the wetted half length only considers the geometric properties of the wedge impacting the water under and assumed constant impact velocity, and does not take into account the influence of water jets. In this formulation, α is the wedge deadrise, V_i the impact velocity and t is time of wetting.

$$c(t) = \frac{V_i \cdot t}{\tan(\alpha)} \tag{5}$$

The Wagner [103] approximation of the wetted half length $c(t)$, takes into account the influence of jets by the $\pi/2$ term, but also assumes a constant wetting velocity.

$$c(t) = \left(\frac{\pi}{2}\right) \cdot \frac{V_i \cdot t}{\tan(\alpha)} \tag{6}$$

Hence, the loading period of the panel is given by (7), where the $c(t)$ in (6) is replaced by $L \cdot \cos(\alpha)$. The loading period for complete chine wetting is formulated as the wetting time of the panel multiplied by 2.

$$T_{LP} = \frac{4 \cdot L \cdot \sin(\alpha)}{\pi \cdot V_i} \tag{7}$$

The natural period of the idealized two-dimensional panel is calculated as the first natural period of a beam, which according to engineering beam theory is:

$$T_{NP} = \frac{2\pi}{\mu_{\mathrm{NP}}^2} \sqrt{\frac{(\bar{m} + \bar{m}_{\mathrm{a}})\, L^3}{D}} \tag{8}$$

where μ_{NP} is a boundary condition parameter (simply supported boundaries give $\mu_{\mathrm{NP}} = \pi$, and clamped boundaries give $\mu_{\mathrm{NP}} = 4.73$); $\bar{m}$ is the structural mass; and $\bar{m}_{\mathrm{a}}$ is a uniformly distributed added mass term. The boundary condition parameter is based on the mode shapes under the first resonant mode. The added mass of a high-velocity water-entry of a rigid panel can be approximated using the below relation,

$$\bar{m}_{\mathrm{a}} = \frac{\pi}{2} \cdot \rho_{\mathrm{W}} \cdot (c(t))^2 = \frac{1}{2} k_{\mathrm{a}} \frac{\pi}{2} \rho_{\mathrm{w}} (L \cos(\alpha))^2 \tag{9}$$

Stenius et al. [89] set $k_a = 1$ and assume that the structural mass is negligible with regards to the added mass. Substituting (7) and (8) using (9) into (4):

$$R_S = 4 \cdot \left(\frac{\mu_{\mathrm{NP}}}{\pi}\right)^2 \cdot \frac{\tan(\alpha)}{V_i} \cdot \sqrt{\frac{D}{\pi \cdot \rho_w \cdot L^3}} \tag{10}$$

This formulation is also presented in terms of the maximum added mass which takes place at chine (clamped edge) wetting, and is consistent with (7). Comparison of (2) and (10) shows the that $R_S \approx \gamma \cdot R_F$, where $\gamma = 5.11$ with the additional terms representing the conditions for the clamped-clamped plate. Stenius et al. [89] define the regime between $2 \leq R_S \leq 5$ as the region where hydroelasticity is relevant based on experimental and FEM results as shown in Figure 12. FEM results were specifically used to investigate non-linear membrane effects for the clamped-clamped condition, and these are stated to occur at $R_S \leq 2$. The boundary between the and quasi-static regime between Figures 12a and 12b does not corresponds to the factor γ. This may be explained due to the convergence criteria adopted and limitations with number of available experimental test cases. However, Stenius [88] also note that the results converge below DAF=1 as $R_S \to \infty$ and that the quasi-static solution is never exceeded due to the overestimation in the pressure.

No analytical or non-dimensional formulation to account for the water compressibility effects on a highly flexible structure at design stage was found in literature. Theoretically, the physical effect may be broken down into 2 parts:

1. Reduction of the water density ρ_w, present in the denominator of R_F and R_S. This can be easily calculated with (24) provided that β_g is accurately known. Physically, this represents a reduction in T_w as per (9) in (8) due to plate oscillations in a less dense medium.

2. Change of the wetting time due to impact cushioning effects [98]. For a rigid structure, the duration of keel to chine wetting is expected to increase [113]. However, this effect is more difficult to estimate due to the combined local effects with hydroelastic interaction, which vary across the interaction spectrum.

Therefore, the interplay between density change and delay in impact duration effects the value of R for impacts in aerated water. The implications on the load in the absolute sense, and in the context of the quasi-static solution are the central focus of the present work. The factors of R for several considered plate thicknesses and impact velocities are shown in Figure 14. The experimental conditions were chosen to fit into all hydroelastic interaction regimes, subject to the spatial limitations of the experimental setup.

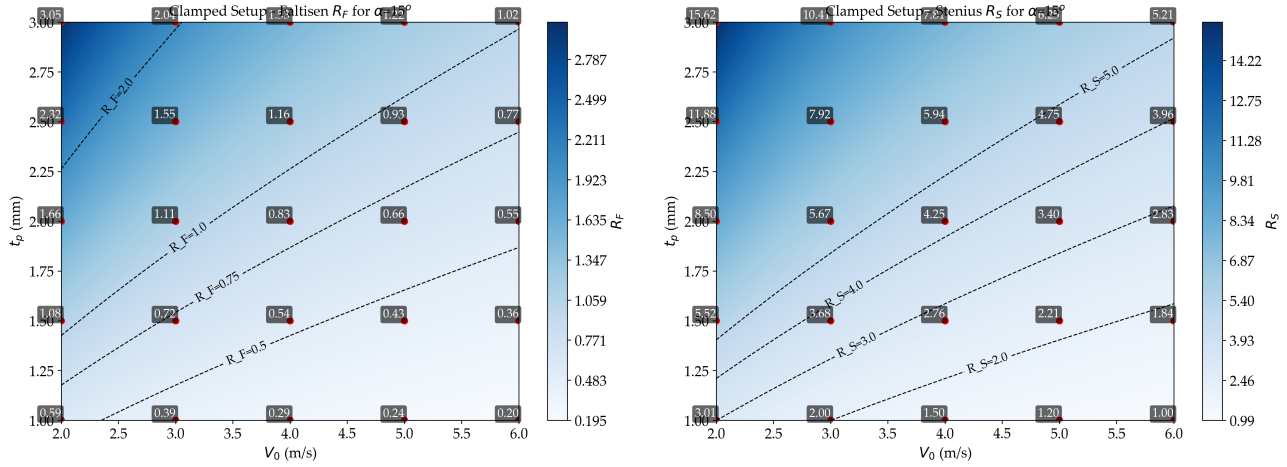

(a) R_F (b) R_S

Figure 14: Hydroelasticity factor R for the considered test conditions.

Deflection and Strain

Analytical calculations of the deflection and strain in the quasi-static condition are important to gauge the expected physical effects on the structure. Furthermore, the quasi-static values of strain as required to calculate the denominator of (1). The load is defined by an average pressure, applied on the structure during the impact, shown in Figure 15. In practice the pressure develops over the length of the plate with the wetting and free surface phenomena, with additional effects due to hydroelasticity. However these effects are ignored for simplification purposes in the quasi-static formulation. Furthermore, there is very limited insight on how the pressure will evolve with hydroelasticity and aeration from previous experimental results.

The spatial pressure distribution across the inner flow region $x \leq c(t)$ is given by (11). This formulation is based on the solution of a boundary value problem satisfying radiation, free surface and body boundary conditions. However, the fluid is considered are incompressible and irrotational. This formulation is adopted for generality with respect to existing literature.

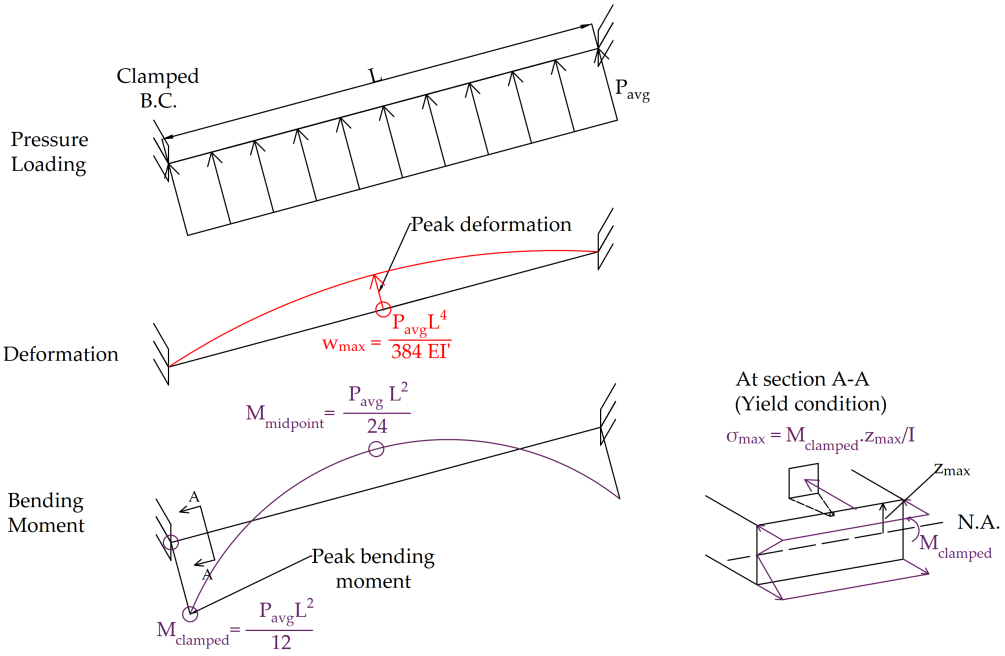

Figure 15: Schematic for analytical deflection and strain calculation.

$$p(t,x) = \rho_w \cdot V \cdot \frac{c(t)}{\sqrt{c(t)^2 - x^2}} \cdot \frac{\mathrm{d}c(t)}{\mathrm{d}t} \tag{11}$$

The design pressure p_d is found by averaging the impact pressure over the wetted length $c_2 - c_1$, where c_2 and c_1 are two arbitrary bounds on the plate with c_1 the lower bound and c_2 being the upper bound for an instantaneous spatial average, as shown in (12)

$$p_d = \rho_w \cdot V \cdot \frac{\mathrm{d}c(t)}{\mathrm{d}t} \cdot \frac{1}{c_2 - c_1} \cdot \int_{c_1}^{c_2} \frac{c(t)}{\sqrt{c(t)^2 - x^2}}\,\mathrm{d}x \tag{12}$$

$$\Rightarrow p_d = \rho_w \cdot V \cdot \frac{\mathrm{d}c(t)}{\mathrm{d}t} \cdot \frac{c}{c_2 - c_1} \cdot \left\{\arcsin\left(\frac{c_2}{c}\right) - \arcsin\left(\frac{c_1}{c}\right)\right\} \tag{13}$$

To obtain the average pressure at complete chine wetting, c_1 was set to 0, this being the wetted length just before the slamming event occurs, and c_2 set to c. The design pressure is obtained by (14).

$$p_d^{max} = \rho_w \cdot V \cdot \frac{\mathrm{d}c(t)}{\mathrm{d}t} \cdot \left(\frac{\pi}{2}\right) \tag{14}$$

The first derivative of either the Von Karman on Wagner wetted length formulation, (5) or (6) respectively, which is a constant, will yield the corresponding derivative of spatially averaged pressure:

$$p_{\text{avg, Von Karman}} = \left(\frac{\pi}{2}\right) \cdot \frac{\rho_w \cdot V_i^2}{\tan(\alpha)} \tag{15}$$

$$p_{\text{avg, Wagner}} = \left(\frac{\pi}{2}\right)^2 \cdot \frac{\rho_w \cdot V_i^2}{\tan(\alpha)} \tag{16}$$

Making reference to the analytical beam theory for the maximum deflection at the centre of the clamped-clamped plate, μ_w is the boundary condition factor and equal to 1 for clamped-clamped (CC) and 5 for simply supported (SS) boundary. In this case, the Wagner [103] pressure from (16) will be used to account for the presence of jets and for consistency.

$$w_{\max} = \mu_w \cdot \frac{p \cdot L^4}{384 \cdot D} = \mu_w \cdot \frac{p_{\text{avg, Wagner}} \cdot L^4}{384 \cdot D} \tag{17}$$

μ_ε is the boundary condition factor and is 1 for the clamped-clamped (CC) boundary condition and 1.5 for a simply supported (SS) boundary.

$$\varepsilon_{\text{max, clamped end}} = \mu_\varepsilon \cdot \frac{z_{\max} \cdot p_{\text{avg, Wagner}} \cdot L^2}{12 \cdot D} \tag{18}$$

where $z_{\max}$ is the maximum perpendicular distance from the neutral axis to the plane surface. Substituting (16) into (18), the formulation for the quasi-static maximum strain at the clamped ends is:

$$\varepsilon_{\text{max, clamped end}} = \mu_\varepsilon \cdot \frac{z_{\max} \cdot \rho_w \cdot \pi^2 \cdot L^2 \cdot V_i^2}{48 \cdot D \cdot \tan(\alpha)} \tag{19}$$

The heat maps in Figure 16 were set up for DC-01 steel to determine the quasi-static structural response. For the clamped-clamped beam, the maximum stress at the clamped ends given by (16) is the failure condition which limits the usability of the experiment assuming uniform load application. The test matrix was set up accordingly to avoid premature failure at the clamped ends while ensuring hydroelastic effects at the centre of the plate are observed.

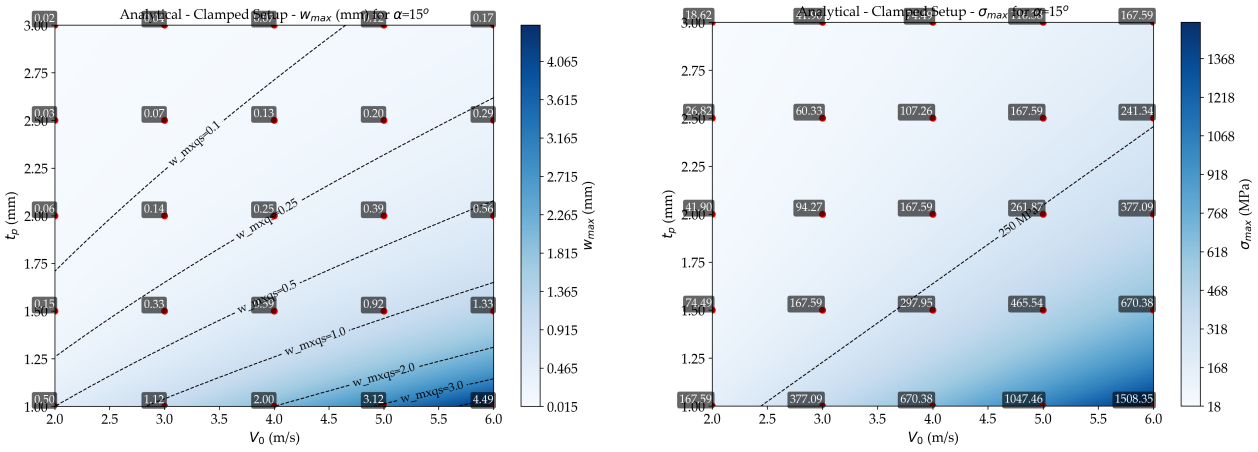

(a) Maximum deflection at the midpoint.

(b) Maximum stress at the clamped end.

Figure 16: Quasi-static structural response for the conditions in Figure 14.

The test conditions and the respective hydroelasticity classification are shown in Figure 17. The lines along the length of the y-axis are only symbolic, with the position on the x-axis being of interest.

3.2.2 Physical and Practical Approach

The wedge was designed for ease of assembly and manufacture. A mock-up was initially constructed out of 2 mm corrugated cardboard sheets. Additional considerations were also made for the optical

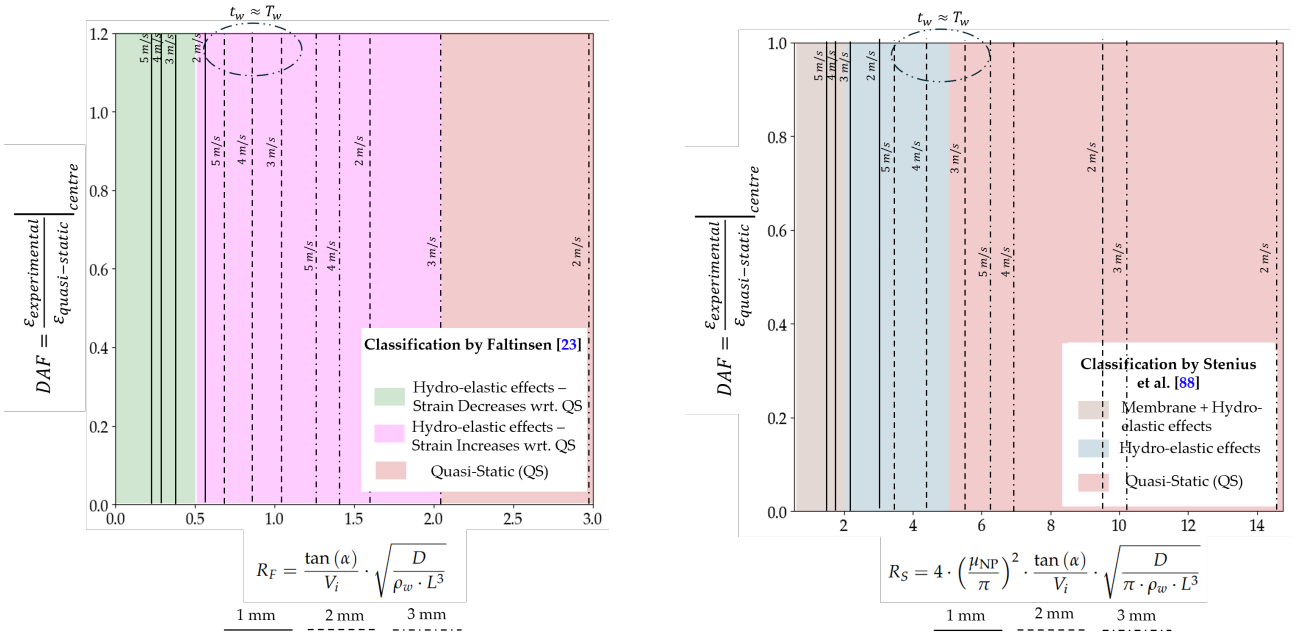

(a) R_F (b) R_S

Figure 17: Test condition classification per interaction regime.

setup viewing angles. The model was tested with different camera angles and lighting arrangements. The following considerations were made for ease of assembly, manufacture and experimental changeover. The complete working drawings for the wedge and further technical details are presented in Appendix 1.

- The main wedge body was constructed out of 4 mm Berken Triplex sheets to facilitate laser cutting and interface with the aluminium L profiles. The sheets were fastened and glued to each other. This method avoids machining into the surface of the wood.

- 4 mm guide rails were used for added structural rigidity. Threaded rod and bearing positions were chosen to prevent excessive swinging which could result in missing the entry into the water tank. Multiple holes for the threaded rods were drilled for positional modularity.

- 12 mm diameter bearings were used with 0.5 mm clearance on each side. This value was determined from experience with previous falling wedge experiments.

- The stiffener at the carriage top was designed to prevent L profile misalignment during descent and impact while not compromising the DIC system field of view.

- Modular design allowing for efficient attachment and removal of plates. The setup enables time-effective assembly, utilizing a single wedge body compatible with interchangeable plates of varying thicknesses, thereby ensuring reusability for future experimental configurations.

- The bottom plates were mechanically fastened to the wedge with countersunk bolts to avoid the additional hydrodynamic interference should the bolts stick out.

- The entire assembly was painted black for visibility and to seal the wood against water damage.

- A layer of tape was finally applied to seal against water ingress. This will not cause a stiff connection like the clamped ends, and thus the assumption of free ends is still valid.

3.3 Choice of Experimental Parameters

In this section, the experimental parameters chosen are justified in the context of the methodology detailed in Section 3.2.1. The aeration percentage β_g and impact velocity V_i are controlled indirectly, as explained in Sections 3.6.6 and 3.7.2 for the aeration and 3.7.3 for the velocity. This section only focuses on the choice of the parameters, the relevance to the research gap and other practical considerations.

Deadrise Angle

The deadrise angle α governs the wedge construction. An angle of 15^o was chosen due to the existing experimental results at this angle, enabling verification of impact pressures, velocities and acceleration for the case with the rigid plate from the experiments by [98]. The deadrise value is crucial for determining the predicted hydroelastic effects.

Impact Velocities

The impact velocities and plate thicknesses were chosen within the bounds of material availability and maximum achievable velocity due to fall-tower height. Impact velocities of 2-5 m/s were tested for plate thicknesses of 1-3 mm to ensure the entire hydroelasticity range is captured for complete quantification of the aeration effects. Impact velocities beyond 3 m/s for the 1 mm plate were anticipated to cause yielding at the clamped boundary. However, during the experimental campaign, no plastic deformation at macro scale was detected using feeler gauges, and subsequently, higher velocities were used.

Aeration

The impact velocity and air fraction ranges were chosen such that Ma_{edge} is in the region where compressibility has a relevant effect on the impact pressure [22]. Furthermore, the air fraction values were restricted by the physical limitations of the aeration system.

$$\text{Ma}_{\text{edge}} = \frac{V_i}{\tan(\alpha) \cdot c_f} \tag{20}$$

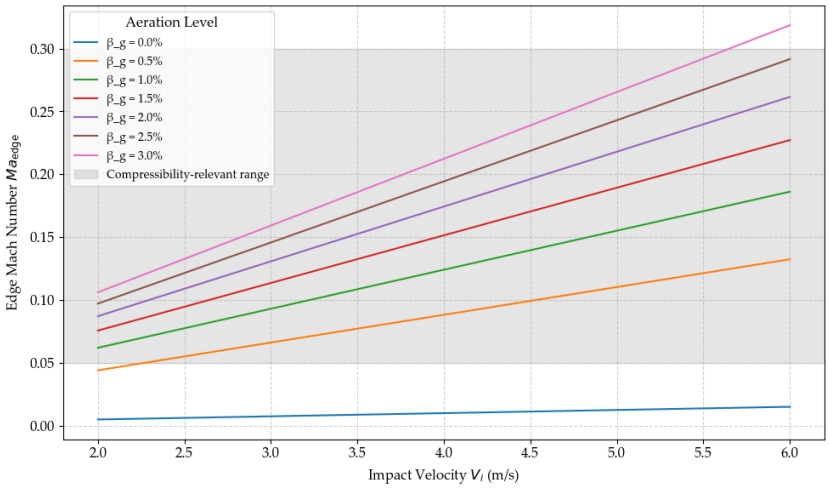

Figure 18: Compressibility Range. $\beta_g = 0 - 2\%$ were used.

The speed of sound in the homogenous fluid consisting of aerated water c_f was computed via the

equation for speed of sound in homogenous mixtures, as per Wood [112], given by (21), where β_g is the percentage of aeration in the aerated water mixture, and subscripts a and l represent pure air and pure water respectively.

$$\frac{1}{\rho_f \cdot {c_f}^2} = \frac{\beta_g}{\rho_a \cdot {c_a}^2} + \frac{1-\beta_g}{\rho_l \cdot {c_l}^2} \tag{21}$$

Values for c_f with ρ_w=1000 kg/m^3, ρ_a=1.225 kg/m^3, c_w=1488 m/s and c_a=343 m/s are presented in Table 2. Additionally, the expected frequencies of the pressure oscillations can then be found as $f_c = c_f/(2 \cdot L_d)$ where L_d is the typical size of the domain such as water depth is 0.5 m.

Table 2: Calculated speed of sound c_f for various gas volume fractions β_g.

β_g **(%)**	0.5	1.0	1.5	2.0	2.5	3.0	3.5	4.0
c_f **(m/s)**	169.10	120.26	98.55	85.61	76.79	70.30	65.26	61.21
f_c **(Hz)**	169.10	120.26	98.55	85.61	76.79	70.30	65.26	61.21

van der Eijk and Wellens [98] reported that the largest changes in impact pressures were found in the range $0.05 < \mathrm{Ma}_{\mathrm{edge}} < 0.3$. The aeration fractions used were ensured to satisfy this criterion, shown in Figure 18.

3.4 Improvements

The following improvements were made to the setup with respect to previous experiments:

- Use of a sharp needle system to measure the water level between subsequent runs. Surface tension makes the change in water surface visible due to very sharp single point contact between the needle and the free surface. The needle is shown in Figure 67.
- Aeration measurements using an indicator in the front of the tank. This approach minimises parallax errors and captures the aeration at the zone of initial impact with the water. The methodology is explained in Section 3.7.2.
- Logging the aeration controller voltage in the DAQ for more complete record keeping and better repeatability.
- Minimum possible attachments to the plate to simplify manufacturing and to reduce the additional vibrating mass in comparison to previous experiments in [32]. Sensors were made waterproof instead of manufacturing waterproof housings.

3.5 Limitations

3.5.1 Experimental Design Limitations

- In principle, the location of peak stress is the clamped end, whilst the location of interest is at the plate midpoint. The design accounts for the trade-off between ensuring sufficient hydroelasticity while ensuring that the plates do not fail from the clamped end.
- Neglecting membrane effects at experimental design stage led to an over-prediction of the strain and thus the limiting condition of the plate. Consequently, for such conditions of flexibility, in

numerical modelling, a higher order model such as the Föppl–von Kármán (FvK) plate theory must be used [29, 43]. This model couples bending and in-plane stretching.

- At the experimental design stage, the influence of aeration is not accounted for.
- Analytical theories are limited to a uniform pressure distribution. However, the pressure will develop over time and is not applied in a single instant to the plate.
- Stainless steel plates were not used despite being more suitable for underwater testing. The key limitation was strain gauge availability. Strain gauges have a material specific temperature compensation, as indicated by the last 2 digits -XX of the product code. Due to the anticipated temperature change between the lab environment and the water in the domain box, using material inappropriate strain gauges will result in significant distortions of the measurements and a complicated procedure for the correct temperature compensation.
- The water ingress from the gap at the fore and aft at the wedge was more severe than expected, and thin layer of tape was used to prevent this during the initial impact phase such that the DIC measurements were not distorted. The tape was not anticipated to substantially increase the stiffness of the connection with respect to the clamped ends, and thus the carriage setup can still be considered as 2D.

3.5.2 Physical and Practical Limitations

- The leading edge was not chamfered. Minimal hydrodynamic interference was expected on the pressure force because water is not separating sharply. However, the leading edge occupies less than 1 % of the total surface area, and it as not possible to quantify this effect.
- The housing for the pressure sensors will affect the plate properties due to a mass addition. The influence is expected to be more pronounced for thinner plates where relative housings mass is higher relative to the plate mass. No workaround was possible as the pressure sensors must be mounted in a flush position to the surface of the plate.
- The utility of the setup is limited for impacts until chine wetting is complete, beyond which complete submersion of the open top wedge will occur.

3.6 Instrumentation

In this section, a detailed overview of the instrumentation system used, the mounting and the interfacing is provided. Considerations behind the placement of instrumentation systems, calibration and sanity checking of outputs are explained in detail. A high-level overview of the entire instrumentation system is provided in Figure 19.

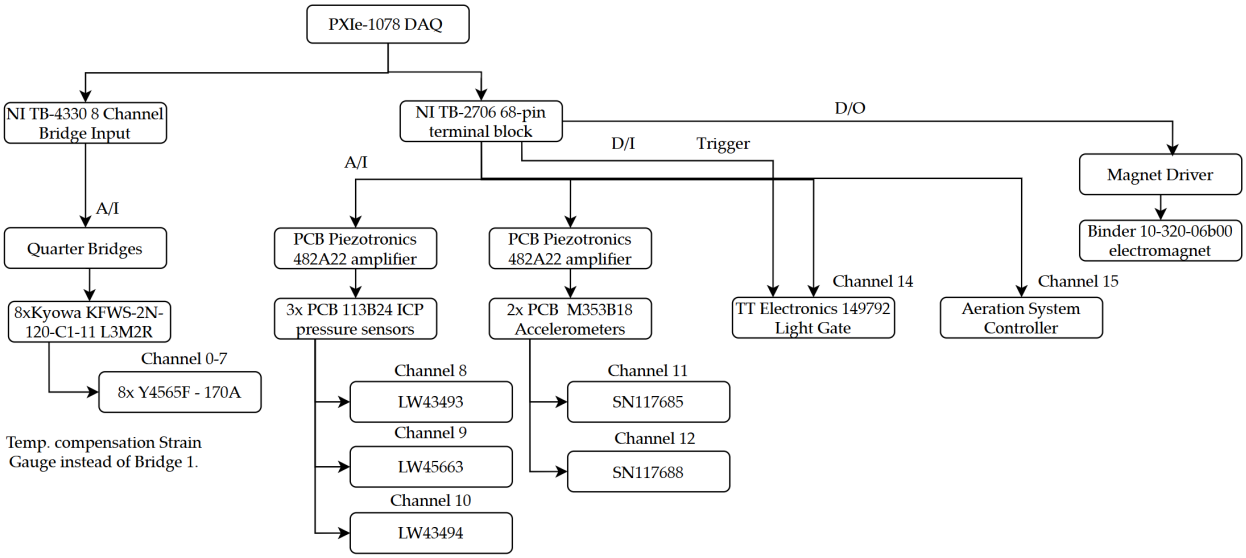

Figure 19: Instrumentation system interfaces.

Table 3: Instrumentation summary.

Instrument	Qty	Manufacturer	Model	Range	Resolution
Pressure sensor	3	PCB Piezotronics Inc.	113B24 ICP	0–6895 kPa	0.035 kPa
Accelerometer	2	PCB Piezotronics Inc.	M353B18	±500 g	0.05 m/s^2 rms
Strain gauge	9	Kyowa	KFWS-2N-120-C1-11	$\leq$ 5% strain	1 μm/m
Camera	1	Basler	Ace acA1920-150uc	9.22 × 5.76 mm sensor	1920 x 1200 px
High-Speed Camera	2	Limess	Photron Fastcam SA-Z	20.48 × 20.48 mm sensor	1920 x 1200 px

3.6.1 Data Acquisition

A National Instruments PXIe-1078 DAQ [66] was used for measurement synchronisation. A National Instruments NI TB-4330 8 Channel Bridge Input [63] and an NI TB-2706 68-pin terminal block [62] were connected to the DAQ to receive the sensor inputs. Two PCB Piezotronics 482A22 4 Channel Line Powered Signal Conditioner [78] were used for the Piezotronics sensors. One unit was allocated to the pressure sensors and the other to the accelerometers.

3.6.2 Strain Gauges

Kyowa KFWS-2N-120-C1-11 L3M2R Small-type Water-proof Strain gauges [53] were used. These strain gauges have CuNi alloy foil resistive element and a polyamide base, and have a specific waterproof coating resultant in suitability for prolonged underwater measurements. This approach was deemed as more suitable rather than waterproofing strain gauges in house. The linear expansion coefficient of 11×10^{-6} ^oC, specifically for steel. As explained in Section 3.2, strain gauge availability due to temperature compensation affected base plate material selection. CC-33A adhesive was applied for temperatures between -10 to 80^{o}C as per manufacturer recommendations [52]. Once the

strain gauges were applied, a final layer of paint was applied to seal the gaps between the strain gauges and the paint protecting the steel. Strain gauge positions were chosen such as to capture the strain propagation in symmetry about the centreline on the instrumented plate and the strain development from keel to chine. In addition, one strain gauge at 90 ^{o} was added to take measurements for longitudinal strain to assess the two dimensionality of the setup.

Table 4: Strain gauge specifications [53].

Parameter	**Value**
Type	KFWS-2N-120-C1-11L3M2R
Gauge factor (24°C, 50%)	2.12 $\pm$ 1.0 %
Gauge length	2 mm
Gauge resistance (24°C, 50%)	120.4 $\pm$ 0.4 Ω
Adoptable thermal expansion	11.7 PPM/°C
Quantity	10
Applicable gauge cement	CC-33A, EP-340
Temperature coefficient of gauge factor	+0.008 %/°C
Lot No.	Y4565F
Batch	170A

3.6.3 Pressure Sensors

Three 113B24 ICP pressure sensors [77] from PCB Piezotronics were used. The attachments were adapted such that the pressure sensors are flush with the bottom plate. Specially designed housings were used. The same housings were kept for different plate thicknesses to minimise fabrication time. The pressure sensors were waterproofed such as to allow for complete immersion and prevent the use of complex housings such as those used by Hendriksen [32]. Additional housings are anticipated to affect the structural properties of the plate. Housings were manufactured to 10 $\pm$0.001 mm diameter. The holes were laser cut to 9.5 mm and reamed to 10 mm.

The following calibration properties for pressure sensors were used. These were obtained via calibration certificates from August 2019.

Table 5: Pressure sensor calibration details.

Reference	**Part Number**	**Sensitivity (kPa/mV)**	**Linearity % FS**	**Uncertainty** $\pm$%
P1	LW47339	1.386	0.2	1.3
P2	LW43493	1.418	0.07	1.3
P3	LW43494	1.384	0.06	1.3

3.6.4 Accelerometers

Two of the M353B18 piezoelectric ICP accelerometers [76] from PCB Piezotronics were used. These accelerometers have a maximum measuring range of ±500 g, which can capture all of the decelerations as per the results of van der Eijk and Wellens [98]. One accelerometer was mounted directly onto the plate, as shown in Figure 20, and the other to the carriage to capture the rigid body deceleration, shown in Figure 21b, and the other was mounted . The accelerometer was employed to monitor the rigid-body motion of the wedge, in contrast to using a displacement sensor as in van der Eijk and Wellens [95], due to the relative ease of numerical integration compared to differentiation.

This approach was experimentally validated by Ren et al. [86], and as a result, a potentiometer for position tracking was deemed unnecessary and omitted.

The manual in [76] details the different accelerometer mounting configuration and the corresponding high-frequency response effects. As mass is added to the system or as mounting stiffness is reduced, the high frequency response is shown to be compromised due to a higher sensitivity variation. The accelerometer will be mounted onto the base plate using an adhesive mount, which is the most direct possible mount directly onto the plate, excluding the approach of threading it directly. Hendriksen [32] makes use of a specific attachment that was bonded on top of the plate, with a specific housing for waterproofing. In the current approach, the accelerometers were directly waterproofed such that complete immersion is possible.

For static calibration, the accelerometer was first placed on a flat, level surface. A properly functioning sensor should register approximately 1 g (9.81m/s²). The sensor was then rotated upside down, at which point it should read approximately -1g.The dynamic calibration results by Hendriksen [32] were found to be unsuitable as the pendulum used for calibration only registered 1% of the measurable acceleration. A decision was taken to rely on the manufacturer's specifications for a quantification of the uncertainty, highlighting an additional limitation.

Table 6: Accelerometer calibration details.

Mounting	**Serial Number**	**Sensitivity (m/s²/V)**
Plate	SN117686	956.0
Carriage	SN117688	919.1

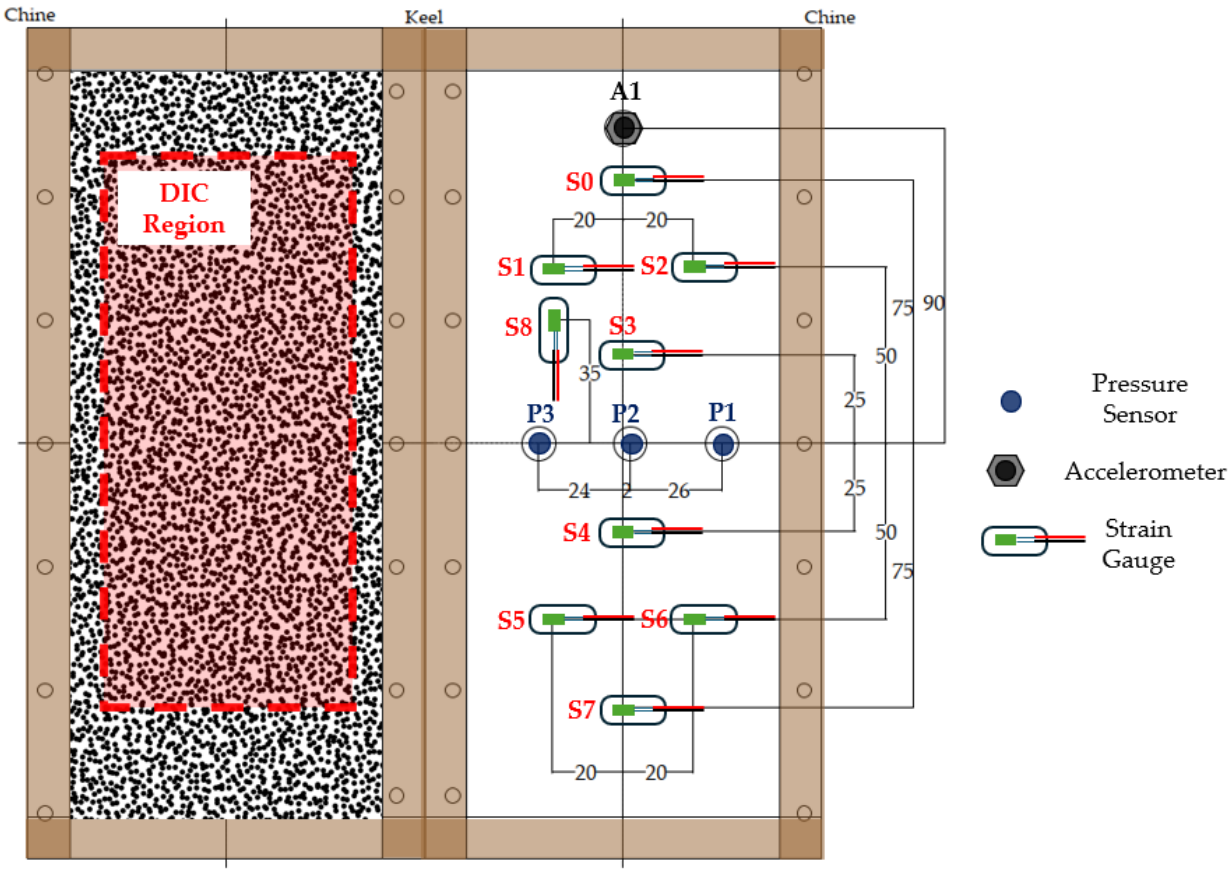

Figure 20: Sensor placement on instrumented wedge bottom.

3.6.5 Light Gate

A Binder 10-320-06b00 electromagnet was mounted to the top of the fall tower to hold the wedge in place at a predetermined height. This was connected to the DAQ such as to be triggered manually once the systems was armed for measurement, as explained in Figure 19.

One TT Electronics 1497921 [93] light gate was used to measure the velocity and to trigger the camera system. The light gate was triggered via a 3D printed trigger mounted onto the rigid carriage, shown in Figure 21.

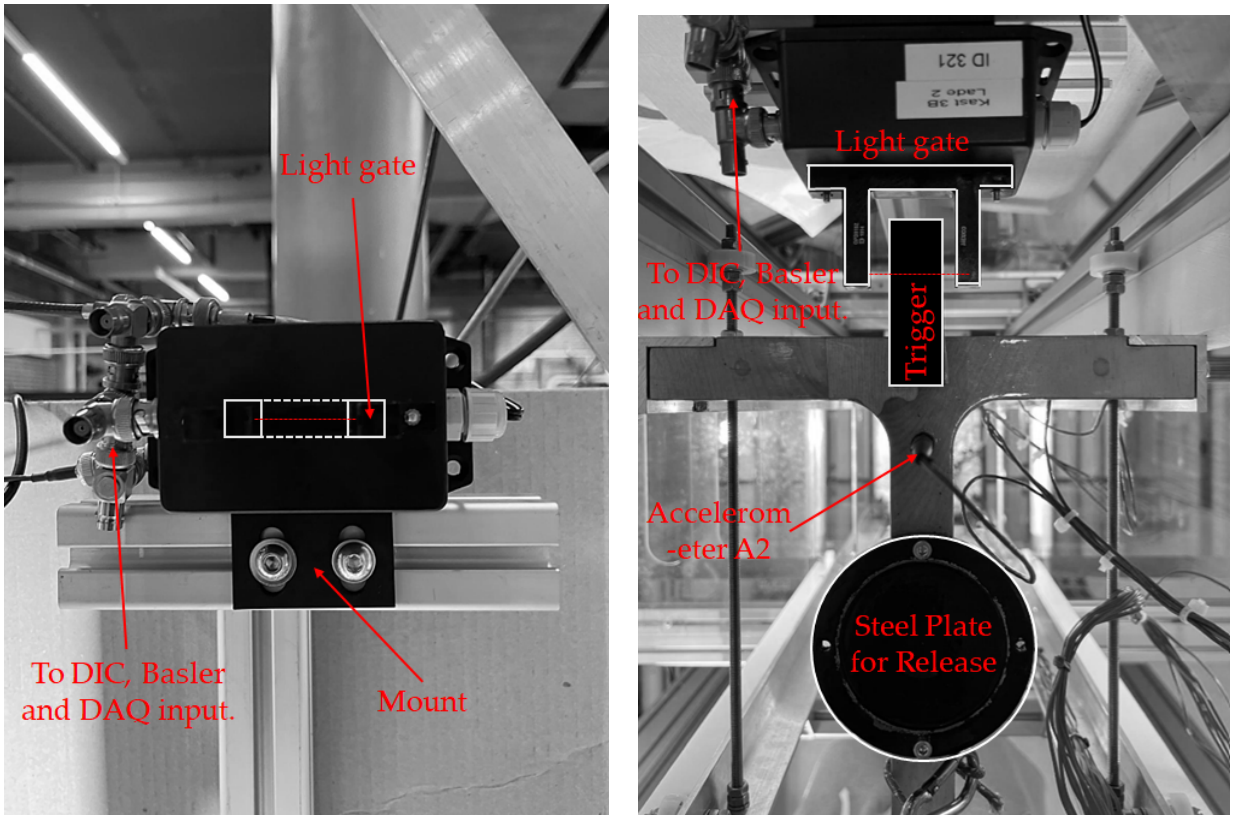

(a) Triggering front view.

(b) Triggering top view.

Figure 21: Instrumentation system physical triggering.

A sampling rate of 100 kHz was used with a trigger wedge of 10.5 ± 0.01 mm, as measured using a vernier calliper. This length of trigger was selected such that at this sampling rate, triggering would be instantaneous while acquiring a sufficient range of samples over which to average the velocity of the impact. The correlation between drop height and impact velocity is explained in further detail in Section 3.7.3. The approach for velocity calculation is detailed in Appendix 3.4.

3.6.6 Aeration

The aeration system consists of air at high pressure being diffused through the water through 16 Pentair AS23S diffusers [79] at the bottom of the domain box tank. A schematic of the air flow through the aeration system is shown in Figure 27b. The key challenge related to this system is to correlate a input voltage with a flow rate and with the percentage of aeration β_g.

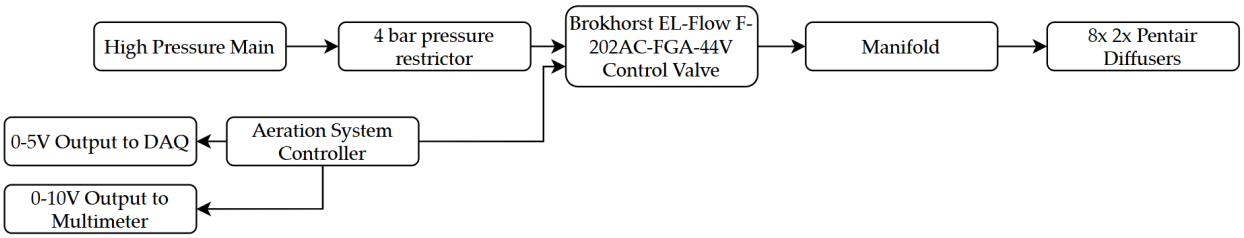

Figure 22: Schematic of aeration distribution system.

The manifold was used for consistent air pressure and flow distribution through the diffusers. This approach to aeration was used in previous works [99, 100] albeit vulnerable to leaks. Consequently, the manifold and subsequent connections to the piping for the air were sealed off. The pressurised air was supplied through the manifold through the Brokhorst EL-Flow Control Valve [9], with a flow rate range of 0 to 5 kg/hr of air at 4 bar. This was controlled with a potentiometer, with the output voltage ranging between 0 and 5 V measured through the analoge DAQ port.

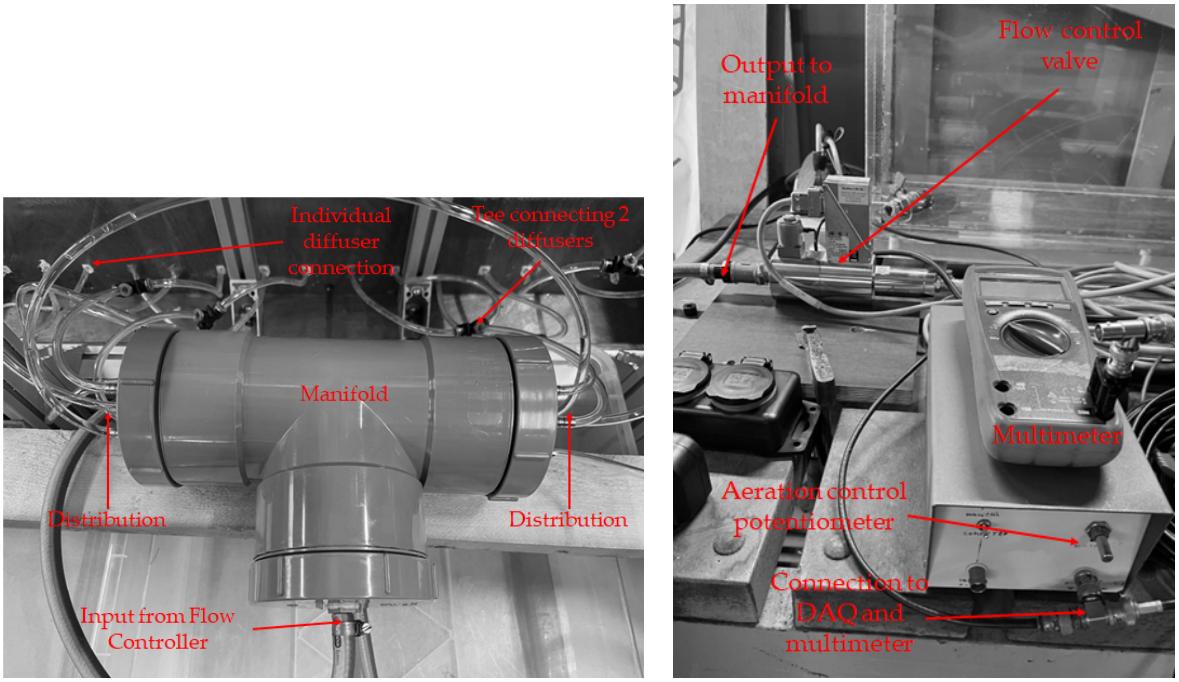

(a) Aeration distribution manifold.

(b) Aeration control equipment.

Figure 23: Aeration system.

A Festo SFAB-1000U-HQ10-25V-M12 Flow Meter [27] was also tested between the flow meter and the manifold. However, this was not found to be very accurate due to a range of up to 1000 L/min, with the range of flow rates expected being less than 5% of the maximum rating. Furthermore, the uncertainty due to resolution was found to be insufficient for an accurate correlation to β_g. Furthermore, the flow controller is designed for air. In the instance of water seeping back into the aeration piping system, the controller did not provide accurate measurements.

The correlation between aeration system input and output is explained in detail in Section 3.7.2.

3.6.7 Wiring and Cable Routing

The pressure sensors and accelerometers were wrapped in heat shrink for waterproofing. The cables were routed along the aluminium profiles. Sufficient cable length was ensured such that no snap load is experienced on impact and that sufficient slack is present. The adopted cable routing configuration also ensures that the cables do not obstruct the optical instrumentation system.

3.6.8 High-Speed Camera

The Basler acA1920-150um [3] camera with an Edmund Optics F1.8 58001 lens from Edmund Optics was placed orthogonally to the slamming wedge to capture the free-surface phenomena and estimate the position of the wedge over time. This camera is limited to 200 fps, and thus was only used indicatively.

3.6.9 Digital Image Correlation (DIC)

Overview and Interfacing

Two Photron Fastcam SA-Z [81] high speed cameras were used for the 3D Digital Image Correlation to capture the deformation and strain across the plate in time. While the wedge is falling under rigid body motion, it is also deflecting, and therefore a 3D-DIC setup is needed. The Quantities of Interest (QoIs) are the displacement along z and the bending across the surface of the plate in z' on the local coordinate system. Two cameras are required for such a setup for data capture in 3D [41, 82].

The cameras were connected to the computer via a high-speed internet connection, and to each other as specified in [80]. In addition, both cameras were connected to the TT Electronics 1497921 light gate [93] for simultaneous triggering. Photron PFV 4 software [82] was used for setting the camera properties, for simultaneous recording and for saving the data. The camera connections are shown in Appendix 3.1. Dantec Istra 4D [16] software was used for camera calibration and for data processing. The software provides robust features for uncertainty estimation. The reader is referred to the software manual [16] for further details.

Mounting and Viewing Angles

The camera setup and placement was designed holistically to account for the expected QoIs while ensuring key principles for 3D-DIC are in place. Each stage of the setup was tested thoroughly to ensure quality of optical data capture.

The Stereo Angle is the angle between the two cameras. Smaller stereo-angles lead to better in-plane displacement accuracy, at the cost of increased out-of-plane uncertainty. Alternatively, larger stereo-angles lead to better out-of-plane displacement accuracy, at the cost of increased in-plane uncertainty [41]. For the present case, both types of focus are required. Each camera was placed at 15^{o} to the vertical line, as recommended by Limess [56]. The Pentax EX0C6 C90100 CCTV lens with a C-mount [82] was used due to superior focus on the region of interest and suitable focus capabilities.

A frame was constructed out of ITEM® profiles for a highly adjustable camera setup, as shown in Figure 24. The frame and camera setup was completely isolated from the fall tower to prevent vibrations affecting the optical measurements. The frame also allows for a highly modular setup, allowing adjustments to be made to the optical setup. Modifications were made to the drop tower to retain the stiffness but open up the viewing angles. The design of the wedge, shown in Section 3.2 was also adapted accordingly to ensure good viewing angles.

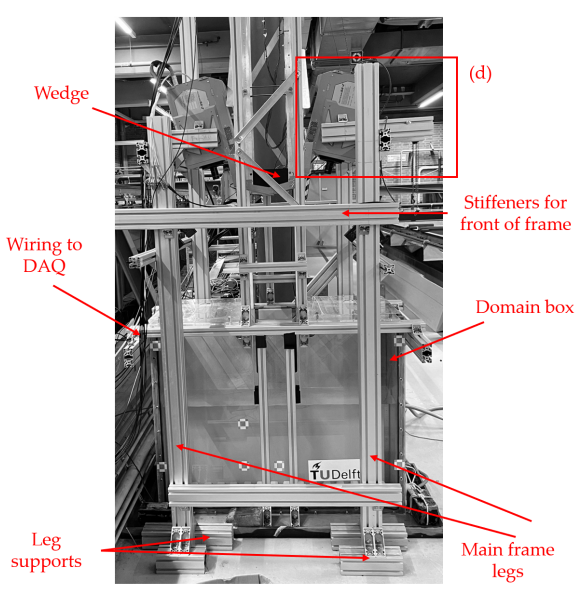

(a) Front view.

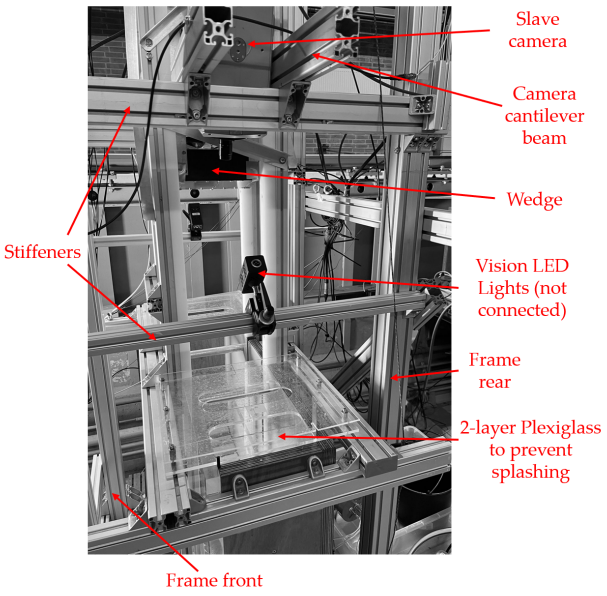

(b) Side view.

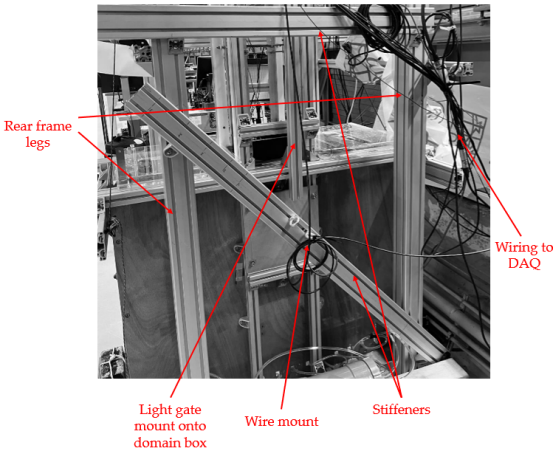

(c) Rear view.

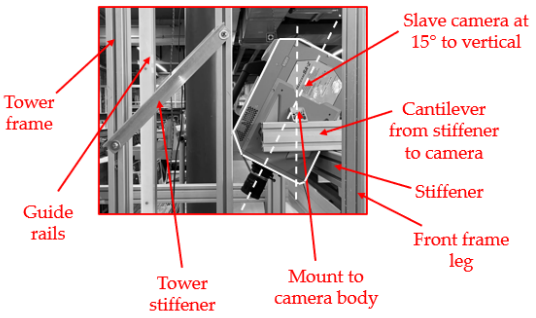

(d) Camera detail.

Figure 24: Overview of frame used for mounting cameras.

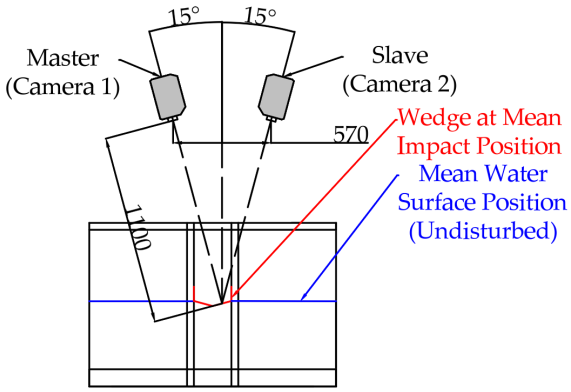

(a) Camera Placement.

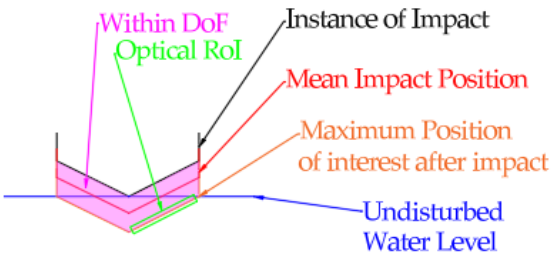

(b) Detail of wedge falling within the DoF.

Figure 25: Detail of wedge falling within the DoF.

The Field of View (FOV), Depth of Field (DoF) and Stereo Angle were taken into account. It was ensured that the entire RoI was visible by both cameras during the entire impact. The mean wedge position during impact, shown in red in Figure 25 was taken as reference, as per [86]. The Depth of Field was calculated for a preliminary indication of the setup suitability. This was also checked practically to ensure that the falling wedge remains in focus throughout the time of interest during the impact.

Calibration

The objective of the calibration step is to derive the setup's intrinsic (e.g. focal length, image centre, lens distortions, skew of each camera) and extrinsic (e.g. relative orientation and position of the cameras) parameters [16, 41]. The calibration was executed with the calibration plate shown in Figure 26. The calibration plate has a high degree of flatness with a known pattern and spacing. The plate was moved around the RoI to cover the DoF as shown in Figure 25b. The initial plate position determines the adopted initial coordinate system [16]. The anticipated deflections perpendicular to the plate in z' are expected to be an order of magnitude smaller than the deflection in the global z direction, as per Figure 16. Consequently, an initial position parallel to the plate deadrise angle was chosen. The calibration plate movements in the RoI are shown in Appendix 3.2-3.3. The calibration was repeated five times to ensure repeatability. Furthermore, the calibration was repeated between changes to the plate.

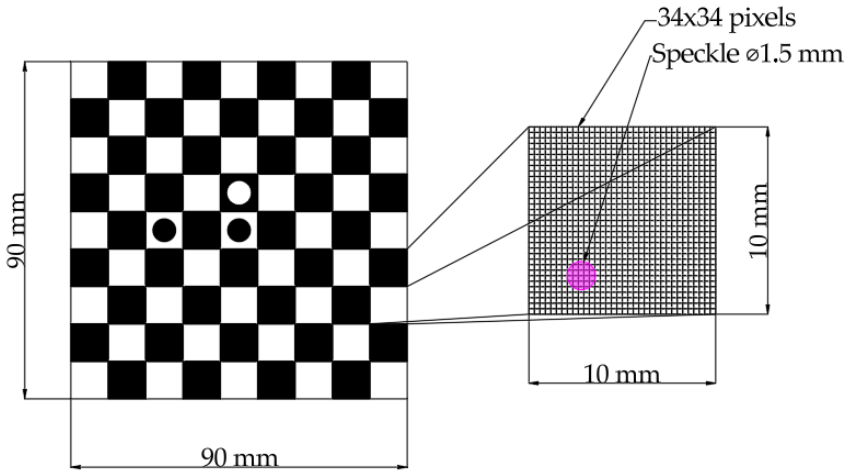

Figure 26: 10x10 mm calibration plate and speckle pattern sizing.

Speckle Pattern Sizing and Application

DIC measurements require a random distribution of circular speckles of uniform size across the region of interest [41]. The speckle size was chosen to ensure each dot was captured by 5–7 pixels, as required by the software algorithm [16, 41, 84]. Calibration with the target in Figure 26 confirmed that speckles of 1.0 mm diameter fulfilled this requirement, and were applied manually using a stippling technique. The pattern density and randomness were verified through preliminary testing to provide sufficient dots per facet balancing resolution and uncertainty.

3.7 Experimental Campaign and Inputs

3.7.1 Test Matrix

The relevant experimental parameters to answer the Research Question are the (1) plate thickness t_p, (2) impact velocity V_i and (3) aeration percentage β_g. The plate thickness is directly set by mounting the relevant plate onto the wedge. The aeration and the impact velocity are indirect inputs. An explanation of how these are obtained and a quantification of the uncertainty is provided in Sections 3.7.2 and 3.7.3 respectively. The order in which the key parameters are listed here represents their complexity with changing between subsequent tests. The longest changeover time is for the plate, due to the complete rewiring of the pressure sensors and strain gauges required. Additionally, a key number of checks and re-calibrations are required to ensure consistency of the setup. Three repetitions were done for each test. This number of repetitions was later found to be insufficient for conditions of high hydroelasticity. The test matrices for the experimental campaign are shown in Tables 7-9. The values of R_F and R_S are displayed for the case with no aeration. Symbolically, no values are presented for the cases with aerated water as these are unknown due to the physical effects.

Table 7: Test matrix for 1 mm plate.

t_p **= 1 mm**		$\beta_g = 0\%$		$\beta_g = 1\%$		$\beta_g = 2\%$	
		R_F	R_S	R_F	R_S	R_F	R_S
V_i **(m/s)**	**2**	0.59	3.006				
	3	0.39	2.004				
	4	0.29	1.503				
	5	0.24	1.202				

Table 8: Test matrix for 2 mm plate.

t_p **= 2 mm**		$\beta_g = 0\%$		$\beta_g = 1\%$		$\beta_g = 2\%$	
		R_F	R_S	R_F	R_S	R_F	R_S
V_i **(m/s)**	**2**	1.66	8.50				
	3	1.11	5.67				
	4	0.83	4.25				
	5	0.66	0.66				

Table 9: Test matrix for 3 mm plate.

t_p **= 3 mm**		$\beta_g = 0\%$		$\beta_g = 1\%$		$\beta_g = 2\%$	
		R_F	R_S	R_F	R_S	R_F	R_S
V_i **(m/s)**	**2**	3.05	15.62				
	3	2.04	10.41				
	4	1.53	7.81				
	5	1.22	6.25				

3.7.2 Aeration Control & Measurement

Overview

The air mass flow rate was controlled via the potentiometer. The potentiometer voltage was correlated to the aeration percentage via a float. The operating principle is shown in the schematic in Figure 27.

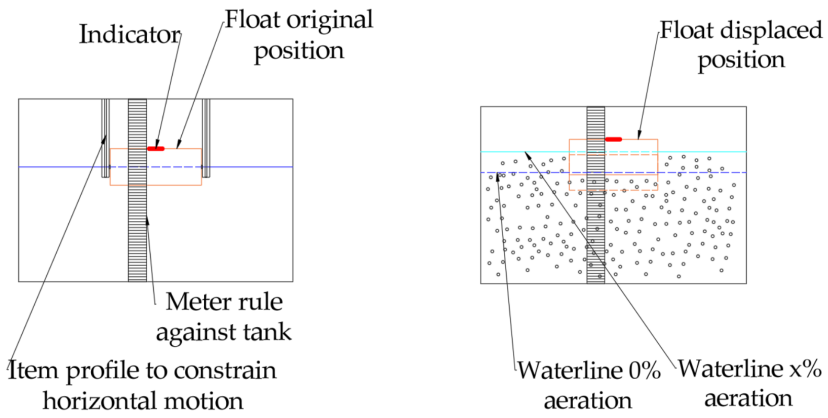

(a) Aeration system off.

(b) Aeration system on.

Figure 27: Aeration measurements via float.

When air is introduced into the system, the water level will change, and the distribution between air and water volume can be estimated. The wedge was placed at the centre of the tank at the point of impact due to this being the region of interest in the fluid domain. In addition, this approach is the farthest away from the sides of the tank, making it least sensitive to edge effects and bubble cloud swirling. Estimating the aeration percentage at other locations in the tank [99] was not found to add value due to the curvature of the water surface as shown in Figure 28, with the region of peak curvature being the region where the impact occurs. This approach therefore assumes that the aeration distribution is constant throughout the region occupied by the float.

Figure 28: Curvature on the water level.

The rise in water level is quantified in Figure 29 by a ruler attached to the external surface of the domain box. A higher water level will result in impact taking place at an earlier time instant and with a slight reduction in impact velocity. Due to the dynamics of the water surface, it was not possible to have the free surface at 0.5 m for all aeration conditions, and thus the case for $\beta_g = 0\%$ was adopted as the baseline.

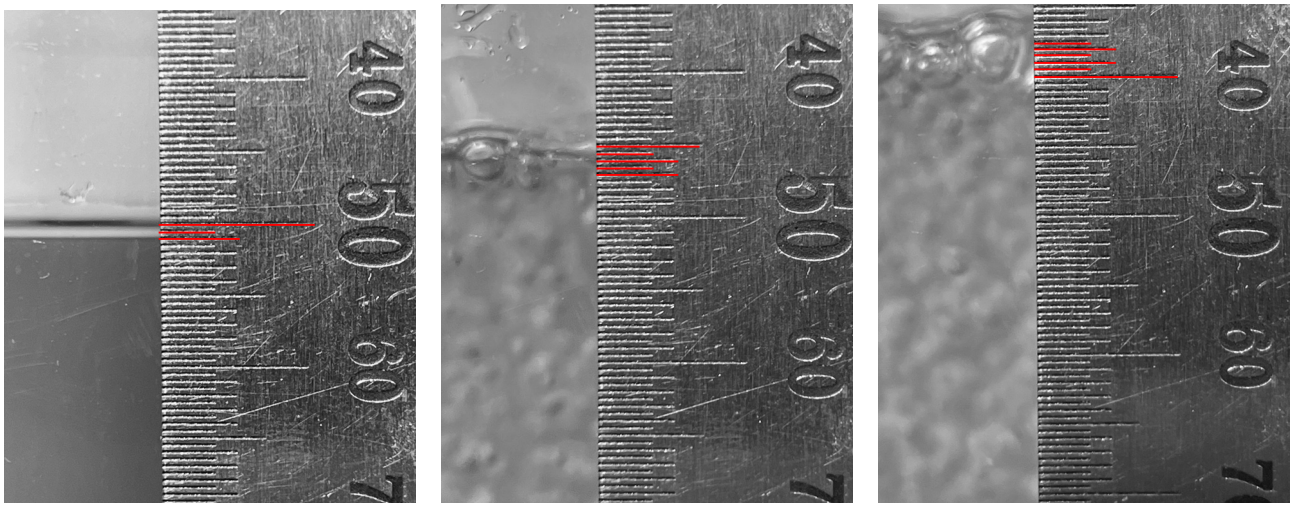

(a) $\beta_g = 0\%$ (b) $\beta_g = 1\%$ (c) $\beta_g = 2\%$

Figure 29: Rise in water level at centre of domain box with aeration system active. Relevant markings on the ruler are emphasized in red.

This approach to measure β_g was selected over techniques making use of the flow rate due to the difficulties with determine the flow rate via a flow meter as explained in Section 3.6.6. Other researchers used an approach based on the time to fill a tube with air [57, 98]. The latter approaches were based on estimates of bubble velocity. In addition, a correlation to the approach with the float could not be made. The strength of the present approach is that no assumptions on bubble dynamics are made and only physical quantities that are directly measured are used. Wu et al. [113] adopted a more sophisticated electronic instrumentation system, and a high-speed camera was used to determine the bubble diameter and velocity. This level of complexity was beyond the scope of the thesis.

Methodology

Using mass conservation for the air and water in the system at a given instant in time under and assumed steady state with no air leakage:

$$M_{\text{water}} + M_{\text{air}} = M_{\text{aerated water}} \tag{22}$$

It should be noted that the diffusers fill with water when no air is present. When air is added to the system, the stones first fill with air before releasing the air to the water. The volume of the air stones should be taken into account, as the volume of air does not contribute to the aeration of the water. The below formulation is found to compute the density of the aerated water:

$$\rho_{\text{water}} \cdot A_{\text{wl}} \cdot h_{wl} + \rho_{\text{air}} \left(A_{\text{wl}} \cdot \Delta h_{\text{wl}} - n_{\text{diffuser}} \cdot V_{\text{diffuser}} \right) = \rho_{\text{aerated water}} \cdot A_{\text{wl}} \cdot h_{\text{aerated water}} \tag{23}$$

where A_wl is the area at the waterline of the foam block, h_{wl} is the height at the waterline and Δh_{wl} is the change in water level with the addition of aeration. The aerated water is composed of β_g

percentage of air and $1 - \beta_g$ percentage of water.

$$\rho_{\text{aerated water}} = \rho_{\text{air}} \cdot \beta_g + \rho_{\text{water}} \cdot (1 - \beta_g) \tag{24}$$

A red pointer was attached to the centre of the foam block, and a meter rule was placed against the surface of the tank. The pointer was centred to avoid a rotational moment in the case of air bubble dynamics. This approach was found to reduce parallax errors that were prevalent in previous measurements. In addition, the pointer was balanced by an additional mass at the aft of the foam block. The block is also held in place by two ITEM® profiles to restrict lateral movement and rotation. In addition, self tapping screws were added between the sides and the item profiles, and the front and the walls of the tanks to minimise frictional forces when the block is rising up and down under influence of aeration.

A multimeter was also connected to the potentiometer to obtain a value for the voltage that is easy to visualise when changing. This value was between 0 and 10 V as per the aeration control box output. The initial position of the pointer was recorded when the aeration system was off. The aeration system was switched on and allowed to settle to steady state such that the position of the pointer had stabilised. The procedure was repeated 3 times for a range of voltages.

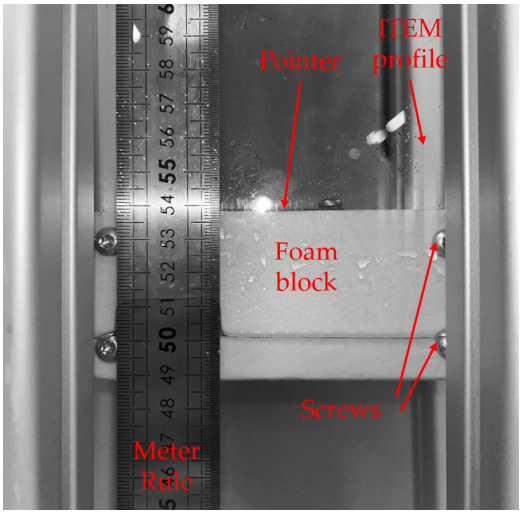

Figure 30: Aeration measurements via float.

Outcome

The following plots was obtained for change in waterline Δh and β_g against the Voltage (V) when systematically varying the voltage in intervals of 1 V. The plots were set to intercept the origin as when the aeration system is off there will be no aeration. A check was performed by setting the voltage to the values expected to give aeration values of 0, 1 and 2% and measuring the change in water height for the float, with a good match smaller than the resolution of the ruler was obtained.

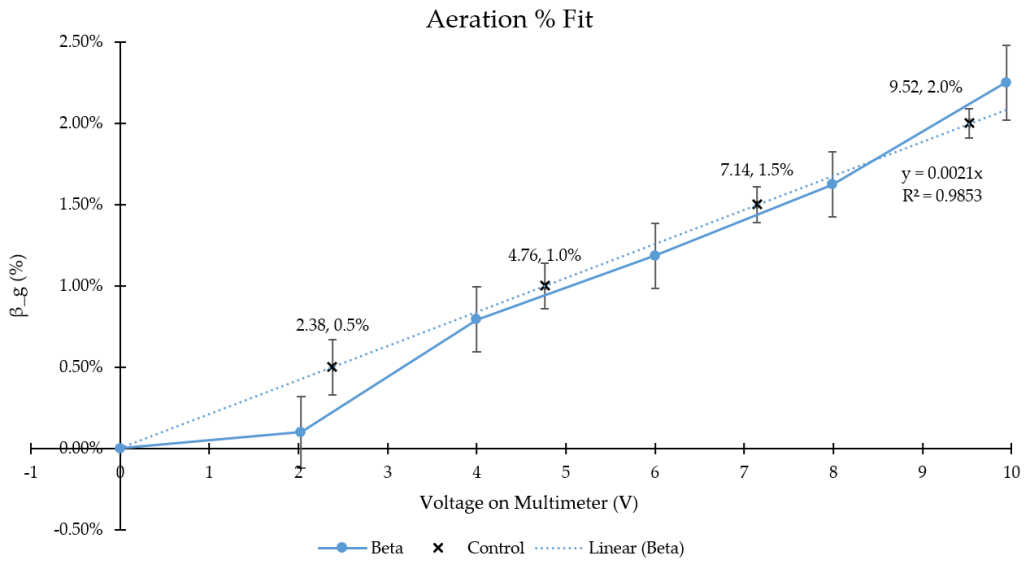

Figure 31: Linear regression for the aeration control system. The points denoted by $\times$ represent the experimental aeration control point.

Consequent, aeration is the simplest input measurement to control due to only requiring a predetermined voltage change. This was chosen as the first variable to vary in the text matrix.

Limitations

It was not possible to correlate the voltages with the percentage of aeration documented in previous tests due to incomplete record keeping. The following limitations to this approach were identified:

- At higher voltages, and thus at the upper threshold for values of aeration, due to the bubble dynamics, it was not possible to attain a completely steady state due to bubble merging and interaction such that pointer allocutions were still observed.
- At lower voltages, and thus at the lower threshold for values of aeration, the resolution by the ruler was a limitation in determining the change in the position of the pointer.
- When turning off the aeration system between tests, time was required to allow water to seep back into the aeration stones for a common datum.
- The air diffusers are assumed to be filled with either water or air. There is no distinction between the empty volume filling with air or water and the solid stone.
- The approach attempts to limit foam block motion to translation in y. The edge effects of bubble space against the front and back of the tank are expected to contribute to the upward force acting on the block, however were not quantified.

3.7.3 Impact Velocity Control & Measurement

The impact velocity depends on the drop height, the air resistance and the frictional resistance between the sides of the tower and the guide rails. The velocity is to be varied by changing the length of the threaded rod which holds the electromagnetic binder, and the release height. The values of velocity obtained by Hendriksen [32] were used as a reference point and the height was subsequently adjusted when conducting several impact tests.

The differences can be explained due to inconsistent contact with the guide rails during the fall, with the influence of friction not being consistent between runs. Including a precise gyrometer to capture the angle during descent with respect to the original position would yield information on the path of descent, and thus the parallelism between the L profiles and the tower.

Table 10: Summary of Impact Velocities and Release Heights.

Impact Velocity (m/s)	2	3	4	5
Release Height $V_i = \sqrt{2 \cdot g \cdot h}$ (m)	0.204	0.459	0.816	1.274
Velocity (3 runs) (m/s)	1.95	3.03	4.16	4.88
Uncertainty (m/s) ($\pm$)	0.015	0.075	0.041	0.05

3.7.4 Experimental Overview

The process followed per test is shown in Figure 32. When triggering the instrumentation system using the light gate, the system was set to collect data for 1 s before the trigger and for 2 s after the trigger pulse. This approach was used to ensure that sufficient data directly before and during the impact is collected without extensive and redundant data.

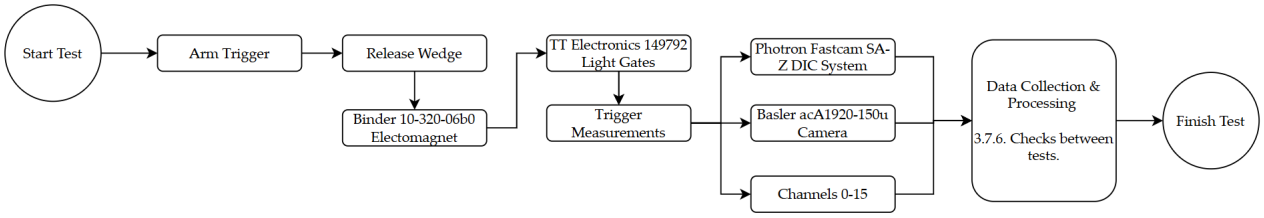

Figure 32: Process followed per individual test.

3.7.5 Procedure Prior to Executing Experimental Campaign

The following points were identified and mitigated during preliminary testing to ensure consistency during the campaign.

- To ensure the DIC cameras were triggered simultaneously, a flash was switched on periodically and the frames checked such that it was visible in the same frame as recorded by both cameras.
- Several test were conducted to determine the number of tests per combination of experimental variables. For higher percentages of aeration and thinner plates, more tests were required due to bubble interaction stochastics.

3.7.6 Procedure between two test runs:

The following checks were carried out between subsequent runs to ensure consistency of the impact region and test conditions.

- The water level at condition of no aeration, and prior to switching on the aeration system, was allowed to settle and was checked using the well calibrated pointer needle shown in Figure 67. For test conditions with a high impact velocity, the water level was topped up as necessary due to splashes.
- Sufficient time for the bubble distribution to stabilise was allowed and that all the diffusers were operational.

- The bottom surface of the wedge was cleaned of excess water. The inside of the wedge was allowed to drain from water. The speckle pattern was completely dried to prevent optical signal distortions.
- All signals were checked to ensure that the instrumentation system is live and that the respective zero values are being read.
- The light gate position relative to the undisturbed water level was checked.
- The lights for the camera system were switched on.
- After each test, the data was checked to ensure that all sensors had operated properly, and that all relevant data had been recorded.
- The camera synchronisation was checked. During calibration, issues were found when turning the cameras on and off, which resulted in errors due to frame mismatch.
- The hammer tests and calibration of the DIC system were redone between plate changes.

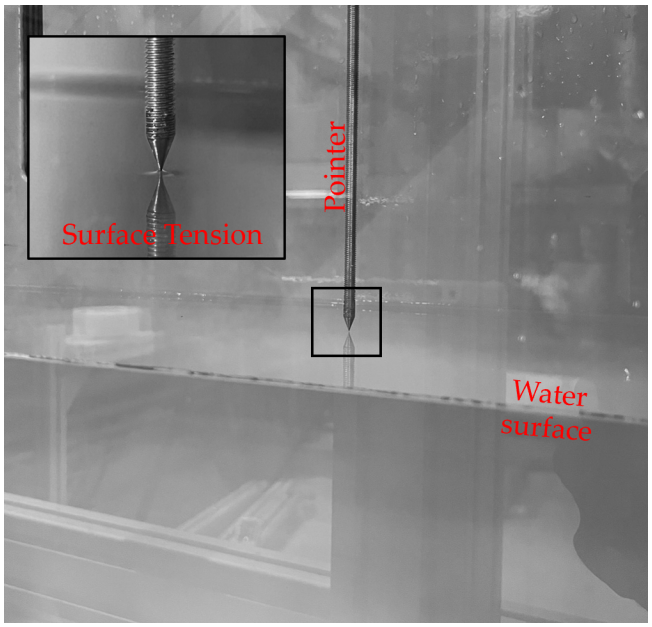

Figure 33: Pointer used to verify free-surface level at calibration position via surface tension.

4 Experimental Results and Analysis

In this chapter, the experimental results are presented and analysed in detail. First, a detailed explanation of how the raw data was handled, processed, filtered and interpreted is provided. The individual results are first discussed in the context of the underlying physical phenomena.

4.1 System Natural Frequencies

Hammer tests were conducted to identify the dominant natural frequencies of the structural components in the experimental setup. The primary objective was to inform the choice of appropriate filter parameters and for subsequent processing, analysis and frequency domain decomposition. Accelerometers were placed on the flexible plate and the rigid carriage, denoted by A1 and A2 respectively. Three repetitions for the wedge suspended in the air and for the wedge in water were carried out. The natural frequency of the accelerometers is $\geq$ 500 kHz [77]. According to the Nyquist criterion, the 100 kHz sampling rate limits the measurable frequency content to 50 kHz [86]. Consequently, the sensor's own resonance was not captured and is not expected to be present in any of the recorded spectra.

4.1.1 Emerged Hammer Tests

The carriage was suspended in the air by a string. This setup isolates the natural frequencies of the clamped–clamped plate–carriage system in the emerged condition, representative of the initial phase prior to water entry. Each plate thickness was subjected to a single sharp hammer strike. The frequency content of the resulting vibration signals was extracted via a Fast Fourier Transform (FFT) as presented in Figure 34. The signal from the accelerometer mounted onto the rigid carriage is also plotted due to the mutual influence by the mechanical coupling at the clamped connections. Effects of contact between the suspended carriage, the fall tower guide rails and the string suspension were unavoidable. These effects could not be quantified in a repeatable and consistent manner. The first hydro-structural natural frequency f_{hs} was estimated as per the methodology in Appendix 2 is also overlaid on the spectra for reference.

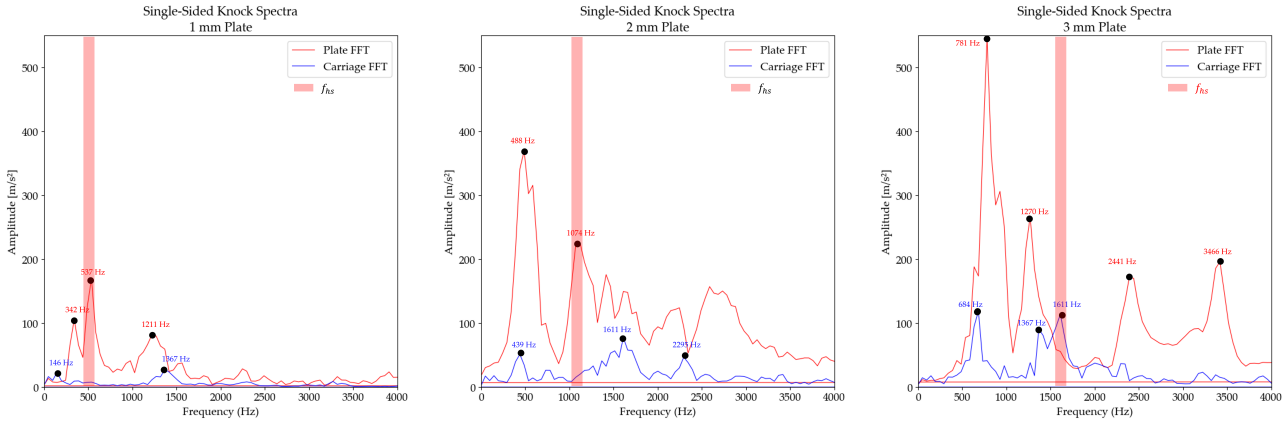

(a) $t_p = 1.0$ mm (b) $t_p = 2.0$ mm (c) $t_p = 3.0$ mm

Figure 34: Knock tests on the instrumented flexible plate in the air.

For the 1 mm and 2 mm plates, the dry natural frequency was clearly captured by the accelerometer mounted directly on the flexible plate. However, for the 3 mm plate, the dry natural frequency appears more prominently in the signal from the accelerometer on the stiffened carriage. This may be attributed to the highest relative stiffness between the 3 mm plate and the stiffened carriage resulting in an effect of the mechanical coupling between plate and carriage. Consequently, the vibration of

the plate is more effectively transmitted to the carriage, leading to stronger detection on the carriage-mounted accelerometer.

Additionally, knock tests were conducted on the tank wall while the wedge was suspended, to isolate structural excitation from the tank and domain box with aeration. The results across $\beta_g = 0 - 2\%$ are shown in Figure 35. A consistent peak at approximately 781 Hz is observed in the sub-figures, and for the submerged knock tests in Figures 36-38 suggests this is the dominant natural frequency of the suspended wedge–carriage–string system. The damping effect of aeration is demonstrated as the higher frequency peaks in the non-aerated case were not detected .The modes in both aeration conditions are identical with the peak at 1600 Hz being damped. Although aeration was expected to slightly influence the frequencies of the natural modes, no change could be detected in the present measurements. This is likely due to limitations of the instrumentation approach, which was not sufficiently sensitive to resolve subtle modal shifts.

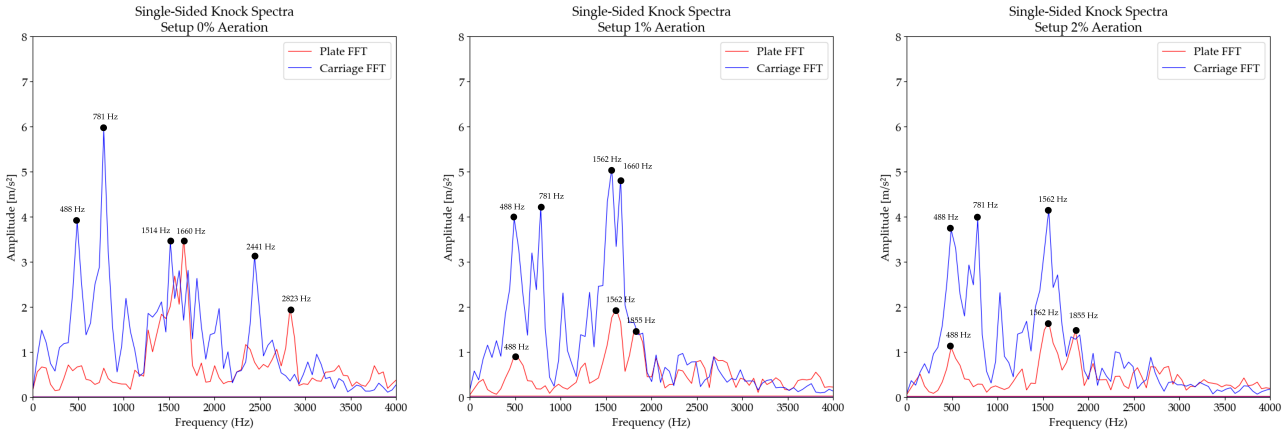

(a) $\beta_g = 0\%$ (b) $\beta_g = 1\%$ (c) $\beta_g = 2\%$

Figure 35: Knock tests on the domain box with carriage in the air.

4.1.2 Submerged Hammer Tests

The carriage with the flexible bottom was submerged in water up to the chines as in the case of complete wetting during impact. These tests aim to investigate how aeration in the tank influences the excitation spectrum transmitted through the system in the wetted condition. Due to insufficient buoyancy, the wedge was held in position by a string which introduced an artificial constraint. The spectra for the different aeration percentages are presented in Figures 36-38. The hydro-structural plate natural frequencies in air f_{hs} and the hydro-elastic natural frequencies including the added mass effects $f_{he,n}$ are also overlaid. The values of aeration were investigated for variance in plate wetted natural frequencies based on the water compressibility. The flexible plates were not struck directly to avoid a disturbance to the bubble flow field introduced by submerging the hammer. Consequently, the hammer impact was applied to the top of the carriage, and the excitation was transmitted through the mechanical assembly.

For the 2 mm plate in Figures 36b, 37b and 38b, the first hydroelastic frequency $f_{he,1}$ is observed to match the peak in the plate FFT spectrum. Furthermore, there is no change to this frequency when introducing aeration. For the 1 mm plate, at $\beta_g = 2\%$, an increase in the plate frequency, shown in the red trace in Figure 38a is observed. This matches physical expectation given the plate is oscillating in a lighter fluid. This effect was not observed for the 2 and 3 mm plate, demonstrating the sensitivity of the thinner plate to slight changes in aeration conditions. As explained previously, the 3 mm plate results in stronger structural coupling with the carriage. However, in this condition, the effects of aeration were not captured, with Figures 36c, 37c and 38c showing a similar spectrum albeit at different amplitudes.

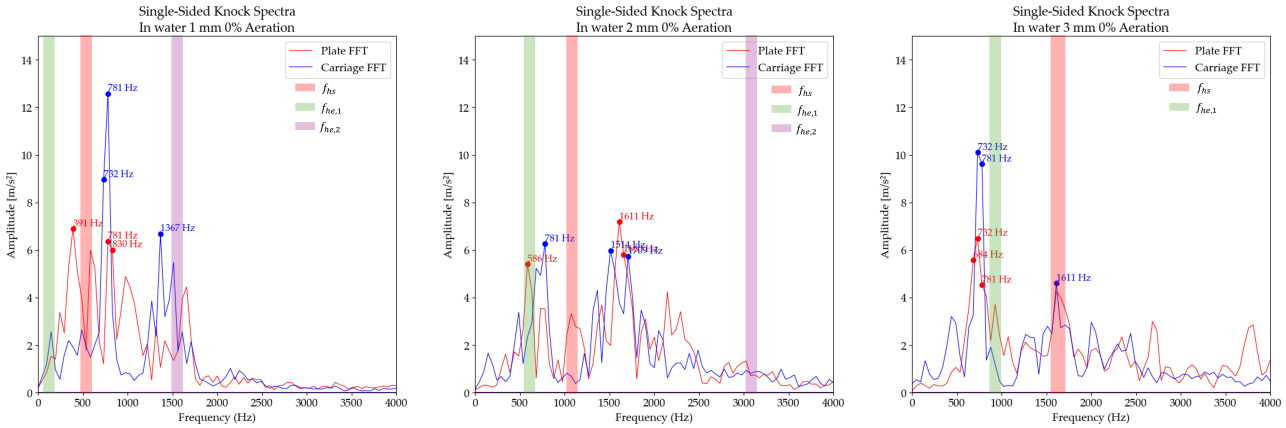

(a) $t_p = 1$ mm (b) $t_p = 2$ mm (c) $t_p = 3$ mm

Figure 36: Knock tests on the immersed wedge at $\beta_g = 0\%$

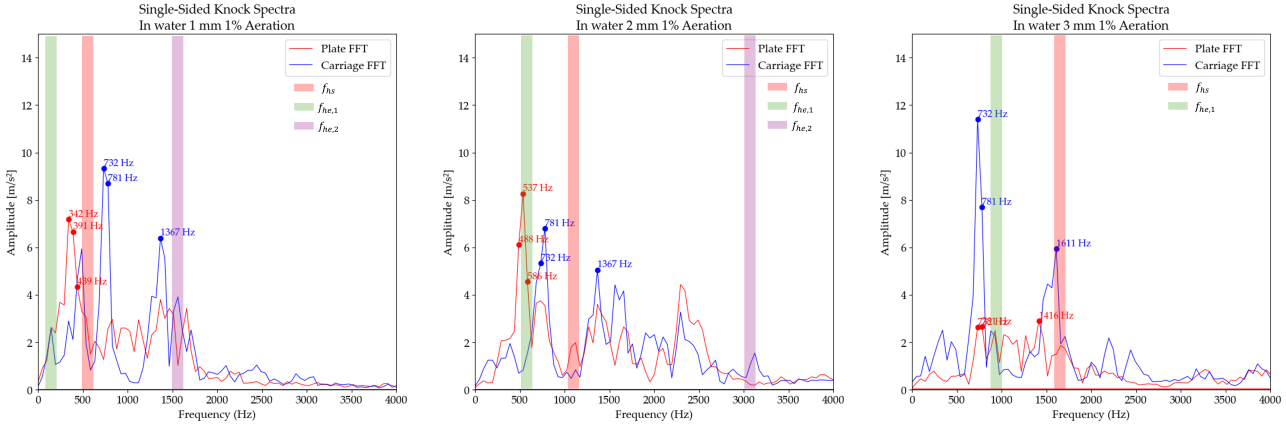

(a) $t_p = 1$ mm (b) $t_p = 2$ mm (c) $_pt = 3$ mm

Figure 37: Knock tests on the immersed wedge at $\beta_g = 1\%$

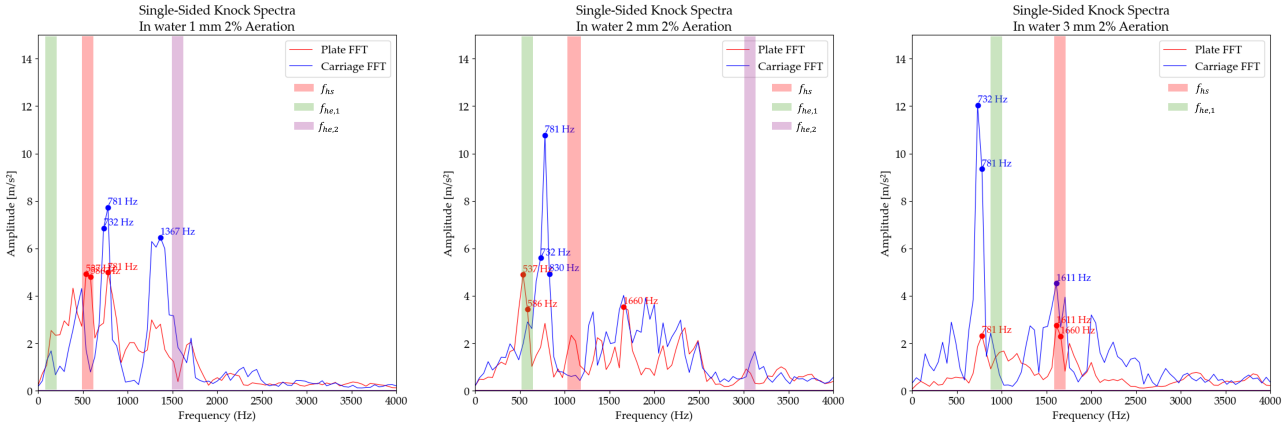

(a) $t_p = 1$ mm (b) $t_p = 2$ mm (c) $t_p = 3$ mm

Figure 38: Knock tests on the immersed wedge at $\beta_g = 2\%$

4.2 Pressure

In this section, the impact velocity, structural rigidity and aeration influence on hydrodynamic pressure are investigated. Making reference to the three stages of hydroelastic impact as classified by Ma et al. [57]:

I **Shock loading** - The first and highest pressure peak which subsequently drops very suddenly. This is often accompanied by a burst of acoustic noise.

II **Fluid expansion (low pressure)** - The compressed air layer is trapped beneath the plate expands and induces the pressure to further decrease towards a vacuum while pulling the plate further downwards.

III **Secondary re-loading** - The pressure starts to increase towards zero (atmospheric) with a second contraction of the trapped air. When the pressure recovers from sub-atmospheric to atmospheric values, the air layer does not stop contracting but is further compressed and leads to secondary re-loading of the plate.

4.2.1 Processing Workflow

The following steps were taken to process the pressure signals:

1. The data acquisition system was configured to record from 1 s prior to the trigger activation to capture a baseline for zero-offset correction. The pressure trace prior to impact was set to 0 Pa. The zero offset was observed to increase later in the campaign. This may be attributed to water ingress and environmental factors such as temperature and humidity changes. Further investigation is required to assess the impact of the pressure offset on result repeatability.

2. Pressure signal outputs were recorded in Volts (V). The calibration factors in Table 5 were used to make a conversion to pressure.

3. A fourth-order Butterworth low-pass filter was applied. A Butterworth filter is designed to pass frequencies below a cut-off frequency with minimal amplitude distortion, while sharply reducing frequencies above it. The order of the filter determines the high frequency attenuation. This filter was adopted to ensure that the pressure peaks and magnitude are retained while eliminating noise around the peak particularly in test cases for higher aeration and significant hydroelasticity.

$$H(j\omega) = \frac{1}{\sqrt{1 + \epsilon^2 \left(\frac{\omega}{\omega_c}\right)^{2n}}} \tag{25}$$

where ω is the angular frequency, ω_c is the cut-off angular frequency, n is the order of the filter, and ϵ is a parameter related to the ripple in the passband (for Butterworth filters, typically $\epsilon = 1$ for a normalized response). It should be noted that increasing the order n enhances the roll-off rate of the filter but also increases its computational complexity.

A filter at 2500 Hz was applied based on the investigation of system natural frequencies as per the hammer tests in Section 4.1. This cut-off frequency was selected such that it is higher than the first natural frequency of each plate thickness while attenuating the noise around the pressure the peaks due to the effect of aeration. Furthermore, this magnitude of filter will allow the eigenfrequencies identified during the knock tests to still be visible should excitation occur.

4. The filtered pressure traces for each pressure sensor across repeated runs were aligned at a thresh-

old during the fluid shock loading. Thresholds between 5-25 kPa along the sharp rise in pressure were chosen. The average time at which the traces for each pressure sensor cross this pressure threshold was also retained to average the tests temporally. For time domain correlation of pressure and strain, the same correction must be made for strain.

4.2.2 Pressure Peaks

Figure 39 shows the peak pressures across all tested conditions, highlighting the influence of sensor location, plate stiffness, impact velocity, aeration and local hydroelasticity. Local plate deformation alters the effective deadrise angle seen by the fluid, meaning sensors at different positions experience different apparent impact angles which evolve with plate wetting [86].

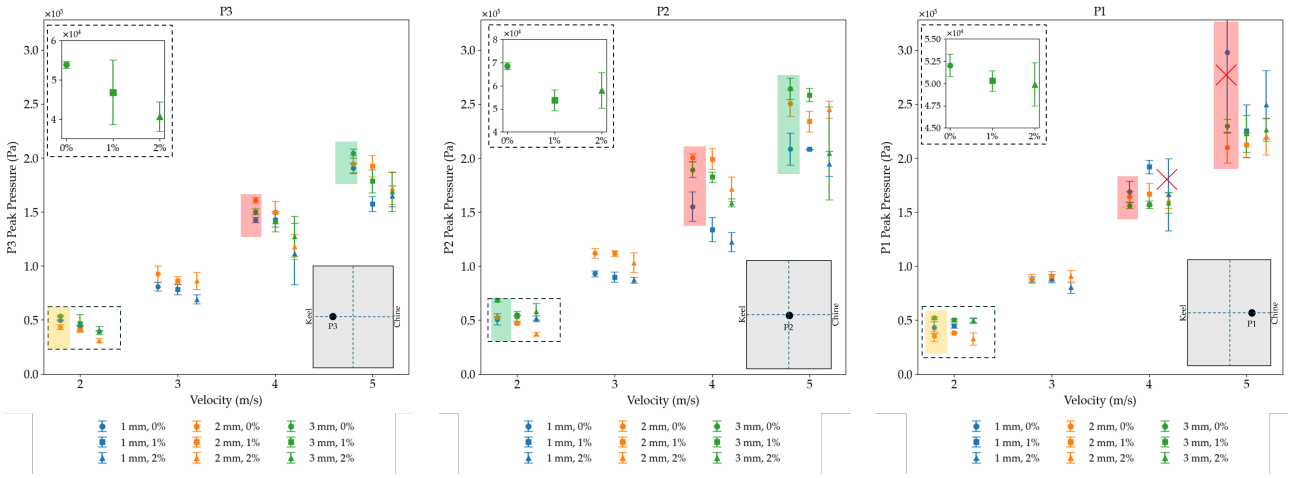

(a) P3 - close to keel. **(b)** P2 - plate centreline. **(c)** P1 - close to chine

Figure 39: Maximum impact pressures $P_{\max}$. For $\beta_g = 0\%$:
Red: $P_{\max,t_p=2\text{ mm}} > P_{\max,t_p=3\text{ mm}} > P_{\max,t_p=1\text{ mm}}$. Yellow: $P_{\max,t_p=3\text{ mm}} > P_{\max,t_p=1\text{ mm}} > P_{\max,t_p=2\text{ mm}}$.
Green: $P_{\max,t_p=3\text{ mm}} > P_{\max,t_p=2\text{ mm}} > P_{\max,t_p=1\text{ mm}}$.

Impacts in Non-Aerated Water

The experimental condition with no aeration is considered first, shown by the green, yellow and red boxes in Figure 39. Previous experimental results provide established trends between structural rigidity and impact pressure magnitude [35, 86]. For the same impact velocity, for a less stiff structure, a lower pressure peak is expected to develop as the load deforms the structure, consequently transferring the impulsive load across a longer time frame. This effect was not observed across all tested conditions of R and was more pronounced at higher velocities [35].

The discrepancies in the boxed term in Figure 39 are likely due to differences in physical loading mechanisms, particularly at higher velocity where hydroelasticity is more prevalent. Inspection of Figure 39c indicates an increase in loading near the chine for plates that are less stiff, however subject to higher uncertainty. At higher velocities, significant deformation can result in membrane effects on the plate surface. The plate fibres are loaded in tension, increasing load capacity and reducing structure response to locally amplify the pressure [89]. This nonlinearity also increases experimental variability, particularly for the thinner plate. The governing load increase mechanism is that once the deflection exceeds a certain value, the fibres in the plate are pulled in tension which has an additional load carrying effect [89]. Consequently, this limits the deformation resulting in a localised pressure increase at the corresponding sensor position.

Assessment of Hydroelastic Behaviour from Pressure Peaks

Results from Hendriksen [32] were used to benchmark the loading peaks and the hydroelastic characteristics based on the pressures. In this work, a 4 mm aluminium plate was fixed from the keel and chine to represent the clamped boundary condition, and tested at various impact velocities and deadrise angles. The pressure sensor in the central position is the same in both works, whereas the other two are offset by 10 mm. This discrepancy is approximately 1/10 of the plate length.

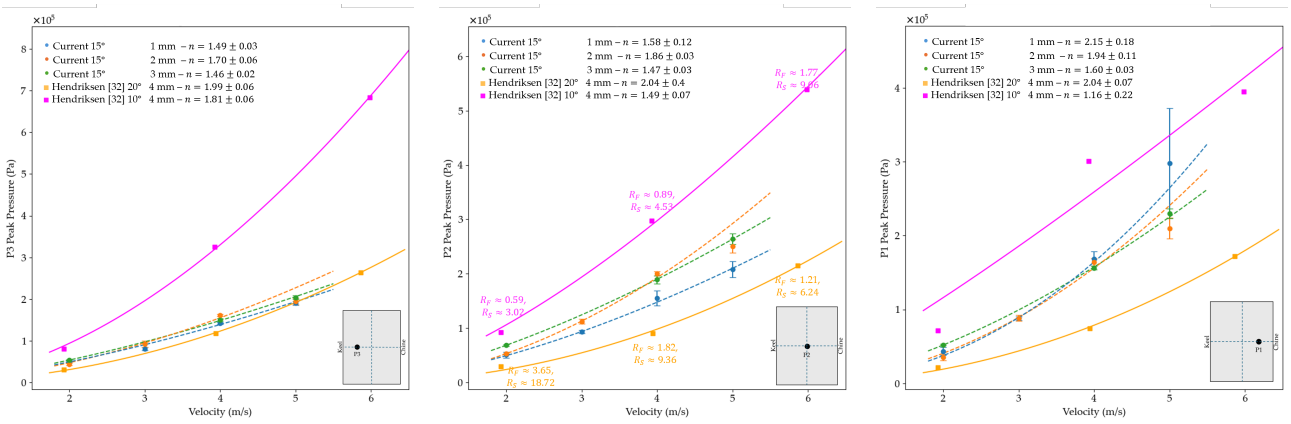

(a) P3 - close to keel. **(b)** P2 - plate centreline. **(c)** P1 - close to chine

Figure 40: Experimental results for maximum impact pressure from the current study and from [32] with fitted power law relationship.

The relationship between the pressure and the impact velocity is given by the below scaling relation. For a quasi-static case, theoretically, $n = 2$ from (16) and $n = 1$ for a hydroelastic case.

$$P = A \cdot V_i^n \tag{26}$$

A non-linear least squares relation was fitted to obtain n. For the plate at $\alpha = 20^o$ in yellow in Figure 40, the relations for all 3 pressure sensors have $n \approx 2$ in agreement with the quasi-static classification from R_S.

For the plate at $\alpha = 10^o$ (pink trace), n decreases towards the chine highlighting the hydroelastic effects as the plate is wetted during the impact. The values of R_F for the 2 mm plate in the present study, plotted in orange are in the same hydroelastic interaction regime. However, $n \to 2$ closer to the chine, contradicting then observation for $\alpha = 10^o$. The hydroelastic effects on either side of $R = 1$ in this region have different implications on the loading due to the dynamic effects and how they act during the wetting time. The fitted relation is therefore sensitive to biases regarding the data point placement around the turning point of the DAF plot. This region cannot be generalised into a single factor.

The 3 mm plate test points in Table 9 lie in the quasi-static regime for R_S with an overlap into the region of load amplification for R_F for $V_i = 4 - 5$ m/s. For the 3 mm plate, denoted by the green trace, the exponent n is consistent across P3 and P2 at 1.5, with a slight increase for the pressure sensor P1 near the chine. The interpretation is that hydroelastic behaviour is more significant closer to the keel.

The 1 mm plate test points lie between $0.23 \leq R_F \leq 0.57$, thus, with slight response amplification effect with respect to the quasi-static solution expected for $V_i = 2$ m/s. Membrane non-linear effects

are also expected. n increases substantially from keel to chine, with values for $n > 2$ in proximity to the chine. This contradicts the expectation that $n \approx 1$ for a hydro-elastic case. This data point at 5 m/s also shows substantially higher variability. Despite the hydroelastic classifications from literature, effects of flexibility are shown to be localised and dependant on the load evolution during the wetting. Ren et al. [86] refer to this phenomenon of local deformation affecting the pressure and strain development as a local deadrise angle. An exaggerated view is shown in Figure 42 for explanation purposes.

These observations suggest that existing hydroelastic classification criteria may not be generalized well beyond the specific experimental test conditions under which they were developed. This also indicates that treatment of objects as "rigid" to apply a quasi-static load is a relative term based on the geometry and impact conditions. Furthermore, assessing the effects of hydroelasticity based on the theoretical relationship with the pressure peaks is not robust due to potentially incorporating different hydroelastic effects into a single factor thus providing a misleading interpretation. The approach is dependant on the quantity and uncertainty of data points available. This vulnerability is demonstrated based on the inconsistent pressure peaks for a less stiff construction under the same impact velocity shown in Figure 40.

Aeration Effects on Quasi-Static Conditions

For the thickest plate at the lowest impact velocity ($R_S > 5$), the details are shown in the zoomed sections in Figure 39. The compressibility of aerated water will cause a smaller impact load peak over a higher load duration in comparison to an impact in incompressible water [98]. The physical relationship between load peak and temporal distribution is consistent, as confirmed by inspection of the individual tests. The mean of the pressures at the keel and chine sensors in Figures 39a and 39c demonstrate these physical effects. Despite the suggested load reduction, the high variability means the difference cannot be confirmed with confidence. For P2 in Figure 39b, $\beta_g = 1\%$ causes the highest pressure reduction. Consequently, the load peak reduction is attributed to the free surface position and conditions at impact. The uncertainties are also substantial such that overlaps between the aerated data points are present. A similar effect is observed from the experimental findings of van der Eijk and Wellens [97] for a rigid structure, where higher aeration does not always correspond to a lower pressure peak, particularly in proximity to the chine. The overlaps of the uncertainty bars with the data points are also noted.

For the thickest plate, when considering the mean load value, the aeration effects for V_i = 4 m/s near the chine are physically inconsistent as the load increases with peak aeration. Response amplification due to weakly coupled hydroelasticity is ruled out because this effect would also be observed for V_i = 5 m/s where hydroelastic effects would be more prevalent.

Possible explanations for the inconsistent results include changes in the free surface geometry and non-homogenous free surface due to aeration illustrated in Figure 41 and compliance at the pressure sensor housing and mounting. The pressure sensors are also vulnerable to the air bubble size and distribution, as shown in Figure 42. A combination of these factors will effect the free surface development, thus explaining physical inconsistencies between the sensors. Therefore, considering only the pressure loading, it is not possible to generalise the effects of an impact in aerated water for the thickest plate.

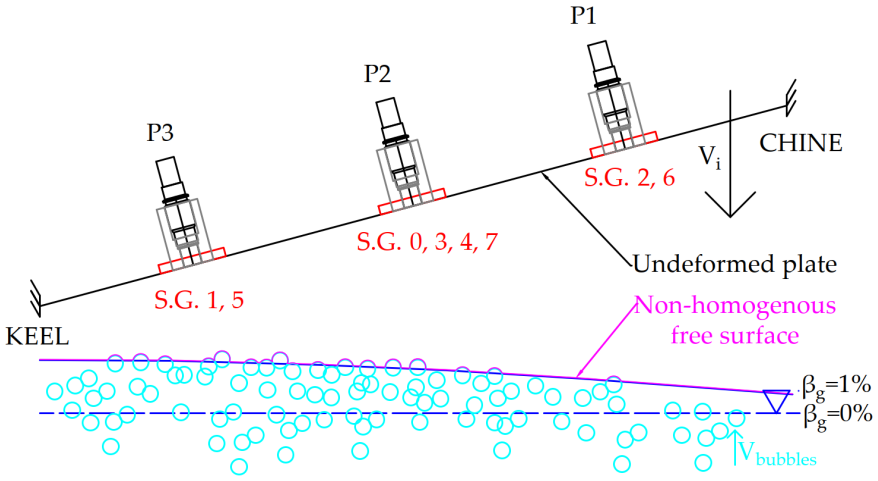

Figure 41: Detail of the curvature at the water surface in the aerated condition.

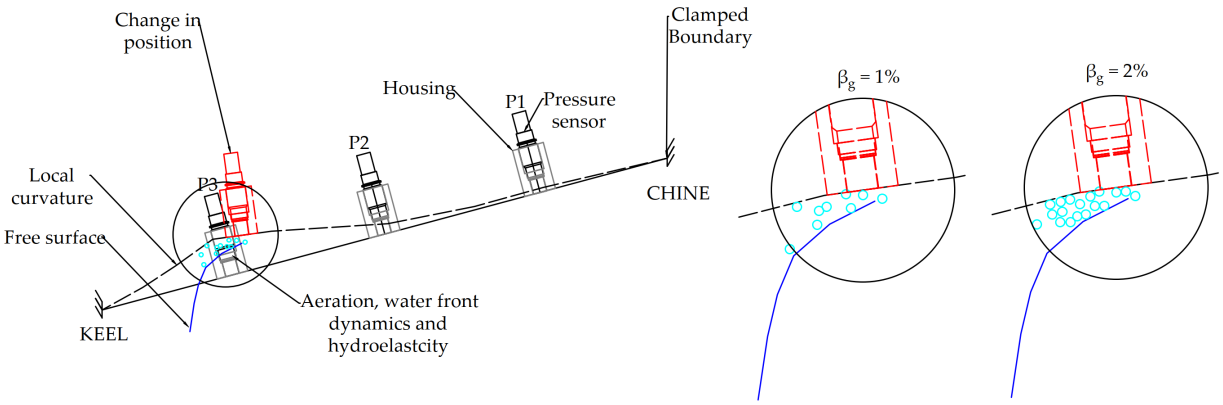

Figure 42: Detail of aeration and flexibility effects on pressure measurements.

Aeration Effects on Pressure Development near Keel

Figure 39a shows that higher aeration consistently reduced pressure near the keel across plate thicknesses and impact velocities, despite the trend overlaps within the uncertainty range. Hosseinzadeh et al. [35] state that the repeatability of the tests is better for pressure sensors near the keel. The results from this study corroborate these findings. A possible explanation is that in proximity to the keel, the free surface development has not yet been substantially affected by the free surface development, inhomogeneities in water surface and pressure sensor positional changes, shown in Figures 41 and 42. For the pressure sensors further away from the keel and at higher impact velocities on thinner plates, the results are less consistent and the uncertainties are substantially higher. Higher degrees of aeration and structural flexibility are expected to increase physical uncertainty through more complex parameter interactions. Stand-alone pressure data was insufficient to conclusively address Sub-Question 1 due to experimental uncertainty.

4.2.3 Effects of Hydroelasticity and Aeration on Pressure Development

The pressure plots for the hydroelastic condition are given in Figures 43-46. At higher aeration, the impact takes place earlier in time due to water level increase.

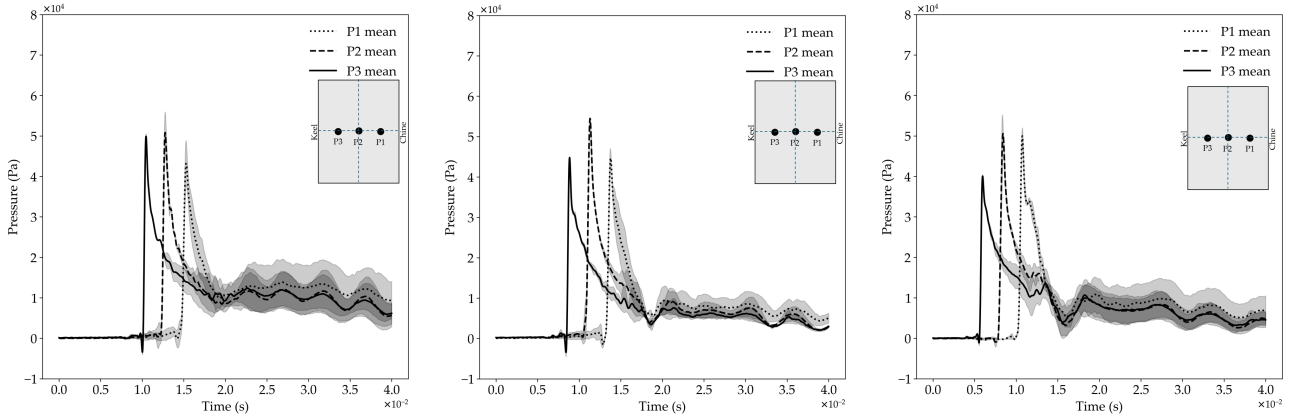

(a) $\beta_g = 0\%$ **(b)** $\beta_g = 1\%$ **(c)** $\beta_g = 2\%$

Figure 43: Pressure–time traces for the 1 mm plate at V_i = 2 m/s ($R_F = 0.58, R_S = 3.0$).

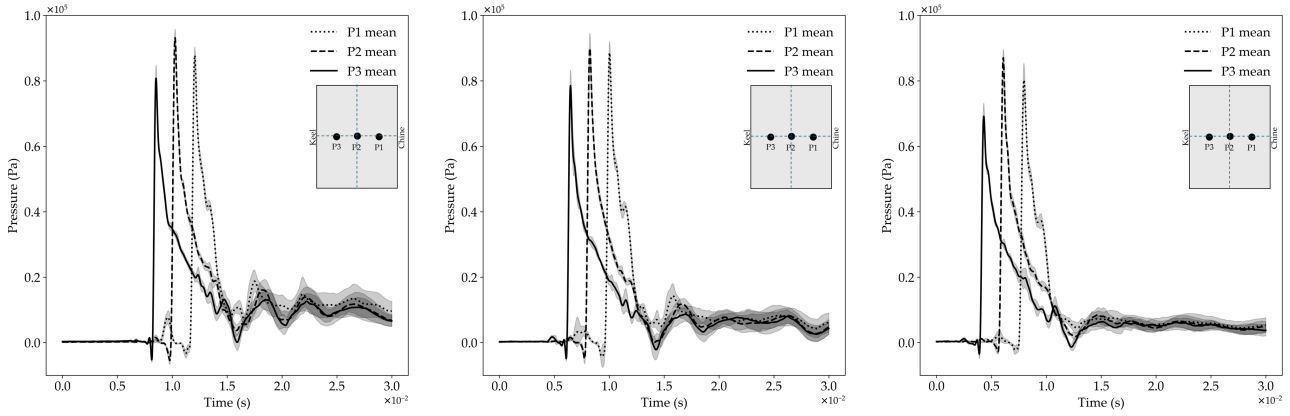

(a) $\beta_g = 0\%$ **(b)** $\beta_g = 1\%$ **(c)** $\beta_g = 2\%$

Figure 44: Pressure–time traces for the 1 mm plate at V_i = 3 m/s ($R_F = 0.39, R_S = 2.0$).

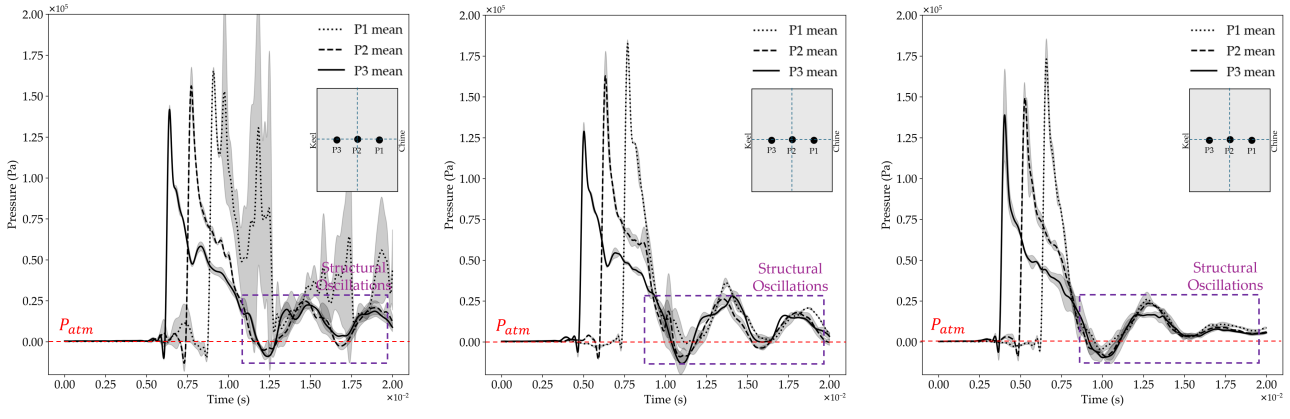

(a) $\beta_g = 0\%$ **(b)** $\beta_g = 1\%$ **(c)** $\beta_g = 2\%$

Figure 45: Pressure–time traces for the 1 mm plate at V_i = 4 m/s ($R_F = 0.29, R_S = 1.50$).

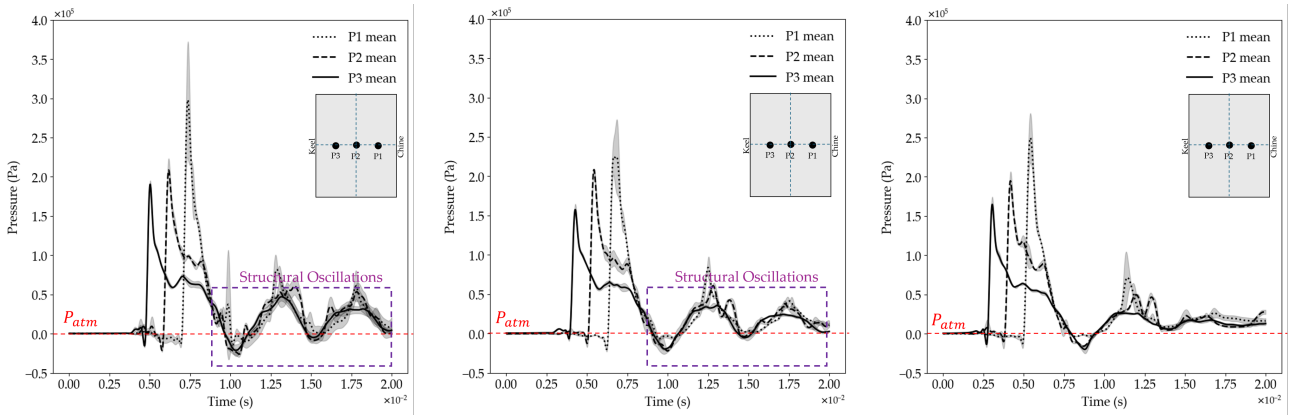

(a) $\beta_g = 0\%$ **(b)** $\beta_g = 1\%$ **(c)** $\beta_g = 2\%$

Figure 46: Pressure–time traces for the 1 mm plate at V_i = 5 m/s ($R_F = 0.23, R_S = 1.20$).

Figure 46 demonstrates the condition with strongest hydroelastic effects. A reduction was noted for all three sensors in this loading condition with the addition of aeration. For P1 and P3 the plot for $\beta_g = 1\%$ shows the highest reduction in pressure peak. For P2, $\beta_g = 2\%$ shows the highest reduction in pressure peak. The pressure peak is directly correlated to the temporal load distribution due to aeration effects, but is highly effected by local impact conditions. Even at strongly hydroelastic conditions, a consistent trend in pressure reduction due to aeration could not be established due to the experimental limitations.

Pressure oscillations after the fluid shock loading peak has occurred were also observed for this loading condition. The post-impact pressure oscillations were isolated and a FFT was applied to identify density waves (Table 2) in an attempt to capture aeration effects on the surrounding fluid domain. The oscillations occur at the wetted plate natural frequency of approximately 200 Hz, and are also captured by the accelerometer on the plate and by the strain gauges as shown in Figures 50 and 51. For $\beta_g = 0\%$ the water is nearly incompressible, resulting in less damping for the post-impact oscillations. For a higher value of aeration, the damping effect of aeration is stronger, where for $\beta_g = 2\%$, the oscillations are damped earlier in time. The oscillatory effects are due to the pressure sensors being embedded directly in the plate which is vibrating and decelerating in the water. The three stages of the impact described by Ma et al. [57] are not visible as the pressure drop never reaches 2.3 kPa [44], and consequently, no subsequent re-loading takes place. The cavitation effects observed by Mai et al. [58] were due to a completely flat and rigid plate impacting the water at high speed.

To locate the density waves, the approach taken by van der Eijk and Wellens [98] was adopted. They assume the pressure waves will either reflect off the bottom or side of the domain box. A characteristic distance L_d of 0.5 m between the point of impact and the bottom of the domain box was taken for a 2D condition. The approach was applied to the case of a rigid structure at V_i = 7 m/s. The same methodology was applied to the pressure signals shown in Appendix 4 for the 3 mm plates at $V_i = 4 - 5$ m/s. The pressure waves were not captured. This may be due to the lower impact velocity of 5 m/s and structure flexibility such that pressure wave signal is not strong enough for propagation and detection by the pressure sensors. The pressure sensors are translating downwards and undergoing oscillations with the plate. The approach was also applied to the pressure traces in Figure 46. Here, the structural response was found to be dominant and density waves were also not detected. Furthermore, the impact transferred to the structure for the post-impact structural oscillations results in less energy being available for a density wave to propagate through the domain box. Despite the assumption that pressure waves will either reflect off the bottom or side of the domain box in the 2D case, the pressure waves will propagate in all directions. Given the ratio of

half-tank length to water height to width ratio is approximately 3:3:1, the reflection will not occur in all directions at the same frequency as per $f_c = c_f / (2 \cdot L_d)$. Therefore, the pressure sensors mounted directly onto the flexible plate exhibit limitations with measuring pressure waves as an indication of aeration effects. Density wave frequency is also highly sensitive to the aeration percentage and bubble distribution. Alternative techniques and pressure sensor mounting directly to the domain box are proposed in Section 5.2.

Comparison to Numerical Results

The numerical results of Aghaei [4] show that the aeration effect is dominant at $\beta_g > 5\%$, such that peak pressures become independent of the hydroelasticity beyond this point, thus eliminating the need for strong coupling. The present study could not verify this hypothesis as the aeration flow controller was operating at the limit. Furthermore, a power law relationship for the maximum numerical pressure scaling with velocity was defined to account for the water compressibility. The present author finds this approach too generic due to combining the physics of different hydroelastic interaction regimes. Section 4.2.2 for the non-aerated impact condition demonstrates the lack of robustness of this approach. Furthermore, non-linear effects will be present, which a non-validated numerical model will omit.

In summary, pressure analysis yielded inconclusive results for quantifying the aeration and hydroelasticity effects on structural loading during slamming. The physical mechanisms for hydroelasticity and aerated load reduction were identified, but pressure measurements lacked statistical significance and failed to detect the density waves generated on impact.

4.3 Strain

4.3.1 Processing of Strain Data

The operational principle behind strain gauges is that as the object is deformed, the foil is deformed, causing its electrical resistance R_Ω to change by ΔR_Ω. The output of the strain gauges is in the form of mVolts/V. The gauge factor GF is defined as the ratio of fractional change in electrical resistance to the fractional change in length (strain) [65], given as below for the measured strain ε_m:

$$\mathrm{GF} = \frac{\Delta R_\Omega / R_\Omega}{\varepsilon} \tag{27}$$

A value of 2.12 $\pm$1% [53] was provided from the manufacturer and is typical for strain gauges rated for steel. To compute the strain for a quarter bridge:

$$\varepsilon_m = \frac{4 \cdot \frac{V_{out}}{V_{in}}}{GF} \tag{28}$$

Where V_{in} is the excitation voltage across the bridge and V_{out} is the output voltage of the bridge. However, to account for the non-linearity [65]:

$$\frac{V_o}{V_{in}} = \frac{GF \cdot \varepsilon_m}{4} \cdot \left(\frac{1}{1 + GF \cdot \frac{\varepsilon_m}{2}} \right) \rightarrow \varepsilon = \frac{4 \frac{V_o}{V_{in}}}{\mathrm{GF}\left(1 - 2 \frac{V_o}{V_{in}}\right)} \tag{29}$$

The complete correction for strain gauges ε_c is given as below [37]:

$$\varepsilon_c = \varepsilon_m - \varepsilon_s - \varepsilon_f + \text{Influence of Leads} \tag{30}$$

where ε_m is the strain signal without any temperature correction, ε_s is the influence of the thermal output polynomial and ε_f is the influence deviating temperature coefficient of the substrate material, which is 0 in this case. Additionally, the GF was adjusted based on the temperature coefficient α_{GF}, given as 0.008 $\%/^o c$

$$\mathrm{GF}_T = \mathrm{GF} \cdot (1 + \alpha_{\mathrm{GF}} \cdot \Delta T) \tag{31}$$

The maximum temperature difference ΔT between the air and the water was found at $4^o C$ with air temperature being between 22-24$^o C$ The highest effects of thermal shock are expected during the initial impacts for thinner plates. Therefore, additional correction of the strain value using the thermal polynomial was not found to add value [64]. Furthermore, a two-wire circuit was used, which has inherent cable resistance that was also not quantified. This can be remedied using a three-wire circuit [37]. In comparison to the uncertainty due to the repeatability, these uncertainties have been assumed negligible. However, further investigation into the thermal effects of impact, particularly for the thinner plate, where the thermal mass is more sensitive, require additional consideration in future research. ε_{exp} will be used to denote the final corrected value of the strain as obtained experimentally.

4.3.2 Strain Results

The strain peaks recorded from each strain gauge are investigated first, as presented in Figure 47. Across all tests, the peak strains from gauges 0-3 are consistently higher than the symmetric counterpart from gauges 4-7. For the 1 mm plate, strain gauges were damaged due to water ingress and the data points have been crossed out. Inconsistent clamping along the plate's width and bolt loosening after several impacts were ruled out due to a systematic inspection prior to each test. The observed asymmetry is likely due to a slight aft-biased impact, potentially caused by carriage manufacturing tolerances and misalignment of the guiding tower. The discrepancy between the fore and aft strain gauges becomes more appreciable for thinner plates at higher velocities due to higher expected deformation of the plates. The load reduction influence of the domain box was observed to be more significant toward the fore and aft regions of the plate, particularly for thinner structures, due to the effect of the pressure condition at the fore and aft tank boundaries.

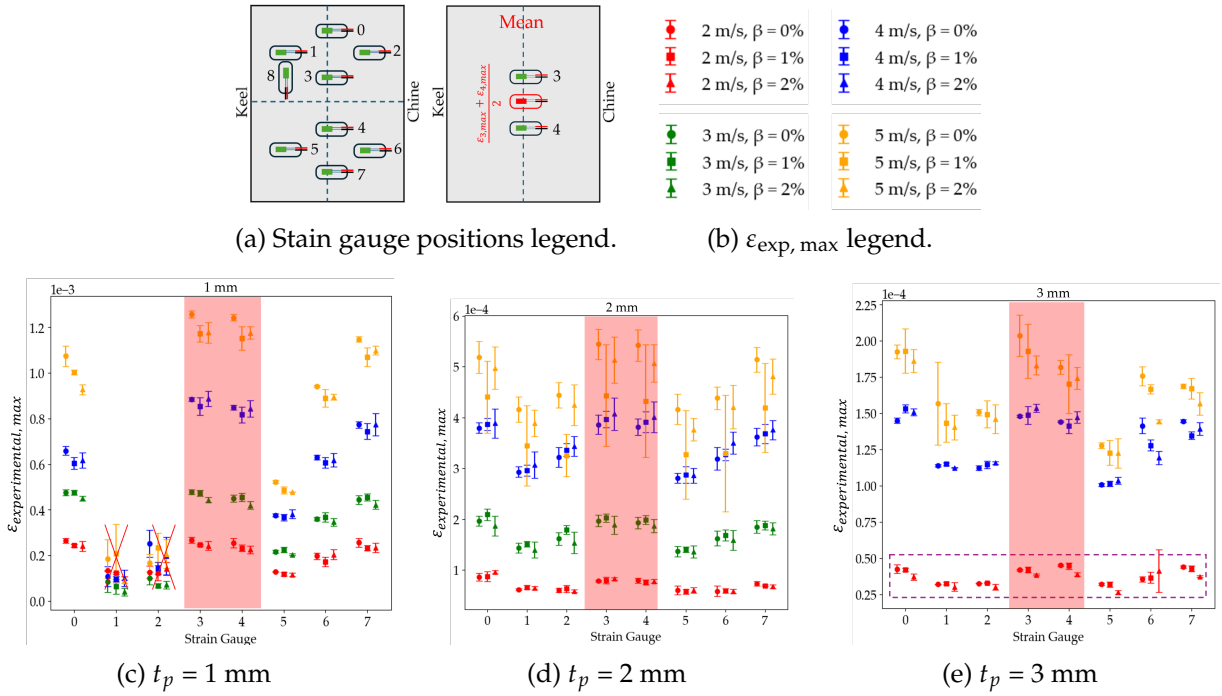

(a) Stain gauge positions legend. (b) $\varepsilon_{\text{exp, max}}$ legend.

(c) t_p = 1 mm (d) t_p = 2 mm (e) t_p = 3 mm

Figure 47: Peak strain responses across different impact conditions, with associated legends for sensor positions and bridge mapping.

Effects of Aeration on a Structure under Quasi-Static Loading

Considering the strain peaks for the case of the stiffest plate at the lowest impact velocity, in the purple box in Figure 47e, shown in detail in Figure 48a. From Table 9, $R_F = 3.05$ and $R_S = 15.6$, indicating that a quasi-static condition should be fulfilled. For gauge 6, the unusually high variance indicates the possibility of damage, water ingress or improper adhesion, consequently discarding the validity of this strain gauge. Consistent reduction in strain between $\beta_g = 0\%$ and $\beta_g = 2\%$ is observed, with the exception of strain gauge 1. Higher aeration causes impact force distribution over a longer duration [98], thereby reducing peak loading. The peak strains for $\beta_g = 1\%$ are less consistent. Since the $t_w >> T_w$ in this loading condition, a strain response amplification effect is not physically possible. Furthermore, the uncertainty bars are not consistent throughout the surface of the plate with some overlaps, thus limiting the conclusions on the quasi-static effects. The variability may stem from local water surface inhomogeneities and higher uncertainty in the water level due to low pressure through the aeration diffusers. Since the bubble dimensions are estimated to be on the

same scale as the plate thickness range, the spatial and temporal distribution of bubbles on the water surface and in the region of impact is expected to influence the results. The effect of water surface inhomogeneity could not be quantified.

For the stiffest plate, the impact conditions at $V_i = 4$ and 5 m/s, corresponding to the blue and yellow data points in Figure 47e, the trends in strain with respect to the non-aerated case are inconsistent and highly asymmetric throughout the length and width of the plate, particularity for the 4 m/s impact case. Hydroelastic effects could possibly be present due to the overlap into the pink region for R_F, however, inconsistencies with the impact region will also effect this strain peak.

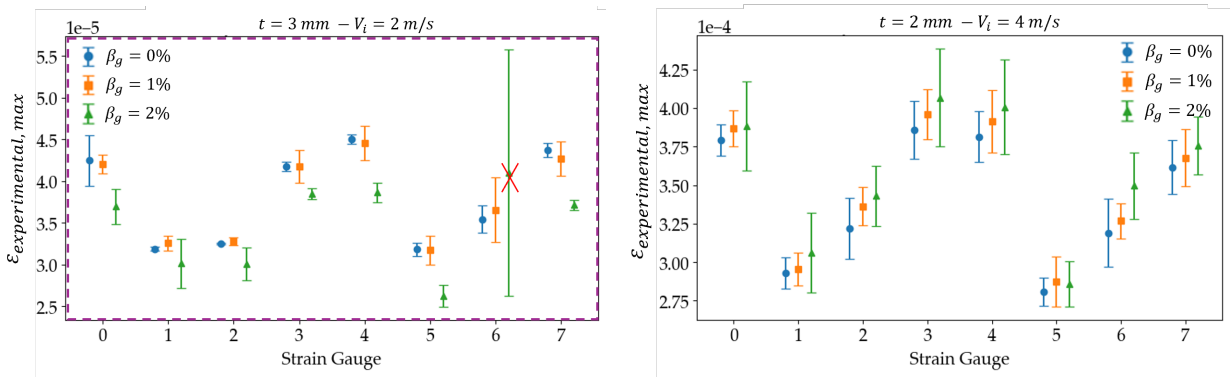

(a) Quasi-static condition.

(b) Resonant condition.

Figure 48: Strain distribution details.

Response Increase due to Aeration

As expected, for the cases with no aeration, indicated by the circular symbols in Figure 47, the strain is higher for a higher impact velocity for the same plate thickness. This trend is observed throughout all experimental conditions, and aligns with the findings of Ren et al. [86] and Hosseinzadeh et al. [35] due to higher load.

The combined physical effects of hydroelasticity and aeration and is the novelty addressed in this work, and consequently no direct benchmark for the expected physical effects exists in literature. For the 2 mm plate at $V_i = 4$ m/s and $R_F = 0.83$, strain increases of 2.76% and 5.25% are reported for $\beta_g = 1\%$ and 2% respectively, shown in Figure 48b. This counteracts the expected load reduction effects when slamming into aerated water, and must be investigated in the context of the hydroelastic response amplification. The aerated water will (1) cause an increase in the wetting time due to load redistribution by aeration (2) result in a fluid density reduction altering the first wetted natural period of the structure, such that an increase in R_F is predicted. For this condition, the wetting time was estimated using the wedge position and dimensions from the frontal facing Basler camera [3] for the initial wedge position and integrating the accelerometer traces to estimate the time of keel contact with the water and time of complete chine wetting. T_w was also estimated based on β_g. An approximate 23% increase in wetting time is noted. The change in density in the denominator only contributes to a 1% increase in the value of R. The combined effect results in $R_F \rightarrow 1$, thus aligning with the peak response increase at the resonance condition for hydroelastic interaction. Note that these effects have not been directly incorporated into R in the figure to maintain consistency with the original representation. The error bars overlap across the aeration cases, and therefore the percentage strain increase cannot be considered statistically significant. The trend is however consistent across all the gauges on the plate for this loading condition. Further investigation with precise parameter control is required to confirm this hypothesis and to quantify the response increase due to aeration.

Plate Flexibility and Hydroelastic Interaction

For the 1 mm plate at $V_i = 4 - 5$ m/s where hydroelastic effects are active as per both R_F and R_S, the strain peaks are shown in Figure 49. In this condition, a reduction in strain peak is observed for $V_i = 2, 3, 5$ m/s for gauges 3 and 4 without overlaps in the uncertainty bars. For a comparison to T_w, the average of gauges 3 and 4 in the central position was taken, as shown in Figure 47a. The results are presented in Table 11.

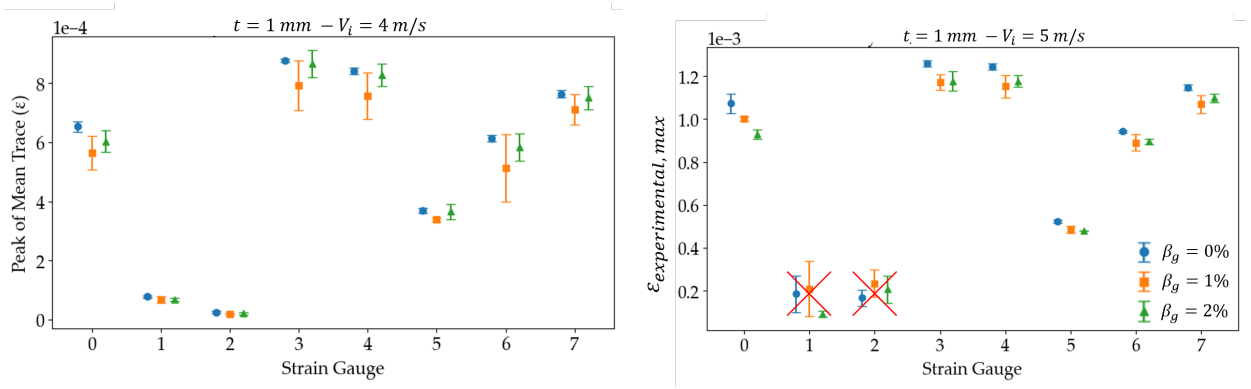

(a) t_p = 1 mm and V_i = m/s.

(b) t_p = 1 mm and V_i = 5 m/s.

Figure 49: Strain distribution details for hydroelastic impact conditions.

Table 11: Maximum strain as the mean of strain gauges 3 and 4, measurement uncertainty, and percentage reduction with respect to the non-aerated case for all the test conditions at t_p=1 mm.

V_i (m/s)	β_g (%)	$\overline{\varepsilon_{max}}$ (m/m)	σ ($\pm m/m$)	σ ($\pm$%)	% Reduction
2	0	2.53×10^{-4}	1.28×10^{-5}	5	–
	1	1.91×10^{-4}	8.35×10^{-5}	44	25
	2	2.10×10^{-4}	4.83×10^{-5}	23	17
3	0	4.60×10^{-4}	1.30×10^{-5}	3	–
	1	4.42×10^{-4}	2.87×10^{-5}	6	4
	2	3.91×10^{-4}	5.89×10^{-5}	15	15
4	0	8.60×10^{-4}	7.77×10^{-6}	1	–
	1	7.76×10^{-4}	9.26×10^{-5}	12	18
	2	8.47×10^{-4}	4.55×10^{-5}	5	3
5	0	1.24×10^{-3}	2.49×10^{-5}	2	–
	1	1.15×10^{-3}	5.20×10^{-5}	5	7
	2	1.16×10^{-3}	5.09×10^{-5}	4	6

In Figures 50 and 51, the strain traces for V_i = 4 and 5 m/s are aligned at the peak to investigate the strain response evolution over time. Since $t_w << T_w$, the whole plate is wetted before structural oscillations develop. Consequently, the impulse is transferred to the plate and post impact oscillations are observed at the higher velocities in Figures 50 and 51. A direct correlation was found between the strain peak and evolution over time. For gauge 3, Figures 50b and 50c demonstrate the widest band and the lowest strain peak for $\beta_g = 1\%$ (red trace). The same effect is observed in Figures 50e and 50f for gauge 4. For the $V_i = 5$ m/s condition in Figure 51, the lowest strain peak for $\beta_g = 2\%$ is also

corroborated by the widest load evolution envelope, shown by the green trace in Figures 51b and 51c for gauge 3 and 51e and 51f for gauge 4. Note that the uncertainty bands around the mean of the runs are due to both the strain magnitude uncertainty and due to the impact occurrence in time, and have been included for completion. The observations were also confirmed for the individual runs. For both cases, these effects are also reflected in the damping of post-impact oscillations, which take place at the natural frequency of the wetted plate when the impulse has been completely transferred to the structure.

Consequently, for a loading condition where hydroelastic coupling is important such $t_w << T_w$ and $R_F << 1$, a reduction in peak strain was found. However, from Figure 12, the data points for the non-aerated water for the 1 mm plate also do not follow the trend of lower DAF for a lower value of R_F, and a benchmark to pure hydroelastic effects could not be established. Furthermore, the overlaps due to the variance require further test repetitions and more carefully controlled experimental conditions for statistically significant values.

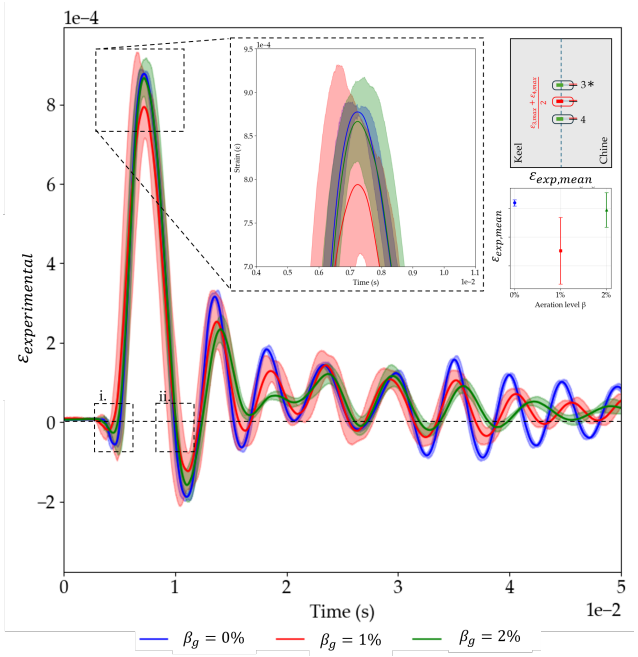

(a) Gauge 3.

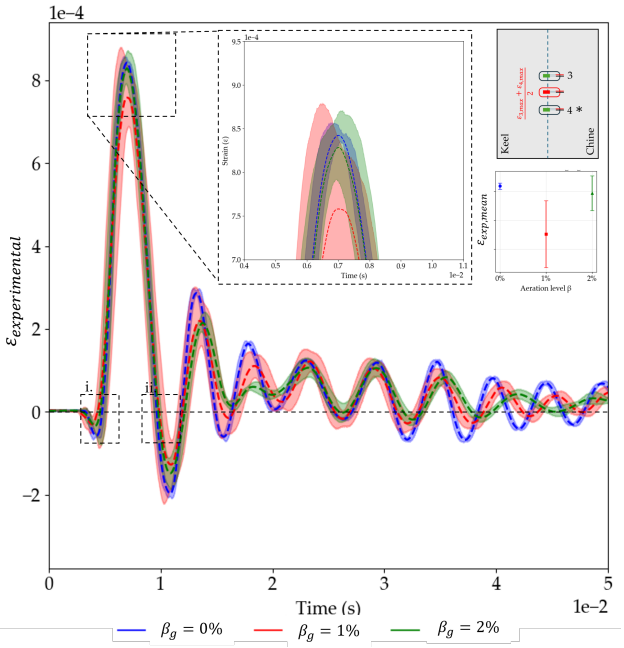

(d) Gauge 4.

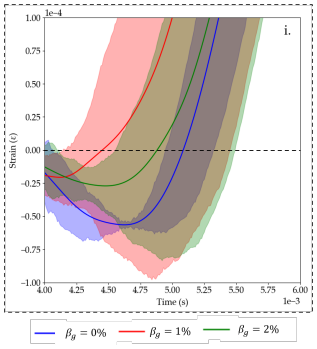

(b) Gauge 3 left.

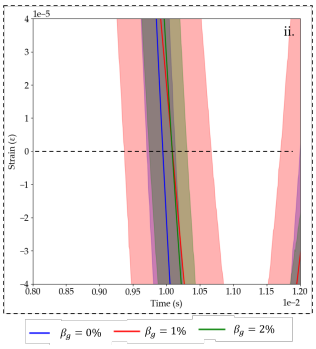

(c) Gauge 3 right.

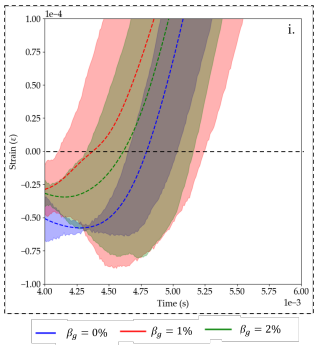

(e) Gauge 4 left.

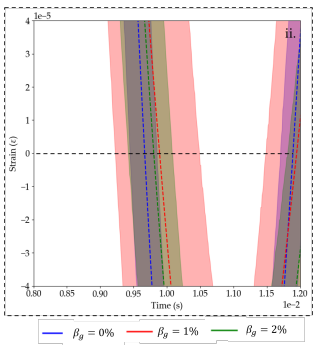

(f) Gauge 4 right.

Figure 50: Strain results for the 1 mm plate at $V_i = 4$ m/s.
Top: Gauge 3 and Gauge 4 stress peak at plate centre. Bottom: zero-strain crossing.

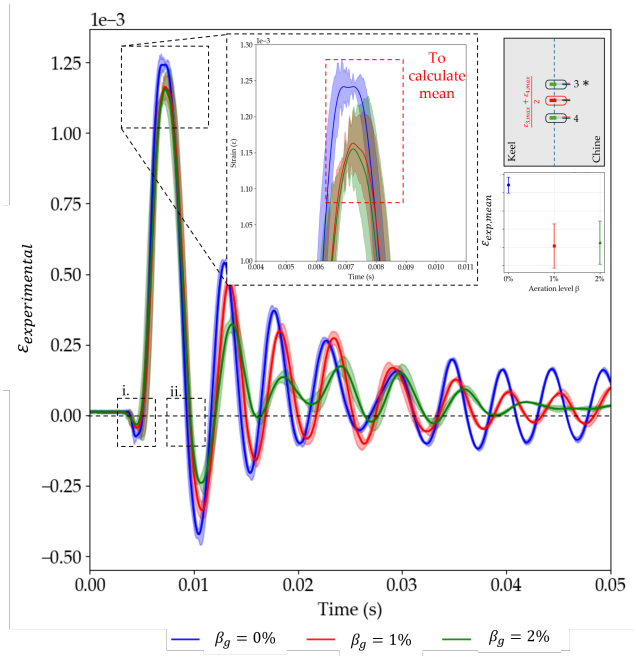

(a) Gauge 3.

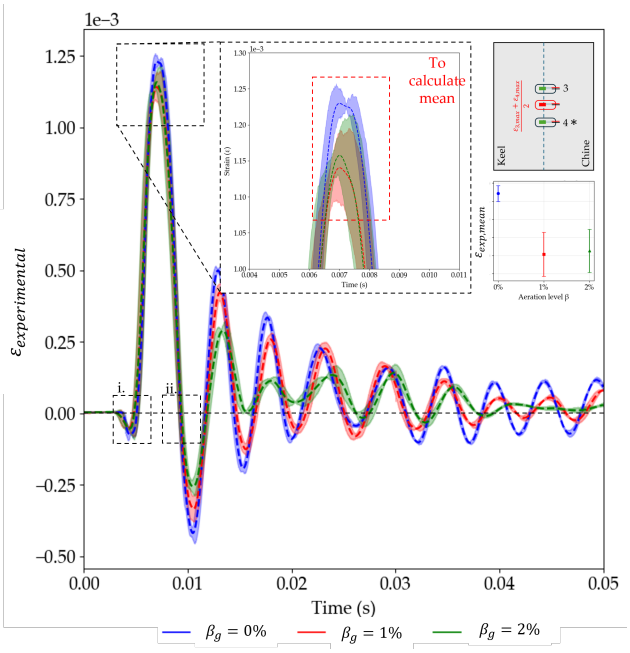

(d) Gauge 4.

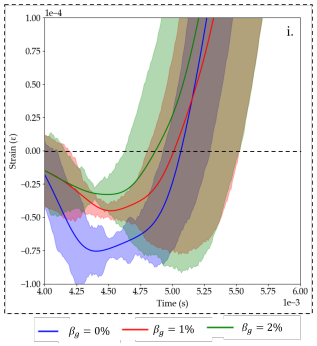

(b) Gauge 3 left.

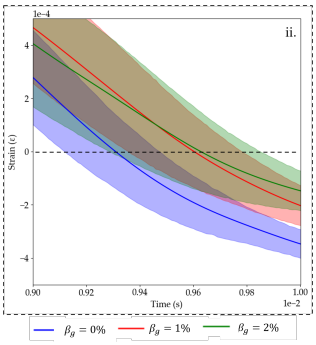

(c) Gauge 3 right.

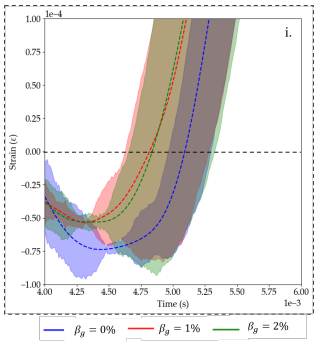

(e) Gauge 4 left.

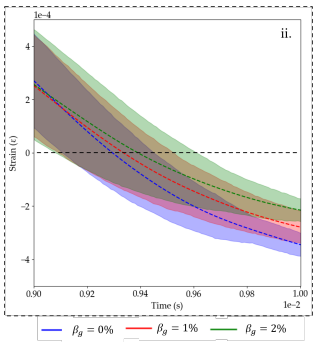

(f) Gauge 4 right.

Figure 51: Strain results for the 1 mm plate at $V_i = 5$ m/s.
Top: Gauge 3 and Gauge 4 stress peak at plate centre. Bottom: zero-strain crossing.

4.4 Optical Measurements - 3D-DIC

The out-of-plane plate deformation in the local coordinate system , $w(x', y', t)$, is obtained by combining (i) rigid-body kinematics from the accelerometer/light gate and (ii) conditioned Digital Image Correlation (DIC) fields. A detailed explanation is provided in Appendix 3.4-3.5. Figure 52 shows the global coordinate system to the rigid carriage displacement, and the local coordinate system with respect to the wedge deadrise angle.

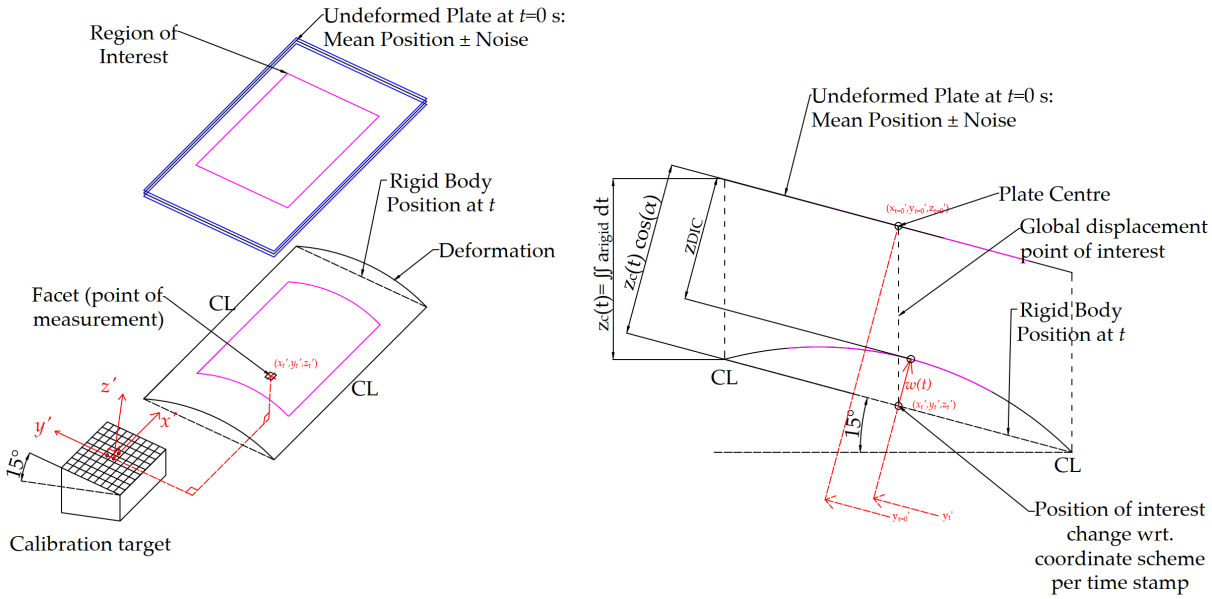

Figure 52: Schematic of calculation methodology for local plate deformation from the 3D-DIC setup.

The results for deformation at plate centre at $t_p = 1$ mm and $V_i = 5$ m/s are shown in Figure 53. As the wedge descends, additional shadows increase image noise. The deformation peaks beyond the initial first peak are not captured by DIC with the same consistency as the strain gauges. The load increase is not physical, particularly for cases with aeration due to the load attenuation effect. For the cases with impact in aerated water, signal variability between subsequent runs was detected characteristic of the free surface conditions on impact. Despite the reduction in plate deformation, a correlation between deformation and aeration in the water cannot be made from these measurements alone. Consequently, the resolution of this approach is not sufficient to determine the effects of aeration on the deformation and the load reduction. Test cases with sufficient signal to noise ratio are shown in Table 12.

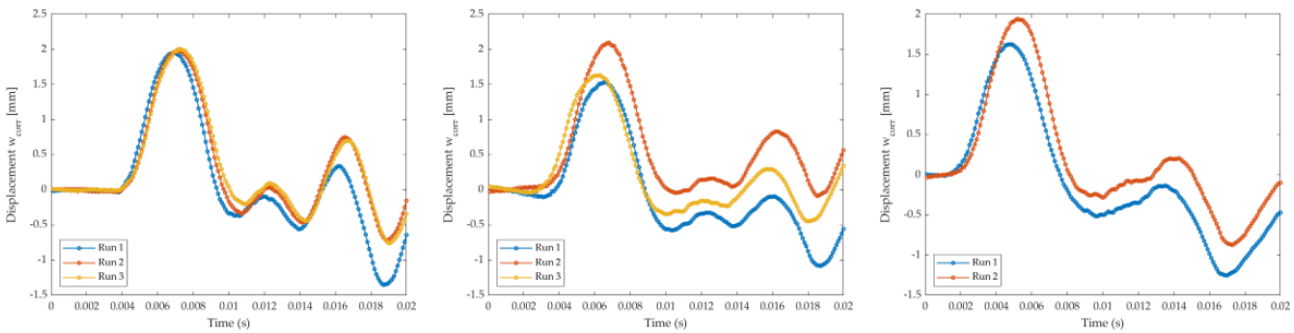

(a) $\beta_g = 0\%$ **(b)** $\beta_g = 1\%$ **(c)** $\beta_g = 2\%$

Figure 53: Deformation at plate centre (P2 position) as measured with the 3D-DIC.

Table 12: Peak corrected displacement w_{max} and DAF for each condition.

t_p (mm)	V_i (m/s)	β_g (%)	w_{max} (mm)	DAF (w_{max})	DAF (ε_{max})
1	5	0	1.985	0.636	0.496
1	5	1	1.756	0.563	0.462
1	5	2	1.784	0.572	0.464
1	4	0	1.292	0.646	0.539
1	4	1	1.420	0.710	0.486
1	4	2	1.394	0.697	0.531
1	2	0	0.304	0.607	0.635
1	2	1	0.409	0.819	0.478
1	2	2	0.446	0.893	0.527
2	5	0	1.023	2.622	0.871
2	5	1	0.933	2.393	0.702
2	5	2	0.813	2.085	0.818

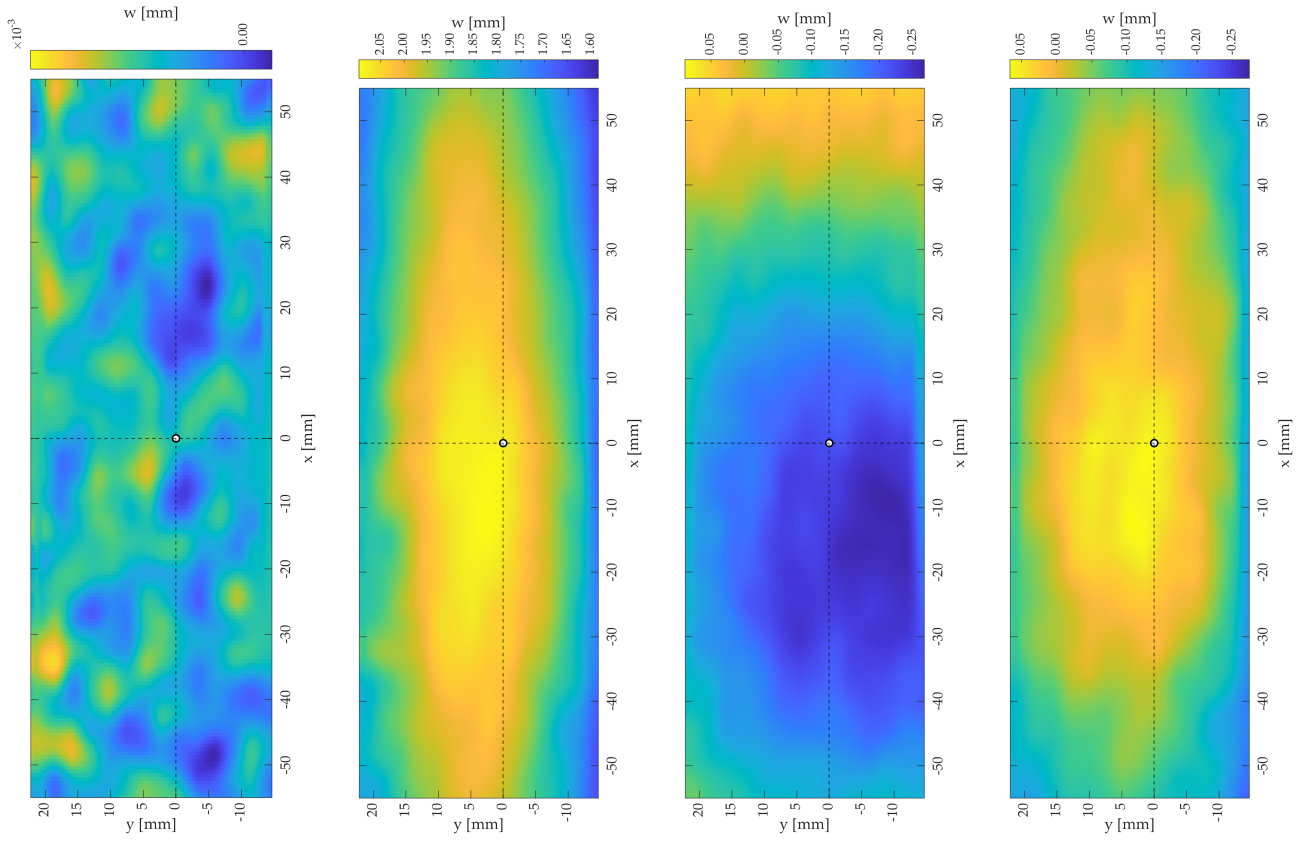

(a) t = 2 ms. (b) t = 71 ms. (c) t = 108 ms. (d) t = 120 ms.

Figure 54: DIC snapshots for the impact case at t_p= 1 mm V_i= 5 m/s.

Figure 54 maps the out-of-plane displacement field w in the vicinity of the central pressure sensor (P2). The position of the pressure sensor is slightly offset due to the available viewing window. The pre-impact frame (Figure 54a) is dominated by measurement noise despite post-processing, with no coherent deformation pattern evident. At t=71 ms (Figure 54b), the field exhibits a clear local maximum near P2, consistent with the expected deformation peak. The displacement peak is temporally coincident with the peak pressure recorded by sensor P1, despite a spatial and temporal offset of the strain peak due to hydroelastic effects with the plate acting as a filter. Subsequent frames capture alternating maxima and minima characteristic of the post-impact response, although the noise threshold is eventually exceeded.

Limitations

At the impact conditions not shown in Table 12, the DIC signal-to-noise ratio was too low to produce reliable results. This effect is already observed for the 2 mm plate at the highest impact velocity where a non-physical load amplification effect is captured. In all cases, the strain could not be retrieved directly from the Istra 4D software [16]. The displacement was also differentiated twice, however, this approach resulted in noise amplification while attenuating the relevant gradients. Strain results were 500 % higher than measurements from the strain gauges and exhibited high fluctuations instead of a smooth load ramp towards the peak. These values are not physically viable as plastic deformation would have occurred, and such a load amplification is beyond the effect of hydroelasticity even near the resonance condition.

The displacement fields are useful to cross-check the relevance of hydroelasticity by comparing the measured response with the quasi-static case, and to visualise the development of deformation along the plate with direct correlation to the pressure and strain development. The results for strain are expected to be more representative due to direct strain-gauge contact with the plate and higher proven repeatability, particularly given the experimental sensitivity to impact conditions.

4.5 Answers to Research Questions

4.5.1 Summary of Results per Interaction Regime

This section analyses the experimental results across all tested hydroelasticity and aeration conditions. To address both research sub-questions, the hydroelastic effects have been classified using the hydroelasticity factor R on the horizontal axis of Figure 47. This is plotted against the Dynamic Amplification Factor (DAF), defined as the ratio of the experimental strain ε_{exp} and the quasi-static structure response ε_{anal} [61], is plotted on the vertical axis. The Wagner [103] formulation for plate wetting (6) was used in the calculation R_F and in the denominator of the DAF for consistency. For a comparison to the quasi-static theory, the mean of strain gauges 3 and 4 in the central positions was taken averaged as per Figure 47a to obtain a value for the strain at the centre of the plate while compensating for asymmetric effects. For each group of tests represented by the points in Figure 47, the average impact velocity from the light gate was computed as per 3.7.3 for the values of R_F and R_S. The experimental results have been classified by percentage of aeration. Each dashed box in Figure 55 corresponds to one plate thickness. The box position along the horizontal axis reflects the plates' natural period, the horizontal spread of points within a box captures the impact velocity effect and the vertical spread inside a box around a value of R captures the aeration effects. For the non-aerated condition, expected hydroelastic phenomena are not observed e.g. convergence to a single value of DAF, peak load at approximately $R_F \approx 1$ and lower DAF with lower R, due to high experimental sensitivity at small scale.

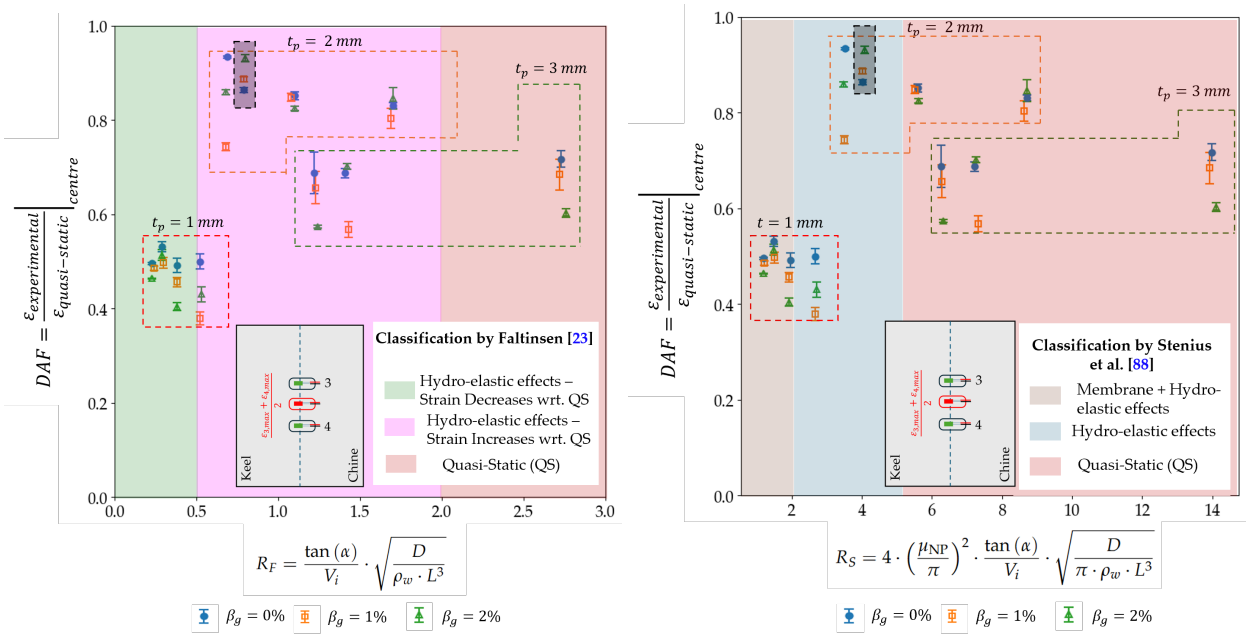

(a) R_F. Regime classification by [35].

(b) R_S. Regime classification by [88, 89].

Figure 55: Experimental strain peaks in terms of the DAF and R for applied design conditions.

Quasi-Static Condition: $R_F \geq 2$ & $R_S \geq 5$

$R_S > 5$ marked in red in Figure 55b, captures all the experimental conditions tested for the stiffest plate. The findings in the present study do not align with this classification as DAF<1 as the quasi-static solution consistently over-predicts the peak strain for both the aerated and non-aerated cases for the 3 mm plate. Strains between 0.25 - 4×10^{-4} were measured for the 3 mm plate at $\beta_g = 0\%$, indicating that some deformation occurs, and thus hydroelastic effects were involved and the plate cannot be considered as truly rigid. An inconsistency for the condition of $V_i = 4$ m/s is observed due to the increase in DAF with respect to the quasi-static for the aerated condition. This may be

attributed to the inconsistency in pressure loading, also explained in Section 4.2.2. As per R_F, insufficient tests have been conducted at higher R to determine the suitability of the quasi-static solution to predict maximum structural response. However, the boxed data points for the 3 mm plate are consistently lower than for the 2 mm plate highlighting the relevance of the plate natural frequency in the interaction. The mismatch in quasi-static classification between Figures 55a and 55b is potentially due to the underestimation of the relevance of the structural mass in the latter factor.

The justification for lack of DAF convergence to 1 for the zero aeration case are due to the simplifications associated with the quasi-static analytical solution in the denominator of the DAF, thus resulting in a load overprediction. For the impacts with aerated water, the quasi-static approach will result in an even greater over-prediction of the structural response. The pressure is assumed to be uniform across the length of the plate, and is thus an overestimation. Furthermore, the analytical theory neglects the air effects before the impact, where a pocket of air will be compressed between the wedge bottom and the water surface, affecting the free surface dynamics and providing additional impact cushioning. The load is not applied instantaneously, but rather develops along the length of the plate over time during wetting. Consequently, the added mass effects changes over time. All impact cases are subject to these effects, however, in other cases hydroelastic effects are also important.

Hydroelasticity: $R_F \leq 0.5$ & $R_S \leq 5$

The relevance of hydroelasticity is observed to be strongest for the lower values of R tested. The highest reductions in peak strain with respect to the analytical solution are attributed to pressure loading redistribution during the deformation which in turn reduces the strain acting on the assembly, as demonstrated in Section 4.3.2. This also highlights the importance of a strongly coupled two-way model due to the over-predictions by the quasi-static model, where the load propagation does not take any deformation into account. The deformation results in a reduction in load. The results in the red box in Figure 55 are shown in detail in Figure 56.

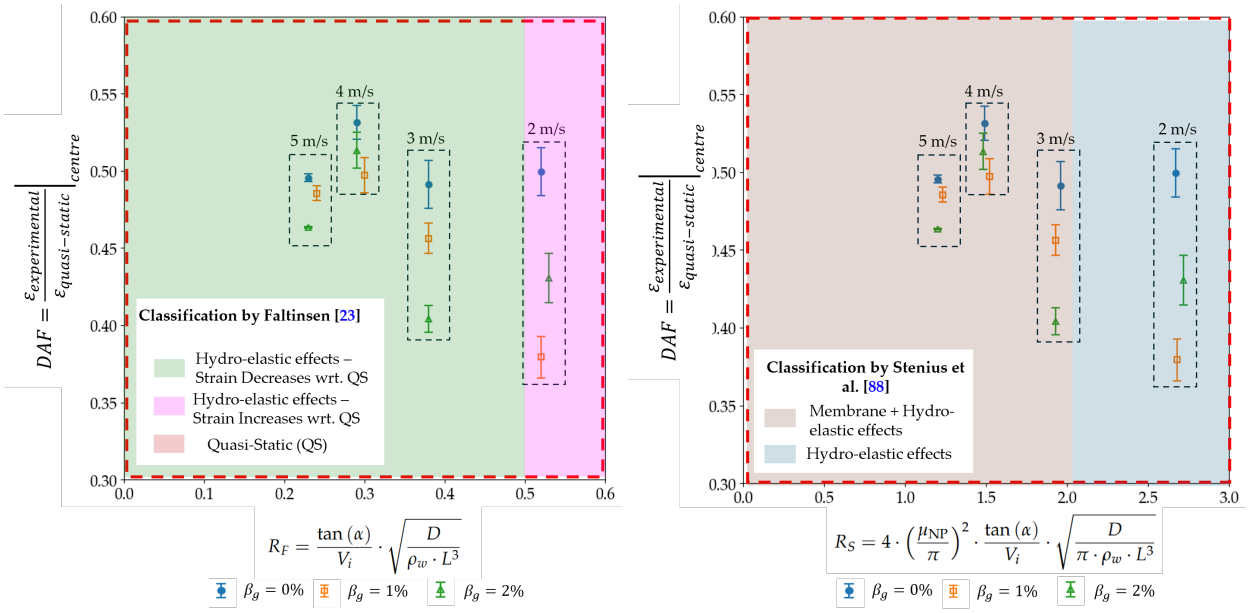

(a) R_F. (b) R_S.

Figure 56: Peak strain reduction at hydroelastic condition.

In non-aerated cases, a decrease in R_F should correspond to a lower DAF, however, this relationship was not evident in the results. For the cases without aeration, the load reduction might not be purely

due to hydroelastic effects. As per Figure 16a a substantial deflection is expected at the midpoint with regards to the length of the plate. Assuming the same DAF applies to the displacement as for the strain with regards to the quasi-static solution, the deformation exceeds 2% of the plate span, and thus membrane effects will have a secondary strain reduction influence [88] but an increase in local pressure due to restricted deformation. Stenius et al. [89] state that membrane effects will have a strong influence for $R_S \leq 2$ in combination with the hydroelastic effects. The governing load reduction mechanism is that once the deformation exceeds a certain value, the fibres in the plate are pulled in tension which has an additional load carrying effect.

A further reduction in the strains and in the DAF is observed when aeration is present. Higher aeration was not found to directly cause greater load reduction, with the reduction being directly related to the load distribution effect [98] and strain evolution over time. This was confirmed in Figures 50 and 51 and is influenced by the aeration at the water surface and the free surface profile before impact. The prevalent effect of hydroelasticity ensures that the combined mechanics of aeration and hydroelasticity for load reduction for $R << 1$ occur concurrently.

Strain Increase: $R_F \rightarrow 1$

A detailed view of the results from the 2 mm plate from Figure 55 is presented in Figure 57a. For the 2 mm plate, it is observed that the response is consistently shifted up higher than for the 1 and 3 mm plate cases. This effect arises because the wetted natural frequency of $\approx$ 515 Hz for this plate, calculated in Appendix 3 and confirmed by the knock tests, coincides with the forcing timescale. This frequency is present in the denominator of R. However, the points do not exceed DAF=1. Similar observations were made in Stenius [88], also attributed to the over-prediction in the quasi-static solution.

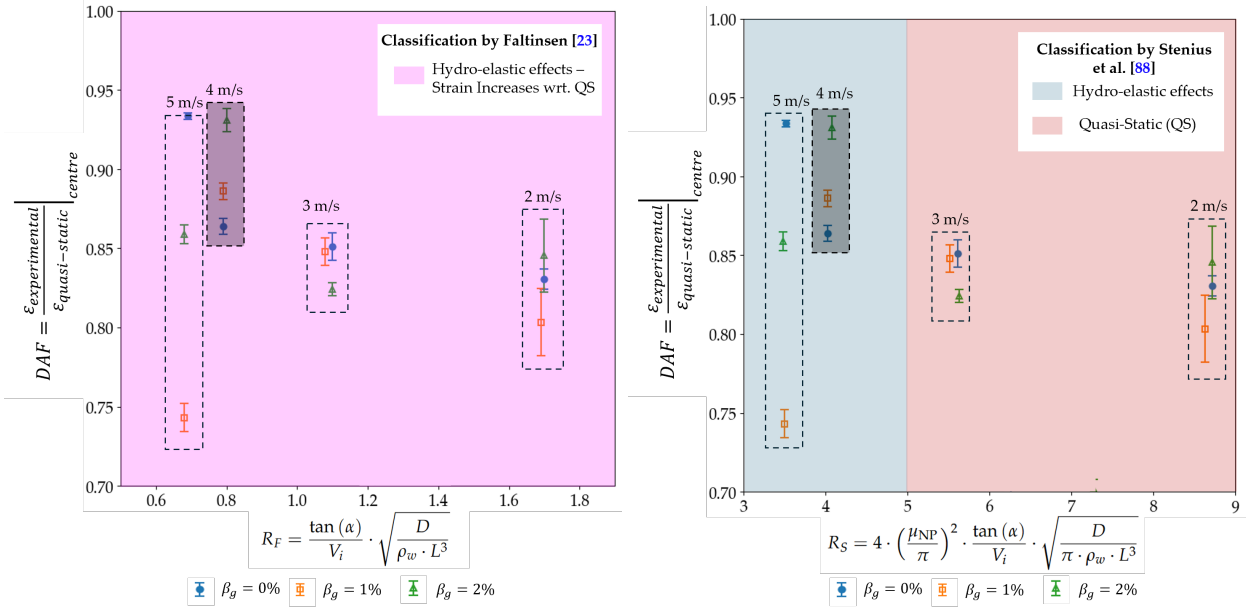

(a) R_F. (b) R_S.

Figure 57: Increase of peak loading due to the aeration.

For V_i=4 m/s marked in the black box in Figure 57, the strain increases with respect to the quasi-static solution for the non-aerated condition shown. This behaviour can be explained by aeration increasing the wetting time and slightly altering fluid density, which together shift R_F toward unity. Under these conditions the response aligns with the peak DAF, consistent with the classification in Figure 12. The dominant mechanism causing the load increase is the prolonged wetting time. The

strain increase does not exceed the quasi-static solution due to the pressure load overestimation, and physically, the loading condition does not approach quasi-static. A contradiction is observed in the interaction regime boundaries in Figure 57b where the cases for V_i=2-3 m/s are classified as quasi-static by R_S. This originates from using a regime classification based on the full analytical formulation of t_w and T_w rather than as a non-dimensional scaling factor. The boundary placement is also limited to the experimental conditions used by the respective authors, as seen in the results of Hosseinzadeh et al. [35].

4.5.2 Sub Research Question A:

How do structural stiffness, impact velocity, and aeration jointly govern structure loading and strain response?

The sub-question was tackled by varying the structural stiffness and impact velocity for various hydroelasticity conditions and testing several aeration fractions. The pressure results in isolation were shown to be inconclusive and would still require a semi-analytical or numerical model to obtain a strain response. Strain measurements were found to be more repeatable and directly comparable to a quasi-static solution.

For a condition of no aeration, the expected trends in absolute values of strain were observed. Lower structural stiffness was found to increase the peak strain on the structure. For each plate thickness, higher impact velocity was found to result in higher peak strain on the structure, matching previous experimental research. At conditions of prevalent hydroelastic effects for $R_F \leq 0.5$, the expected reduction in DAF for decreasing R_F was not observed. For impacts in aerated water, the physical principle of aeration was found to be consistent throughout irrespective of these effects of plate flexibility on load evolution. The affect of aeration is to cushion the impact, and thus the load is distributed over a longer time period. The captured effects of structural stiffness, impact velocity, and aeration on the strain response can be grouped as follows:

- $R_F \leq 0.5$ (Figure 56): A reduction in peak strain and in DAF with respect to the non-aerated condition was observed when introducing an air fraction into the water. DAF trends not matching literature and the response reduction due to aeration was due to variations in the local impact regions. Post impact oscillations due to impulsive load transfer as the wetting time is substantially shorter than the plate natural wetted period.

- $R_F \approx 1$ (Figure 57): An increase in peak strain and DAF with respect to the non-aerated condition was observed for the test case in closest proximity to $R_F = 1$, with the aeration condition causing convergence of the hydroelasticity factor to 1. A comparison of the DAF to R_F is required in this condition since the aerated water mechanics cause a closer match between t_w and T_w, with the increase in the former variable being the dominant influence of the response increase. The extent of strain response amplification and the effects of higher aeration fractions could not be determined at the resonant condition.

- $R_F \geq 2$ (Figure 55): For the stiffest plate at lowest impact velocity, a reduction peak strain and DAF with respect to the non-aerated condition was observed for higher values of aeration. Higher impact velocities for this plate were not consistently classified as quasi-static between the two classification schemes adopted. Consequently, some hydroelastic behaviour, and possibly load amplifications effects were present. The explanation for the region in the point above is also valid in this case.

For the test cases where $0.5 \leq R_F \leq 2$ excluding the one mentioned above, the observations regarding the effect of aeration on the strain response were inconsistent. A possible explanation is that

the hydroelastic strain increase in this category and non-repeatable free surface conditions have a compound effect which greatly effects the experimental results. Consequently, a more controlled test environment with more repetitions is required.

For the 3 conditions mentioned above, due to the inconsistencies with underlying hydroelastic conditions at $\beta_g = 0\%$, limited value can be added by quoting the % change in peak strain with respect to the non-aerated case. The conclusions are therefore limited to knowledge of the combined effects of aeration and hydroelasticity on the structure response with knowledge of the underlying behaviour due to structure flexibility. The results cannot be generalised with respect to the true DAF curve illustrated in Figure 5. Furthermore, for the absolute values of strain, it is also not possible to treat the load changes as statistically significant due to overlaps of the uncertainty bars with the mean values.

4.5.3 Sub Research Question B:

To what extent can the individual effects of hydroelasticity and aeration be distinguished, and across which conditions does each dominate?

For impacts with aerated water, a physical relationship between the load distribution over a longer time and the peak reduction is the same for both the added plate flexibility and the air volume in the water. For the most flexible construction at higher impact velocity, non-linear stiffening effects, where lower strain and a higher pressure peak due to less deflection were also observed [88]. However, for separation of the two effects, the relevance of the flexibility must be benchmarked with the plot in Figure 55. Considering the relative structural response denotes by the DAF, consistent effects were observed in the regions of $R_F < 0.5$ and for $R_F > 2$, and inconsistencies were well explained in terms of the aeration effects on the undisturbed water free surface prior to impact.

To answer the research question, hydroelastic effects are the dominant factor for benchmarking the structural response due to classification based on the wetting time and first wetted natural period. The dimensionless time ratio indicates the relative effects of these physical mechanics. When R_F is in close to 1, the additional effect due to the aeration mechanics can prologue the wetting time sufficiently such that it matches the first wetted natural period resulting in a resonant loading condition and a strain increase. This effect was only observed for the data point closest to the resonant condition. The low value of aeration tested were therefore found to augment the response based on the physical mechanisms identified above. Complete decoupling of the effects was not found within the test matrix used in this investigation.

To independently identify the effects of aeration on the fluid interaction, the density waves characteristic of impact in a compressible medium were also investigated using the approach in van der Eijk and Wellens [98], reported in Section 4.2.3. Using the current instrumentation system, it was not possible to detect the density waves. The lack of detection can be explained by the dominance of hydroelastic response in the flexible plate, the relatively low impact velocity, and limitations arising from sensor placement.

To better answer this research question, an experiment with controlled test conditions and with higher repeatability of the water surface shape is to be conducted. The first step would be to confirm the hydroelastic relationship for the condition with no aeration. Due to the pressure overprediction in the DAF, a new relation for the quasi-static condition is to be derived based on the collected experimental data, where stiffer plates are to be tested at lower impact velocity. The regimes as in Figure 12a are to be defined. Next several tests with different aeration conditions are to be executed. This approach was not deemed practical due to the complexity associated with plate changeover within a limited time frame.

4.6 Evaluation of Experiment

4.6.1 Design of Experiment

Using R_F and a uniform pressure load on a clamped-clamped Euler beam is common practice for hydroelasticity experiment design [35, 86, 89]. The test matrix served as a concrete starting point to answer the research question. However, it was not possible to conduct tests on a quasi-static case as done by van der Eijk and Wellens [98], and thus, no benchmark for the quasi-static strain response was available. Further test cases at higher plate stiffness and at lower impact velocity are required. Additionally, testing a stiff structure at higher velocity to reproduce the experiment by van der Eijk and Wellens [98] would enable the presented hypothesis on the energy content of the density waves to be tested, while also evaluating the experimental repeatability.

A conservative approach was taken for the test matrix to avoid premature plate yielding and failure at the clamped end, balancing out research validity and usability. No yielding and permanent deformation were detected throughout the experimental campaign. This approach was found to be overly conservative as the analytical theory used in Section 3.2 assumes instantaneous and uniform load application. In practice, the load will develop over a time frame between 50 - 200 ms depending on the impact velocity and will be more localised while forming a localised deadrise angle during the initial wetting stages of the impact.

4.6.2 Classification of Impact Regimes

Using a hydroelasticity factor R requires several key simplification such as assuming constant impact velocity, generalises the relevance of water jet development and omits non-linear interaction mechanics. Two classification regimes were used at design stage. The scheme by Faltinsen [24] represents a scaling, and that by Stenius [88] make use of calculated values of the wetting time and first wetted natural period depending on the boundary conditions. The first scheme was shown to demonstrate higher physical generality due to only including the essential variables to the interaction despite assuming constant impact velocity. However, for both schemes, the region of convergence to quasi-static is not well defined. It is therefore recommended to extend the experimental campaign to stiffer plates at lower impact velocities, and derive a formulation for the DAF to capture the hydroelastic effects. The transition between two regions where different physical effects are dominant was also not well established due to the aforementioned simplifications and discrete test conditions.

4.6.3 Contact Instrumentation

The uncertainty in pressure and strain measurements at $R_F \leq 0.5$, particularity at $\beta_g \geq 1$ limits a generalisation of the mutual interaction of aeration and plate flexibility. Repeatability for the pressure sensor measurements in particular was found to be poor in comparison to the strain gauges. The pressure sensors are directly exposed to the stochastics of the (aerated) water surface and experience positional change based on the local deadrise angle during impact, while the strain gauges are sheltered and only measure the response on the internal part of the wedge. Furthermore, the strain gauges were glued directly onto the plate while the pressure sensors were threaded into housings which were in turn glued into the plate, adding another degree of stiffness and contact flexibility affecting the pressure measurements. These observations therefore expose the limitations of relying on pressure sensors and using a numerical model to compute the structural response due to the issues with mounting pressure sensors on a flexible structure, notwithstanding the choice of numerical coupling and other simplifications required [92].

4.6.4 Experiment Insights

The experiment was crucial to identify the dominant physical mechanics for aeration over different hydroelastic regimes, which is the scientific contribution of this work. The small scale experiment was shown to be extremely sensitive to local effects such as variation in aeration in the water domain and the water surface, asymmetric impact and the tank domain boundary conditions. Furthermore, the expected trends for DAF when hydroelastic interacton is important for the pure aeration condition were not observed. Consequently, more research is required on ensuring experimental repeatability or with a larger experimental facility.

4.6.5 Additional Comments on Repeatability

The experimental uncertainty was calculated using the standard deviation (SD) σ and the relative standard deviation (RSD) (32) where N is the number of repeated tests, x_i the maximum value of individual test, and $\overline{x}$ is the mean peak value of the measurement.

$$\sigma = \sqrt{\frac{1}{N-1}\sum_{i=1}^{N}(x_i - \bar{x})^2} \qquad \text{RSD}(\%) = \frac{\sigma}{\overline{x}} \times 100 \tag{32}$$

For each individual condition in Tables 7 to 8, the mean and RSD were computed on the filtered signals. For the strain gauges, all RSD values were below 12%, with the exception of the cases where damage due to water ingress occurred. This implies a high degree of repeatability due to strain gauge isolation from direct (aerated) water impact. Only high frequency noise was present in the strain signals. Provided correct adhesion, the measurement area is constant between runs, unlike for the pressure sensors which are affected by free surface and hydroelastic development.

The pressure sensors demonstrated significantly higher RSD values, due to the differences in peak smoothness due to bubble interactions. Furthermore, for some impact conditions with relevant hydroelasticity, three tests were not sufficient to adequately assess experimental uncertainty due to the sensitivity of the experiments and instrumentation system. The uncertainty bars and overlaps with the mean data points are generally observed to be more prominent at higher impact velocities for thinner plates where the hydroelastic effects are expected to be more severe. For higher order membrane effects, the measurement uncertainty is also expected to increase. Measurement uncertainty was found to increase for test conditions combining physics of aeration and hydroelasticity, both of which add variability. Additional variability due to non-linear fluid effects such as cavitation are possible, but this was not observed in the present work.

4.6.6 Optical Instrumentation

The optical instrumentation was found to be useful only for test cases where the signal to noise ratio exceeds a certain threshold. The DIC was used to generate qualitative insights such as visualisations for the deformation in time along the plate, capturing the 3D effects on the flexible structure and the relative deformation peaks when aeration is present. For an application where the flexible structure is falling and deforming, the DIC data is inherently noisy. Despite the adjustments made to the wedge and top stiffener for optimal lines of sight, the results were effected by shadows and other edge effects. Further investigation into filtering techniques and sensitivity analysis is recommended to fully utilise the DIC for a deforming and falling application.

4.6.7 2D vs. 3D & Small Scale Effects

For an experiment which is perfectly 2D, the strains by s.g. 4-7 are expected to be identical in magnitude and rise time within an acceptable margin. However, a time and magnitude discrepancy between the four sensors at the fore and the aft was found, corresponding to an asymmetric impact, as per Figure 58. In such a case, the 4 strain gauges as marked would register a signal first, with the plate also being exposed to a 3D bending mode and 3D water effects. This was found to occur randomly, and the root cause could not be identified. The tank effects and the pressure boundary condition at the fore and aft are also relevant, particularly for cases of higher V_i due to more significant air compression effects.

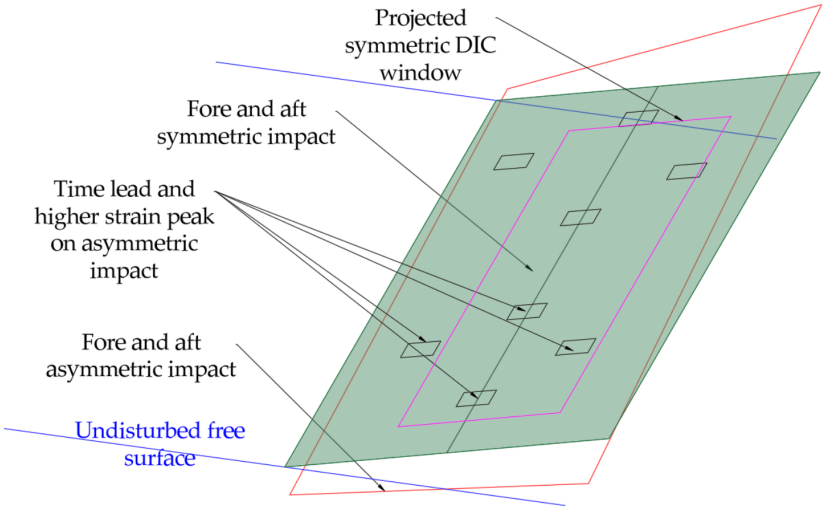

Figure 58: Illustration of asymmetric impact.

Despite designing the carriage and wedge to reproduce behaviour in two dimensions, the inherent edge effects and the random asymmetric impact introduce 3D effects. van der Eijk and Wellens [98] also comment about the 3D influence of the air bubble spatial and temporal distribution which limit the extent to which the experiment can be considered 2D. The overall small scale of the experimental setup and the constrained domain box result in higher sensitivity to physical boundaries. Consequently, strain gauges closest to the line of symmetry along which the pressure sensors will be the least affected by 3D effects, and these were used for analysis of an assessment of the hydroelastic interactions.

The carriage should be manufactured to tighter tolerances such that the impact is more repeatable. Alternatively, to compensate for misalignment in the tower guide rails, a mechanism using stiff springs such as to force the bearings to make consistent contact with the rails can be introduced, High stiffness is necessary such that this does not interfere with any of the natural modes of the setup. Such an approach would also require the use of lubrication to minimise the contact friction.

5 Conclusion

5.1 Conclusion

This thesis addresses the central question: **How does the aeration component in water influence the structural loading and response during hydroelastic slamming events?** A novel small-scale experiment was designed to generate the first dataset of loading and response for hydroelastic slamming of a flexible structure in aerated water.

The aeration was shown to alter the interaction by cushioning impulsive loads by distributing them over a longer time, and to alter the wetted natural frequency of the structure due to the water density change. However, the results demonstrate that a 1–2% air fraction can increase peak strain responses by up to 5% in conditions close to the resonant structural response. This finding is novel and significant because it suggests aeration can play a larger role in structural loading than previously recognized. The research question was answered through the following two sub-questions:

- Sub-Question 1: The experiments demonstrate that structural stiffness, impact velocity, and aeration content jointly govern the slamming response. The effect of the aeration component on the interaction is due to impulse redistribution over a longer time scale. In the impulsive cases with $R_F < 0.5$, peak strain responses were consistently reduced, whereas at $R_F \approx 1$, a 5% strain response amplification effect occurred due to resonance with the wetted natural period.

- Sub-Question 2: Under combined aeration and flexibility effects, structural response at low β_g is governed by the flexibility, represented by the hydroelastic classification. Slamming into aerated water modifies strain peaks through the same load-redistribution and resonance mechanisms, but the change and magnitude depends on the type of interaction and the air fraction in water, which alters the relation between impact duration and the wetted natural period of the structure.

From an engineering perspective, the findings show that aeration cannot simply be assumed to reduce slamming responses in all cases, and the structural mechanics must be taken into account. Near resonance, the loads can be amplified. For lightweight or flexible hulls designed for high speed, aeration must be considered as a variable that can either mitigate or exacerbate hydroelastic stresses. An appropriate quasi-static formulation must also be selected as a benchmark to properly predict the hydroelastic effects on which the aeration response modification is based. Beyond chine wetting, the vibrations at the natural frequency of the plating structures can also damage equipment and machinery on board. At the small experimental scale, load development and structural response were significantly affected by the local impact conditions, demonstrated by the uncertainty bars. Consequently, the effects of such a setup on experimental results and the associated limitations were documented in detail.

In summary, this study establishes a physical foundation and experimental dataset for validating coupled numerical models of hydroelastic impacts in aerated water. To enable broader validation, an expanded dataset is still required. The findings presented here advance understanding of slamming in aerated and breaking wave environments, supporting safer ship design through a more physically consistent representation of environmental loading and structural response. On this basis, the following recommendations for future work are proposed.

5.2 Recommendations for Future Work

5.2.1 Overall

A larger scale experimental setup is recommended to minimise the sensitivity to misalignments and manufacturing tolerances. More repetitions are advised, particularly for cases with thinner plates, high impact velocities and high aeration content. Higher carriage manufacturing tolerances will ensure that the impact is symmetrical.

5.2.2 Evaluation of Natural Modes

An instrumented impact hammer should be used to find the natural frequencies of the system. This hammer provides extensive information on the frequency response and damping behaviour of the structure and constituent substructures while also measuring the force amplitude and frequency content of the impact. This will enable a more complete evaluation of the natural system modes, enabling better mapping and decomposition of the pressure and strain signals in the frequency domain.

5.2.3 Hydroelasticity Classification

The hydroelasticity classification from Faltinsen [24] is to be used as it allows for generality. The methodology in Stenius [88] was useful due to the identified non-linear effects. However, for this specific experiment, a dedicated classification regime must be developed based on sufficient experimental data with repeated measurements as explained in Section 4.5.3. Specifically, the quasi-static regime and dynamic load amplification effects must be well quantified. The hydroelastic behaviour must first be verified, to serve as a benchmark for the aeration effects. The condition of $R_F = 1$ is of specific interest due to the additional strain increase due to aeration.

5.2.4 Aeration

An experimental campaign with more test cases, finer parameter changes, higher number of repetitions and more controlled experimental parameters is required to thoroughly evaluate the effects of aeration on a flexible structure. More aeration conditions should be tested to represent a wider range of possible physical conditions for ship bow slamming, and appropriate components to allow more airflow should be used. Furthermore, the resistance of the piping in the aeration system should be reduced to ensure homogenous airflow throughout the tank and at the surface of the water. The position of the undisturbed water level with respect to the light gate in all test conditions should be constant. The water level increase due to aeration should compensated for. Homogenous air bubble distribution will also help to reduce the local water surface curvature at the point of wedge impact. Furthermore, for the detection of the pressure waves, it is recommended to flush-mount a pressure sensor into the domain box. The pressure sensor will be stable and unaffected by the impact mechanics. The recommendations in this subsection follow from above to obtain a statistically accurate evaluation of the strain increase in the conditions around $R_F = 1$. During the impact with aerated water, a change in the impact noise was observed depending on the type of interaction. Acoustic reconstruction of the impact could also yield useful insights into the effects of aeration.

5.2.5 Free-Surface Visualisation

With the current setup, it is not possible to identify whether non-linear effects such as cavitation occur. Consequently, it is recommended to use a high speed camera with machine vision algorithms to capture the shape of the water free surface and the wedge deformation. This data would be extremely beneficial for the development and validation of numerical models. Such an implementation would require restructuring of the tank such that the stiffeners in the front are relocated.

References

[1] Full-scale measurements of slamming loads and responses on high-speed planing craft in waves. *Journal of Fluids and Structures*, 81:201–229, 2018. ISSN 0889-9746. doi: https://doi.org/10.1016/j.jfluidstructs.2018.05.006.

[2] Loss of containers overboard from msc zoe, 1-2 january 2019. Technical report, Panama Maritime Authority, Dutch Safety Board, and Federal Bureau for Maritime Casualty Investigation, 06 2020.

[3] Basler AG and Edmund Optics. Basler ace aca1920-150uc color usb 3.0 camera datasheet, 2025. URL https://www.edmundoptics.com/p/basler-aca1920-150uc-color-usb-30-camera/36890/. Part #36-740, Accessed from Edmund Optics on May 23, 2025.

[4] Ali Aghaei. *Numerical modelling of aeration and hydroelasticity in slamming loads and responses of marine structures*. PhD thesis, Gottfried Wilhelm Leibniz Universität Hannover, Fakultät für Bauingenieurwesen und Geodäsie, Hannover, Germany, 2022.

[5] Ali Aghaei, Stefan Schimmels, Torsten Schlurmann, and Arndt Hildebrandt. Numerical investigation of the effect of aeration and hydroelasticity on impact loading and structural response for elastic plates during water entry. *Ocean Engineering*, 201:107098, 2020. ISSN 0029-8018. doi: https://doi.org/10.1016/j.oceaneng.2020.107098.

[6] W. J. C. Boef. Launch and impact of free-fall lifeboats. part i. impact theory. *Ocean Engineering*, 19(2):119–138, 1992.

[7] A. D. Boon and P. R. Wellens. Probability and distribution of green water events and pressures. *Ocean Engineering*, 264:112429, November 2022. doi: 10.1016/j.oceaneng.2022.112429.

[8] H. Bredmose, D. H. Peregrine, and G. N. Bullock. Violent breaking wave impacts. part 2: modelling the effect of air. *Journal of Fluid Mechanics*, 641:389–430, 2009. doi: 10.1017/S0022112009991571.

[9] Bronkhorst High-Tech B.V. *EL-FLOW® Select: Digital Thermal Mass Flow Meters and Controllers for Gases*. Bronkhorst High-Tech B.V., October 2024. URL https://www.bronkhorst.com/products/gas-flow/el-flow-select/. Datasheet.

[10] Bas Buchner and Tim Bunnik. Extreme wave effects on deepwater floating structures. In *Proceedings of the Offshore Technology Conference (OTC)*, Houston, Texas, U.S.A., April 30-May 3 2007. Offshore Technology Conference. OTC 18493.

[11] G.N Bullock, A.R Crawford, P.J Hewson, M.J.A Walkden, and P.A.D Bird. The influence of air and scale on wave impact pressures. *Coastal Engineering*, 42(4):291–312, 2001. ISSN 0378-3839. doi: https://doi.org/10.1016/S0378-3839(00)00065-X.

[12] G.N. Bullock, C. Obhrai, D.H. Peregrine, and Henrik Bredmose. Violent breaking wave impacts: Part 1: Results from large-scale regular wave tests on vertical and sloping walls. *Coastal Engineering*, 54(8):602–617, 2006. ISSN 0378-3839. doi: 10.1016/j.coastaleng.2006.12.002.

[13] Zhenwei Chen, Jialong Jiao, Qiang Wang, and Shan Wang. Cfd-fem simulation of slamming loads on wedge structure with stiffeners considering hydroelasticity effects. *Journal of Marine Science and Engineering*, 10(11), 2022. ISSN 2077-1312.

[14] Hugh W. Coleman and W. Glenn Steele. *Experimentation, Validation, and Uncertainty Analysis for Engineers*. John Wiley & Sons, Inc., Hoboken, NJ, 2018. ISBN 9781119417514. doi: 10.1002/9781119417989.

[15] Wouter A. Cornel, Jerry Westerweel, and Christian Poelma. Non-intrusive, imaging-based method for shock wave characterization in bubbly gas–liquid fluids. *Experiments in Fluids*, 64 (2):Article 35, 2023. doi: 10.1007/s00348-022-03560-0. Final published version.

[16] Dantec Dynamics. *Istra4D Software Operation Manual*. Dantec Dynamics, a Nova Instruments Company, 2021. Manual Version: March 2021.

[17] Grant B. Deane and M. Dale Stokes. Scale dependence of bubble creation mechanisms in breaking waves. *Nature*, 418(6900):839–844, 2002. ISSN 1476-4687. doi: 10.1038/nature00967.

[18] Daniele Dessi, Daniel Sanchez-Alayo, Babak Shabani, and Jason Ali-Lavroff. Bow slamming detection and classification by machine learning approach. *Ocean Engineering*, 287:115646, 2023. ISSN 0029-8018. doi: https://doi.org/10.1016/j.oceaneng.2023.115646.

[19] Det Norske Veritas. *Recommended Practice: DNV-RP-C205, Environmental Conditions and Environmental Loads*, October 2010. Det Norske Veritas (DNV).

[20] Det Norske Veritas AS. *Rules for Classification of Det Norske Veritas AS: Newbuildings, Hull and Equipment – Main Class, Hull Structural Design – Ships with Length 100 Metres and Above*, January 2016. Official version available at http://www.dnvgl.com.

[21] Frédéric Dias and Jean-Michel Ghidaglia. Slamming: Recent progress in the evaluation of impact pressures. *Annual Review of Fluid Mechanics*, 50(Volume 50, 2018):243–273, 2018. ISSN 1545-4479. doi: https://doi.org/10.1146/annurev-fluid-010816-060121.

[22] M. Elhimer, N. Jacques, A. El Malki Alaoui, and C. Gabillet. The influence of aeration and compressibility on slamming loads during cone water entry. *Journal of Fluids and Structures*, 70: 24–46, 2017. ISSN 0889-9746. doi: https://doi.org/10.1016/j.jfluidstructs.2016.12.012.

[23] O. M. Faltinsen. The effect of hydroelasticity on ship slamming. *Philosophical Transactions of the Royal Society of London. Series A: Mathematical, Physical and Engineering Sciences*, 355(1724): 575–591, 1997. doi: 10.1098/rsta.1997.0026.

[24] Odd M. Faltinsen. Hydroelastic slamming. *Journal of Marine Science and Technology*, 5(2):49–65, December 2000. ISSN 1437-8213. doi: 10.1007/s007730070011.

[25] Odd M. Faltinsen. Slamming, whipping and springing. In *Hydrodynamics of High-Speed Marine Vehicles*, chapter 8, pages 286–341. Cambridge University Press, Cambridge, 2006. ISBN 9780511546068. doi: 10.1017/CBO9780511546068. Online publication date: September 2009.

[26] Odd M. Faltinsen, Jan Kvalsvold, and Jan V. Aarsnes. Wave impact on a horizontal elastic plate. *Journal of Marine Science and Technology*, 2:87–100, 1997.

[27] Festo SE & Co.KG. *SFAB-1000U-HQ10-PNLK-PNVBA-M12 Flow Sensor: Product Reliability Datasheet*. Festo SE & Co.KG, June 2025. URL https://www.festo.com/nl/nl/a/8162834/. Product reliability datasheet; part no. 8162834.

[28] Jean-Pierre Franc and Jean-Marie Michel. Introduction – the main features of cavitating flows. In *Fundamentals of Cavitation*, chapter 1, pages 1–30. Kluwer Academic Publishers, New York, Boston, Dordrecht, London, Moscow, 2004. ISBN 1-4020-2232-8. ©2005 Springer Science + Business Media, Inc.

[29] August Föppl. *Vorlesungen über technische Mechanik*, volume 6. B. G. Teubner, Leipzig, 1921. 6. Band, 4. Auflage.

[30] R. Grin and W. H. Pauw. Review of incidents resulting in loss of containers. Final Report 33039-1-SEA, MARIN (Maritime Research Institute Netherlands), 05 2022. MARIN order No. 33039.

[31] Sang Truong Ha, Long Cu Ngo, Muhammad Saeed, Byoung Jin Jeon, and Hyounggwon Choi. A comparative study between partitioned and monolithic methods for the problems with 3d fluid-structure interaction of blood vessels. *Journal of Mechanical Science and Technology*, 31(1): 281–287, 2017. ISSN 1976-3824. doi: 10.1007/s12206-016-1230-2.

[32] Elon Hendriksen. Deformation of structures upon impact with a liquid free surface. Master's thesis, Delft University of Technology, December 2022. To be defended publicly on December 14, 2022.

[33] Alan Henry, Ashkan Rafiee, Pal Schmitt, Frederic Dias, and Trevor Whittaker. The characteristics of wave impacts on an oscillating wave surge converter. *Journal of Ocean and Wind Energy*, 1(2):101–110, 2014. ISSN 2310-3604.

[34] Yao Hong, Benlong Wang, and Hua Liu. Experimental and numerical study on hydrodynamic impact of a disk in pure and aerated water. *Proceedings of the Institution of Mechanical Engineers, Part M: Journal of Engineering for the Maritime Environment*, 235(1):152–164, 2021. doi: 10.1177/1475090220933700. URL https://doi.org/10.1177/1475090220933700.

[35] Saeed Hosseinzadeh, Kristjan Tabri, Spyros Hirdaris, and Tarmo Sahk. Slamming loads and responses on a non-prismatic stiffened aluminium wedge: Part i. experimental study. *Ocean Engineering*, 279:114510, 2023. ISSN 0029-8018. doi: https://doi.org/10.1016/j.oceaneng.2023.114510.

[36] Saeed Hosseinzadeh, Kristjan Tabri, Ameen Topa, and Spyros Hirdaris. Slamming loads and responses on a non-prismatic stiffened aluminium wedge: Part ii. numerical simulations. *Ocean Engineering*, 279:114309, 2023. ISSN 0029-8018. doi: https://doi.org/10.1016/j.oceaneng.2023.114309.

[37] Hottinger Brüel & Kjær (HBK). Temperature compensation of strain gauge quarter bridges. https://www.hbkworld.com/en/knowledge/resource-center/articles/strain-measurement-basics/strain-gauge-fundamentals/article-temperature-compensation-of-strain-gauges/temperature-compensation-of-strain-gauge-quarter-bridges, n.d. Accessed: 2025-06-24.

[38] Zhengyu Hu and Yuzhu Li. Two-dimensional simulations of large-scale violent breaking wave impacts on a flexible wall. *Coastal Engineering*, 185:104370, 2023. ISSN 0378-3839. doi: https://doi.org/10.1016/j.coastaleng.2023.104370.

[39] Francisco J. Huera-Huarte, D. Jeon, and M. Gharib. Experimental investigation of water slamming loads on panels. *Ocean Engineering*, 38:1347–1355, August 2011. doi: 10.1016/j.oceaneng.2011.06.004.

[40] Fali Huo, Yupeng Zhao, Jingxi Zhang, Ming Zhang, and Zhi-Ming Yuan. Study on wave slamming characteristics of a typical floating wind turbine under freak waves. *Ocean Engineering*, 269:113464, 2023. ISSN 0029-8018. doi: https://doi.org/10.1016/j.oceaneng.2022.113464.

[41] International Digital Image Correlation Society. *Good Practices Guide for Digital Image Correlation*, 2018. URL https://www.idics.org/good-practices-guide. Print Version.

[42] Joint Accident Investigation Commission (JAIC). Final report on the capsizing on 28 september 1994 in the baltic sea of the ro-ro passenger vessel mv estonia. Technical report, The Governments of Estonia, Finland, and Sweden, Helsinki, Finland, December 1997. The English text is the authoritative version.

[43] Th. V. Kármán. *Festigkeitsprobleme im Maschinenbau*, pages 311–385. Vieweg+Teubner Verlag, Wiesbaden, 1907. ISBN 978-3-663-16028-1. doi: 10.1007/978-3-663-16028-1_5. URL https://doi.org/10.1007/978-3-663-16028-1_5.

[44] G. W. C. Kaye and T. H. Laby. *Tables of Physical and Chemical Constants and Some Mathematical Functions*. Longmans, Green, and Co., London, New York, Bombay, and Calcutta, 1911.

[45] T. I. Khabakhpasheva, A. A. Korobkin, and S. Malenica. Water entry of an elastic conical shell. *Journal of Fluid Mechanics*, 980, February 2024. ISSN 0022-1120. doi: 10.1017/jfm.2024.17.

[46] T.I. Khabakhpasheva and Alexander Korobkin. Elastic wedge impact onto a liquid surface: Wagner's solution and approximate models. *Journal of Fluids and Structures*, 36:32–49, January 2013. ISSN 0889-9746. doi: 10.1016/j.jfluidstructs.2012.08.004.

[47] Kenneth T. Kiger and James H. Duncan. Air-entrainment mechanisms in plunging jets and breaking waves. *Annual Review of Fluid Mechanics*, 44:563–596, 2012.

[48] Olivier Kimmoun, Šime Malenica, and Yves-Marie Scolan. Fluid structure interactions occurring at a flexible vertical wall impacted by a breaking wave. In *19th International Society of Offshore and Polar Engineers (ISOPE)*, pages 308–315, Osaka, Japan, 2009. hal-00454569.

[49] A. Korobkin, R. Guéret, and Š. Malenica. Hydroelastic coupling of beam finite element model with wagner theory of water impact. *Journal of Fluids and Structures*, 22(4):493–504, 2006. ISSN 0889-9746. doi: https://doi.org/10.1016/j.jfluidstructs.2006.01.001.

[50] A. A. Korobkin and T. I. Khabakhpasheva. Regular wave impact onto an elastic plate. *Journal of Engineering Mathematics*, 55:127–150, 2006. doi: 10.1007/s10665-006-9048-6.

[51] Jan Kvalsvold, Odd Magnus Faltinsen, and Jan Vidar Aarsnes. Effect of structural elasticity on slamming against wetdecks of multihull vessels. *Journal of ship and ocean technology*, 1:1–10, 1997.

[52] Kyowa Electronic Instruments Co., Ltd. *KFW/KFWS Waterproof Strain Gauges Instructions Manual*. Kyowa Electronic Instruments Co., Ltd., March 1999.

[53] Kyowa Electronic Instruments Co., Ltd. *KFW/KFWS Instruction Manual*. Kyowa Electronic Instruments Co., Ltd., 2025. URL https://product.kyowa-ei.com/en/products/strain-gages/type-kfws?tab=lineup. Instruction manual for small-sized waterproof foil strain gages (KFWS series). Accessed May 4, 2025.

[54] Inna Levitsky, Dorith Tavor, and Vitaly Gitis. Micro and nanobubbles in water and wastewater treatment: A state-of-the-art review. *Journal of Water Process Engineering*, 47:102688, 2022. ISSN 2214-7144. doi: https://doi.org/10.1016/j.jwpe.2022.102688.

[55] Kangping Liao, Changhong Hu, and Makoto Sueyoshi. Free surface flow impacting on an elastic structure: Experiment versus numerical simulation. *Applied Ocean Research*, 50:192–208, 2015. ISSN 0141-1187. doi: https://doi.org/10.1016/j.apor.2015.02.002.

[56] Ralf Lichtenberger. Email correspondence regarding dic camera setup. Personal communication, 2025. Query regarding 3D-DIc camera angles.

[57] Zhihua Ma, D.M. Causon, Ling Qian, C Mingham, Tri Mai, Deborah Greaves, and Alison Raby. Pure and aerated water entry of a flat plate. *Physics of Fluids*, 28, 01 2016. doi: 10.1063/1.4940043.

[58] Tri Mai, Cong Mai, Alison Raby, and Deborah Greaves. Aeration effects on water-structure impacts: Part 1. drop plate impacts. *Ocean Engineering*, 193:106600, 12 2019. doi: 10.1016/j.oceaneng.2019.106600.

[59] Tri Mai, Cong Mai, Alison Raby, and Deborah Greaves. Hydroelasticity effects on water-structure impacts. *Experiments in Fluids*, 61(9), 2020. doi: 10.1007/s00348-020-03024-3.

[60] Marine Accident Investigation Branch (MAIB). Report on the investigation of the structural failure of msc napoli, english channel, on 18 january 2007. Technical Report 9/2008, Marine Accident Investigation Branch, Southampton, United Kingdom, April 2008.

[61] S. Malenica, S. Seng, L. Diebold, Y. M. Scolan, A. A. Korobkin, and T. Khabakhpasheva. On three dimensional hydroelastic impact. In *Proceedings of the 9th International Conference on Hydroelasticity in Marine Technology*, pages 89–100, Rome, Italy, July 2022. Bureau Veritas.

[62] National Instruments. *TB-2706 Terminal Block for PXI Multifunction I/O Modules*, 2023. URL https://docs-be.ni.com/bundle/371459b/raw/resource/enus/371459b.pdf. Installation Guide.

[63] National Instruments. *TB-4330 Terminal Block for PXIe-4330/4331 Modules*, 2023. URL https://www.ni.com/docs/en-US/bundle/pxie-4330-4331-tb-4330-seri/resource/375486a.pdf. Installation Guide and Terminal Block Specifications.

[64] National Instruments. How is temperature affecting your strain measurement accuracy? https://www.ni.com/en/shop/data-acquisition/sensor-fundamentals/measuring-strain-with-strain-gages/how-is-temperature-affecting-your-strain-measurement-accuracy-.html, n.d. Accessed: 2025-06-24.

[65] National Instruments Corporation. Strain gauge measurement – a tutorial. Application Note AN078 (341023C-01), National Instruments, Austin, TX, August 1998.

[66] National Instruments Corporation. *PXIe-1078 Specifications*. National Instruments Corporation, May 2025. URL https://www.ni.com/docs/en-US/bundle/pxie-1078-specs/page/specs.html. Specifications document.

[67] Charlotte Obhrai, Geoffrey Bullock, Guido Wolters, Gerald Müller, Howell Peregrine, Henrik Bredmose, and Joachim Grüne. Violent wave impacts on vertical and inclined walls: Large scale model tests. In *Proceedings of the International Coastal Engineering Conference*, pages 4075–4086. World Scientific, April 2005. ISBN 9789812562982. doi: 10.1142/9789812701916_0329.

[68] Bing Pan, Jieyu Yuan, and Yong Xia. Strain field denoising for digital image correlation using a regularized cost-function. *Optics and Lasers in Engineering*, 65:9–17, 2015. ISSN 0143-8166. doi: https://doi.org/10.1016/j.optlaseng.2014.03.016. URL https://www.sciencedirect.com/science/article/pii/S0143816614001237. Special Issue on Digital Image Correlation.

[69] R. Panciroli. Water entry of flexible wedges: Some issues on the fsi phenomena. *Applied Ocean Research*, 39:72–74, 2013. ISSN 0141-1187. doi: https://doi.org/10.1016/j.apor.2012.10.010.

[70] R. Panciroli and M. Porfiri. Analysis of hydroelastic slamming through particle image velocimetry. *Journal of Sound and Vibration*, 347:63–78, 2015. ISSN 0022-460X. doi: https://doi.org/10.1016/j.jsv.2015.02.007.

[71] R. Panciroli, S. Abrate, G. Minak, and A. Zucchelli. Hydroelasticity in water-entry problems: Comparison between experimental and sph results. *Composite Structures*, 94(2):532–539, 2012. ISSN 0263-8223. doi: https://doi.org/10.1016/j.compstruct.2011.08.016.

[72] R. Panciroli, S. Abrate, and G. Minak. Dynamic response of flexible wedges entering the water. *Composite Structures*, 99:163–171, 2013. ISSN 0263-8223. doi: https://doi.org/10.1016/j.compstruct.2012.11.042.

[73] R. Panciroli, A. Shams, and M. Porfiri. Experiments on the water entry of curved wedges: High speed imaging and particle image velocimetry. *Ocean Engineering*, 94:213–222, 2015. ISSN 0029-8018. doi: https://doi.org/10.1016/j.oceaneng.2014.12.004.

[74] Riccardo Panciroli. *Hydroelastic Impacts of Deformable Wedges*, pages 1–45. Springer Netherlands, Dordrecht, 2013. ISBN 978-94-007-5329-7. doi: 10.1007/978-94-007-5329-7_1.

[75] Riccardo Panciroli, Tiziano Pagliaroli, and Giangiacomo Minak. On air-cavity formation during water entry of flexible wedges. *Journal of Marine Science and Engineering*, 6(4), 2018. ISSN 2077-1312. doi: 10.3390/jmse6040155.

[76] PCB Piezotronics, Inc. *Model M353B18 Platinum Stock Products High-Frequency Quartz Shear ICP® Accelerometer: Installation and Operating Manual*. PCB Piezotronics, Inc., 3425 Walden Ave., Depew, NY 14043, USA, . URL https://www.pcb.com.

[77] PCB Piezotronics, Inc. *Model 113B24 High-Frequency ICP® Pressure Sensor: Installation and Operating Manual*. PCB Piezotronics, Inc., 3425 Walden Ave., Depew, NY 14043, USA, . URL https://www.pcb.com.

[78] PCB Piezotronics, Inc. *Model 482A22 4-Channel, Line-Powered, ICP® Sensor Signal Conditioner: Installation and Operating Manual*. PCB Piezotronics, Inc., 3425 Walden Ave., Depew, NY 14043, USA, . URL https://www.pcb.com. Installation and Operating Manual.

[79] Pentair Aquatic Eco-Systems. Sweetwater air diffusers, 2025. URL https://pentairaes.com/sweetwater-air-diffusers. Accessed: 2025-05-27.

[80] Photron Limited. *FASTCAM SA-Z Hardware Manual, Rev. 4.06 E*. Rev. 4.06E.

[81] Photron Limited. *Photron FASTCAM SA-Z Technical Datasheet, Rev. 16.10.27*, Oct 2016. Available early 2017.

[82] Photron Limited. *Photron FASTCAM Viewer for High-Speed Digital Imaging: User's Manual, Ver. 4.3.0.0aE*, 2018.

[83] Louis-Romain Plumerault. *Numerical modeling of wave impacts on a wall: taking into account the presence of air in the water*. Theses, Laboratory of Applied Sciences for Civil and Construction Engineering, June 2009.

[84] Hanna Pot and Sebastian Schreier. An experimental study towards the application of digital image correlation for motion analysis of very flexible floating structures. Technical report, Delft University of Technology, 2023.

[85] Moritz Reinhard, Alexander Korobkin, and M. Cooker. Cavity formation on the surface of a body entering water with deceleration. *Journal of Engineering Mathematics*, 96, 05 2015. doi: 10.1007/s10665-015-9788-8.

[86] Zhongshu Ren, M. Javad Javaherian, and Christine M. Gilbert. Kinematic and inertial hydroelastic effects caused by vertical slamming of a flexible v-shaped wedge. *Journal of Fluids and Structures*, 103:103257, 2021. ISSN 0889-9746. doi: https://doi.org/10.1016/j.jfluidstructs.2021.103257.

[87] Adel Shams, Sam Z. Zhao, and Maurizio Porfiri. Analysis of hydroelastic slamming of flexible structures: modeling and experiments. *Procedia Engineering*, 199:1484–1488, 2017.

[88] Ivan Stenius. Finite element modelling of hydroelasticity in hull-water impacts. Trita-ave 2006:93, KTH Centre for Naval Architecture, Aeronautical and Vehicle Engineering, Royal Institute of Technology, Stockholm, Sweden, 2006. MSc thesis.

[89] Ivan Stenius, Anders Rosén, and Jörg Kuttenkeuler. Explicit fe-modelling of hydroelasticity in panel-water impacts. *International Shipbuilding Progress*, 54:111–127, 2007.

[90] Zhe Sun, K. Djidjeli, Jing Tang Xing, and Fai Cheng. Coupled mps-modal superposition method for 2d nonlinear fluid-structure interaction problems with free surface. *Journal of Fluids and Structures*, 61:295–323, 02 2016. doi: 10.1016/j.jfluidstructs.2015.12.002.

[91] Zhe Sun, A. Korobkin, X.P. Sui, and Zong Zhi. A semi-analytical model of hydroelastic slamming. *Journal of Fluids and Structures*, 101:103200, 2021. ISSN 0889-9746. doi: https://doi.org/10.1016/j.jfluidstructs.2020.103200.

[92] Igor Ten, Špiro Malenica, and Alexander Korobkin. Semi-analytical models of hydroelastic sloshing impact in tanks of liquefied natural gas vessels. *Philosophical Transactions of the Royal Society A: Mathematical, Physical and Engineering Sciences*, 369(1947):2920–2941, Jul 2011. doi: 10.1098/rsta.2011.0112.

[93] TT Electronics plc. *Slotted Optical Switch OPB819Z Datasheet*. TT Electronics | Optek Technology, Inc., 1645 Wallace Drive, Ste. 130, Carrollton, TX 75006, USA, November 2016. Product datasheet.

[94] M. van der Eijk. *Extreme aerated water-wave impacts on floating bodies: The relevance of air content in water on ship design loads*. Dissertation, Delft University of Technology, 2023. Final published version.

[95] M. van der Eijk and P. R. Wellens. Experimental, numerical and analytical evaluation of the buoyant wedge entry problem with reemergence in 2d. under review in Journal of Fluid Mechanics, 2023.

[96] Martin van der Eijk. Numerical modelling of homogeneous aerated-water wave impacts. Master's thesis, Delft University of Technology, Delft, Netherlands, November 2018. Thesis committee: Dr. Ir. J.J. Hopman (Ship Design), Dr. Ir. M.J.B.M. Pourquie (Fluid Mechanics), Dr. Ir. G.H. Keetels (Offshore and Dredging Engineering), Supervisor: Dr. Ir. P.R. Wellens (Ship Hydromechanics).

[97] Martin van der Eijk and Peter Wellens. An efficient bilinear interface reconstruction algorithm and consistent multidimensional unsplit advection scheme for accurate capturing of highly-curved interfacial shapes on structured grids. *Journal of Computational Physics*, 498:112656, 2024. ISSN 0021-9991. doi: https://doi.org/10.1016/j.jcp.2023.112656.

[98] Martin van der Eijk and Peter Wellens. An efficient pressure-based multiphase finite volume method for interaction between compressible aerated water and moving bodies. *Journal of Computational Physics*, 514:113167, 2024. ISSN 0021-9991. doi: https://doi.org/10.1016/j.jcp.2024.113167.

[99] T. van der Zee. The influence of aeration and deadrise angle on impact: An experimental and numerical study of the influence of deadrise angle and aeration on maximum impact pressure. Msc thesis, Delft University of Technology, Delft, The Netherlands, 2022.

[100] K.P. van Gent. The effect of aeration on the maximum pressure during wave impacts on a horizontal overhang: An experimental and numerical study of the effect of aeration on the maximum impact on a horizontal overhang. Msc thesis, Delft University of Technology, Delft, The Netherlands, 2023.

[101] Irja Viste-Ollestad, Terje L. Andersen, Narve Oma, and Sigvart Zachariassen. Investigation of an incident with fatal consequences on coslinnovator, 30 december 2015. Investigation Report 418005005, Petroleum Safety Authority Norway, 07 2016.

[102] T Von Karman. The impact on sea plane floats during landing. 1929.

[103] H. Wagner. Über stoss-und gleitvorgänge an der oberfläche von flüssigkeiten. *Zeitschrift für Angewandte Mathematik und Mechanik*, 12(4):193–215, 1932.

[104] Herbert Wagner. Über stoß- und gleitvorgänge an der oberfläche von flüssigkeiten. *ZAMM - Journal of Applied Mathematics and Mechanics / Zeitschrift für Angewandte Mathematik und Mechanik*, 12(4):193–215, 1932. ISSN 0044-2267. doi: 10.1002/zamm.19320120402.

[105] Ge Wang, Shaojie Tang, and Yung Shin. Direct calculation approach and design criteria for wave slamming of an fpso bow. *International Journal of Offshore and Polar Engineering*, 12(4): December, 2002. ISSN 1053-5381.

[106] Jingbo Wang, Claudio Lugni, and Odd Magnus Faltinsen. Experimental and numerical investigation of a freefall wedge vertically entering the water surface. *Applied Ocean Research*, 51: 181–203, 2015. ISSN 0141-1187. doi: https://doi.org/10.1016/j.apor.2015.04.003.

[107] Jingbo Wang, Claudio Lugni, and Odd Magnus Faltinsen. Analysis of loads, motions and cavity dynamics during freefall wedges vertically entering the water surface. *Applied Ocean Research*, 51:38–53, 2015. ISSN 0141-1187. doi: https://doi.org/10.1016/j.apor.2015.02.007.

[108] Shan Wang and C. Guedes Soares. Simplified approach to dynamic responses of elastic wedges impacting with water. *Ocean Engineering*, 150:81–93, 2018. ISSN 0029-8018. doi: https://doi.org/10.1016/j.oceaneng.2017.12.043.

[109] Kai Wei, Jie Hong, Mochen Jiang, and Wenyu Zhao. A review of breaking wave force on the bridge pier: Experiment, simulation, calculation, and structural response. *Journal of Traffic and Transportation Engineering (English Edition)*, 9(3):407–421, March 2022. doi: 10.1016/j.jtte.2021.03.006.

[110] Kai Wei, Jie Hong, and Yongle Li. Characterizing breaking wave slamming loads on bridge piers with probabilistic models of slamming maxima, rise and decay times. *Ocean Engineering*, 266:113097, 2022. ISSN 0029-8018. doi: https://doi.org/10.1016/j.oceaneng.2022.113097.

[111] Rik Wemmenhove. *Numerical simulation of two-phase flow in offshore environments*. PhD thesis, 2008. University of Groningen.

[112] A. B. Wood. *A Textbook of Sound*. G. Bell and Sons, Ltd., London, 1941.

[113] Wencheng Wu, Longfei Xiao, Yufeng Kou, and Mingyue Liu. Research on impact pressures in aerated water entry of a symmetrical wedge. *Journal of Fluid Mechanics*, 1010:A4, 2025. doi: 10.1017/jfm.2025.280.

[114] Zhi Yao, Fali Huo, Yuanyao Zhu, Chenxuan Tang, Kunqiao Jia, Dong Li, and Yong Ma. Experimental and numerical investigation on slamming mechanism of a mooring column-stabilised semi-submersible. *Processes*, 11(3), 2023. ISSN 2227-9717. doi: 10.3390/pr11030725.

[115] W.C. Young and R.G. Budynas. *Roark's Formulas for Stress and Strain*. McGraw-Hill International Edition. McGraw Hill LLC, 2001. ISBN 9780071501811.

Appendix 1: Wedge Construction

Appendix 1a: Construction Drawings

Table 13: List of drawings

Drawing Number	Drawing
1a	Front and back wedge walls
1b	Left and right side walls
1c	Keel Stiffener
1d	Bottom Flexible Plate
1e	Stiffener at top of carriage
2a	L profiles 1
2b	L profiles 2

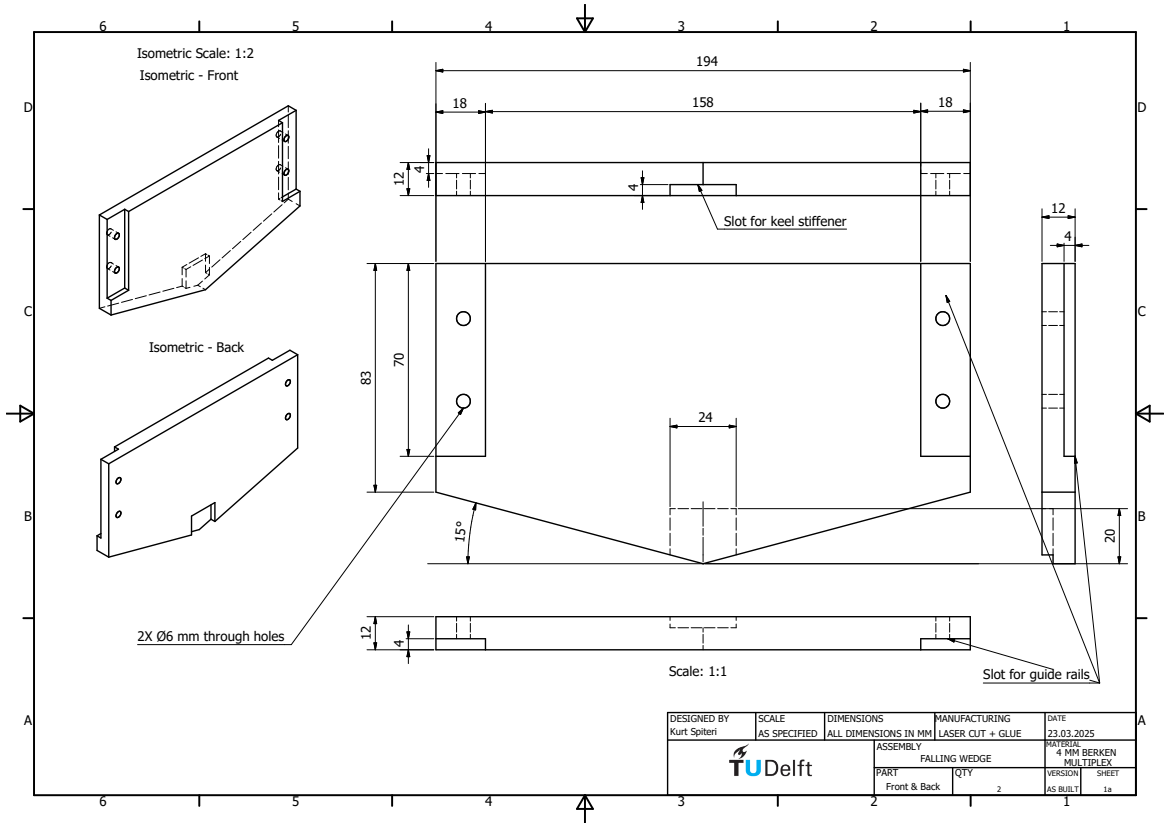

Figure 59: Front and rear walls of the wedge.

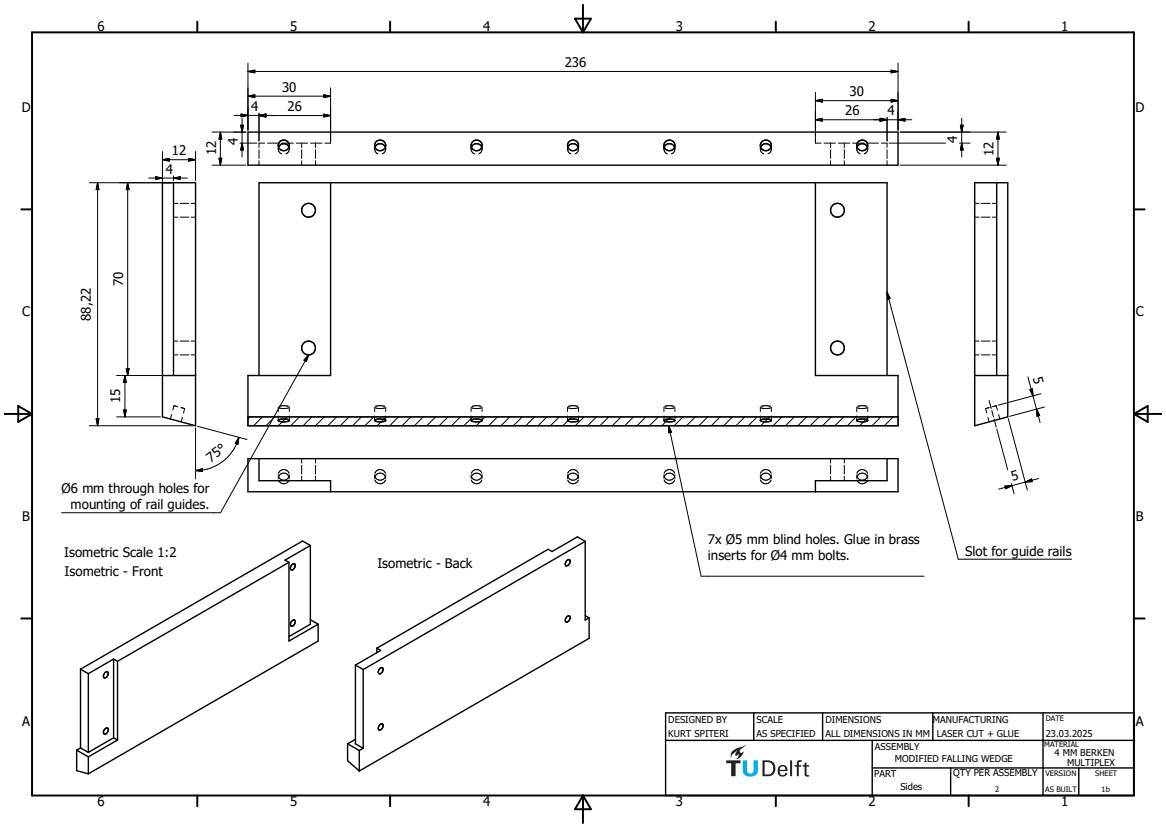

Figure 60: Fore and aft walls of the wedge.

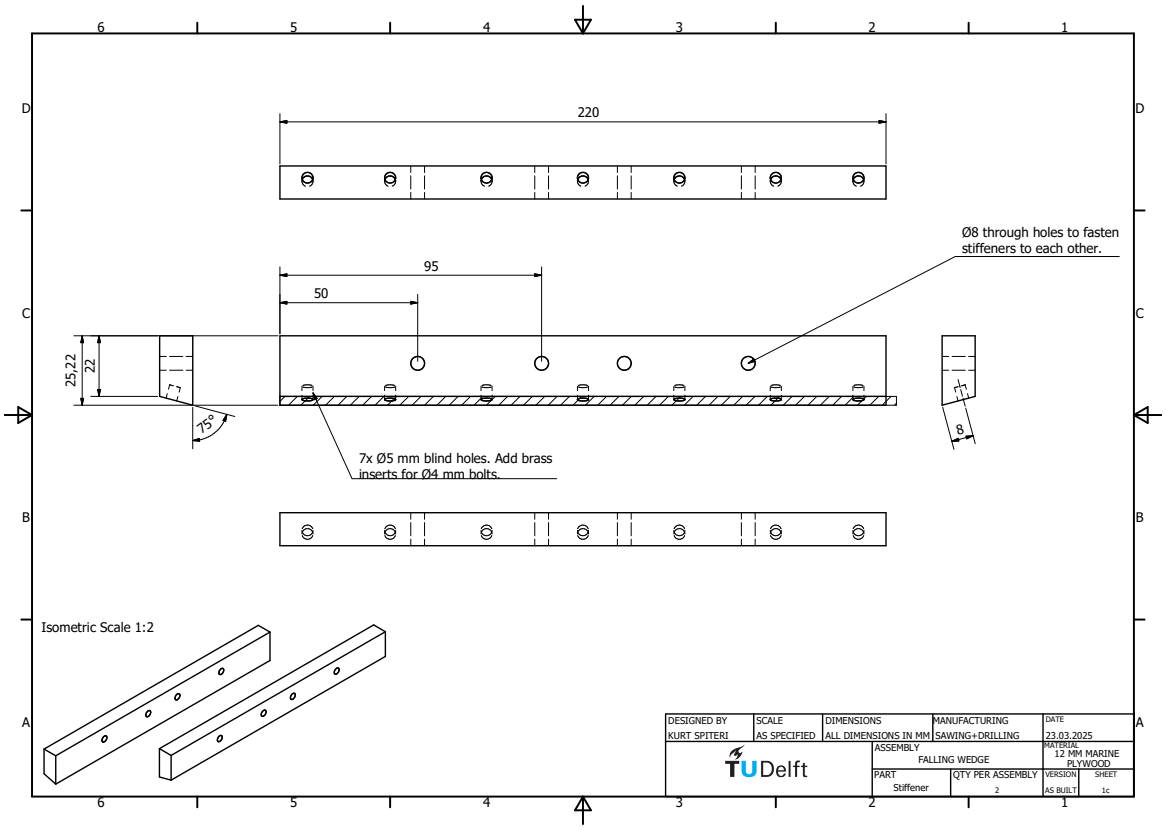

Figure 61: Port and starboard walls of the wedge.

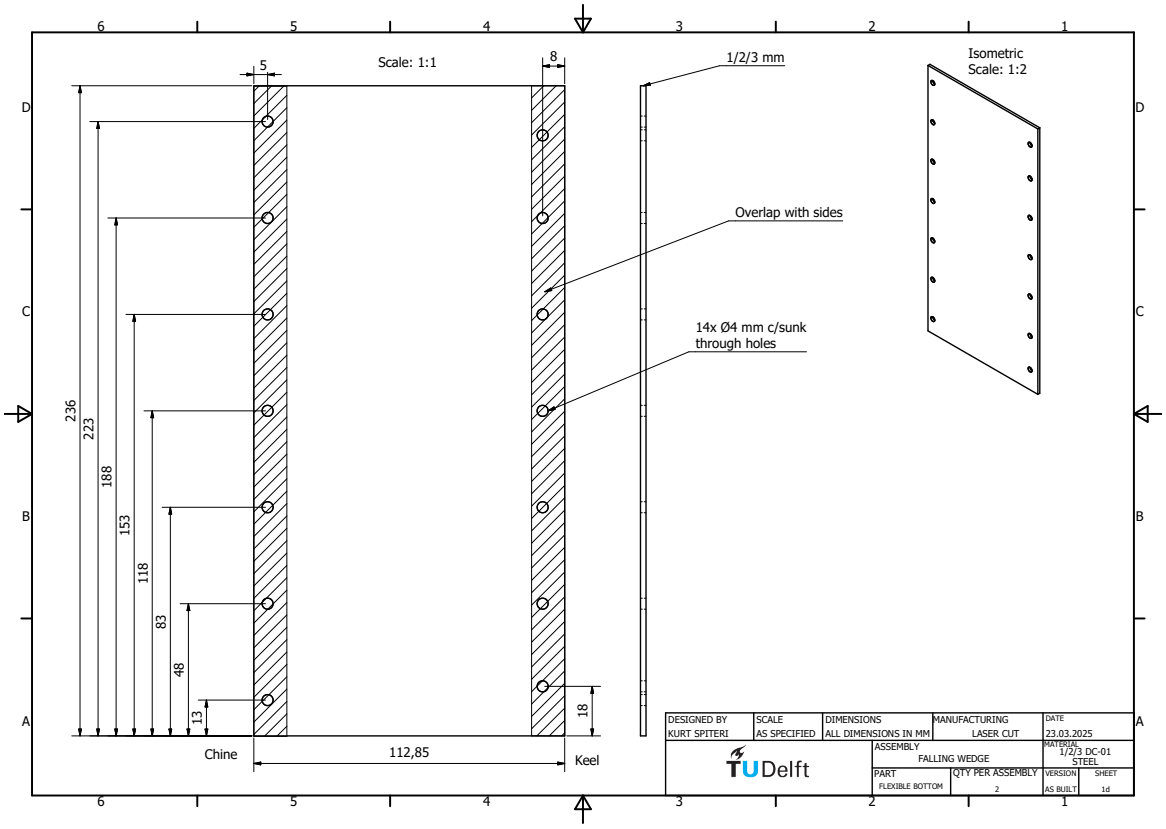

Figure 62: Flexible bottom plate.

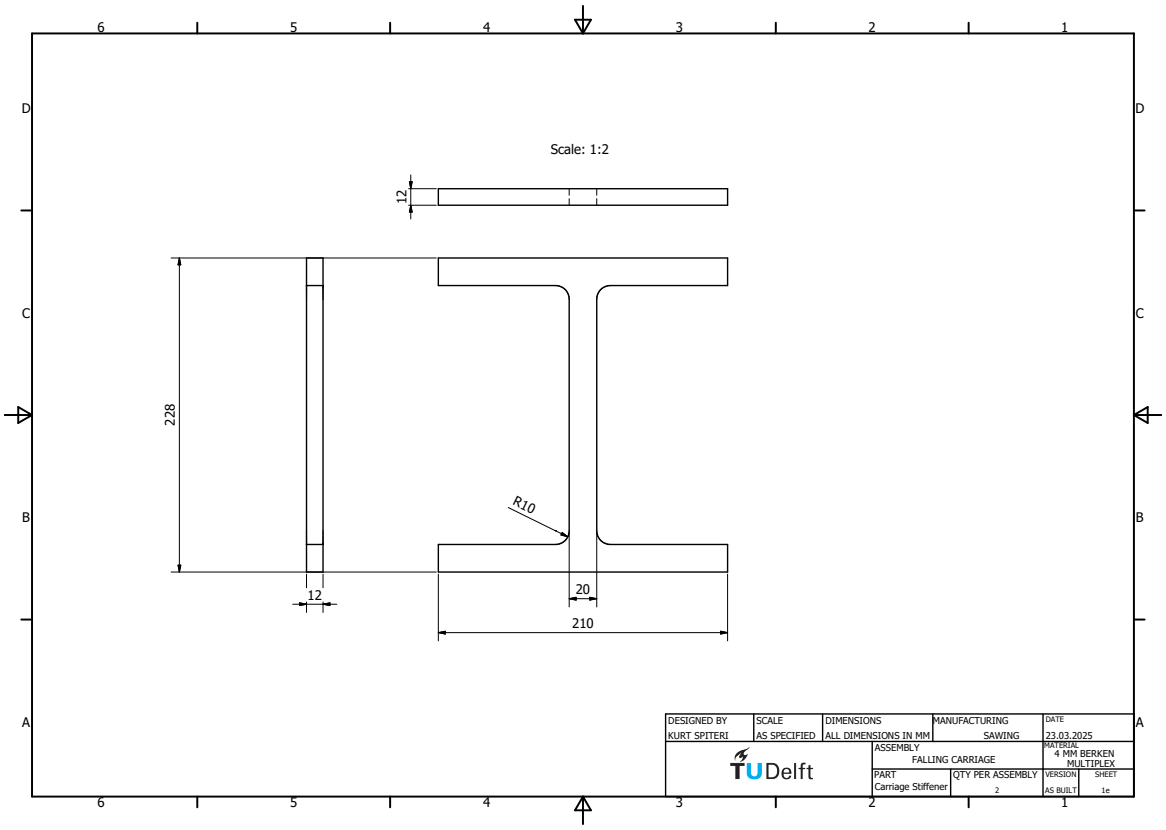

Figure 63: Stiffener at the top of the carriage.

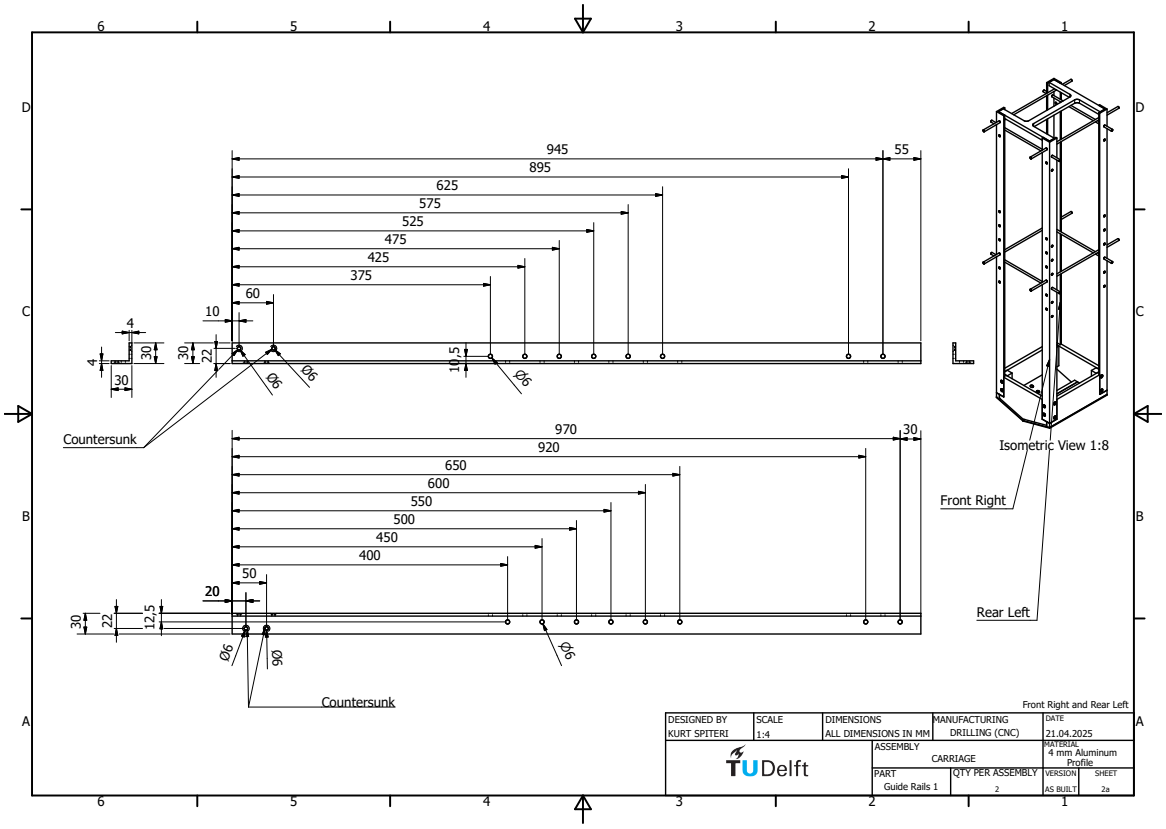

Figure 64: L profile.

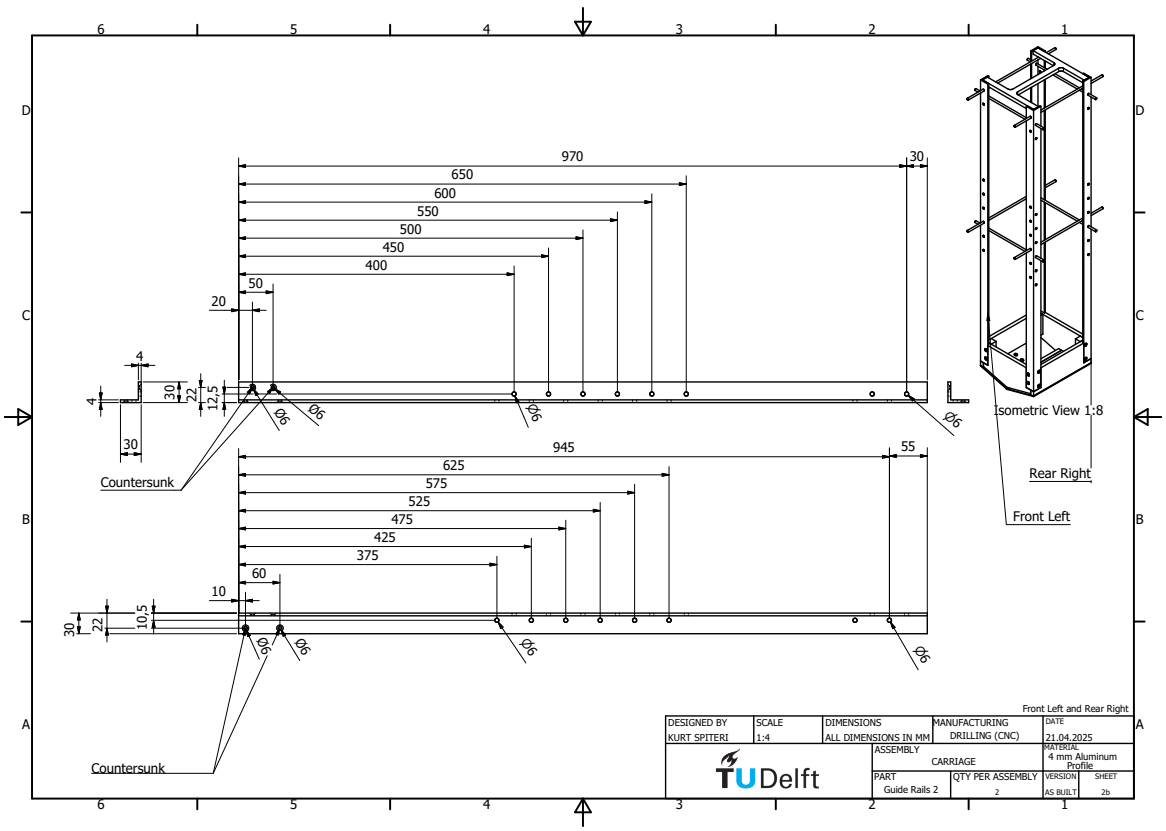

Figure 65: L profile.

Appendix 1b: Technical details

Bearings and Guide Rails

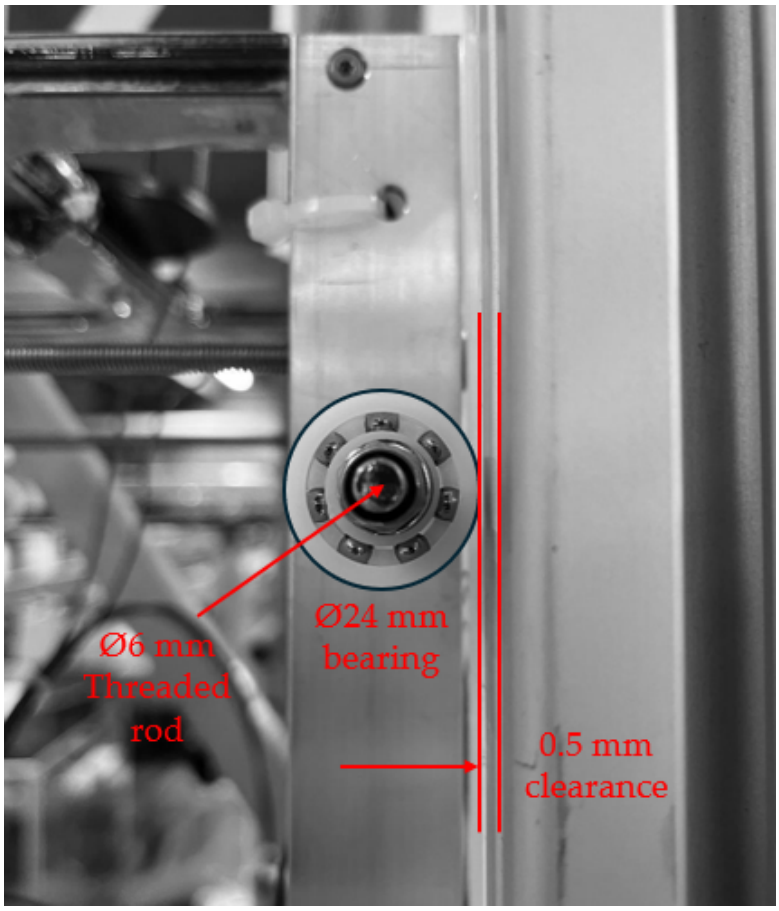

Figure 66: Detail of the bearing clearance against guide rails.

In practice, this clearance was larger due to manufacturing defects and misalignment. Consequently, the carriage was making intermittent contact with the rails.

Appendix 2: Flexible Wedge Natural Frequencies

For hydro-structural interaction, which is a one-way coupled interaction between the wedge bottom and the water:

$$f_{\text{hydro structural}} = \frac{1}{2 \cdot \pi} \sqrt{\frac{K_{11}}{M_{11}}} \tag{33}$$

For hydro-elastic interaction, which is two way coupled between the flexible bottom of the wedge and the water on impact. Let n be the number of the excited frequency harmonic:

$$f_{\text{hydro-elastic, n}} = \frac{1}{2 \cdot \pi} \sqrt{\frac{K_{nn}}{M_{nn} + A_{nn}}} \tag{34}$$

Derivation

Refer to Figure 13. Starting from the expression for the complex velocity potential:

$$\Phi(s) = i \cdot \left(V_i \cdot s - V_i \cdot \sqrt{s^2 - c^2} \right) \tag{35}$$

Verifying for the inner flow domain $|x| < c(t)$ at the water surface z=0, under approximation of the wedge with low deadrise angle as a plate

$$\Phi(x, z = 0) = -V_i \cdot \sqrt{c^2 - x^2} + i \cdot V_i \cdot x \qquad \longrightarrow \qquad \Phi(x, z = 0) = \varphi + i \cdot \psi \tag{36}$$

$$\varphi = -V_i \cdot \sqrt{c(t)^2 - x^2} \text{ at z=0} \tag{37}$$

Making a modification to (37) to account for the deflection velocity of the wedge $\bar{w}_{,t}$:

$$\varphi = (\bar{w}_{,t} - V) \cdot \sqrt{c(t)^2 - x^2} \tag{38}$$

Linearizing the Bernoulli equation for the modified velocity potential the pressure distribution is formulated, as illustrated in equation (40).

$$p(t, x) = -\rho_w \cdot \varphi_{,t} \tag{39}$$

$$p(t, x) = \rho_w \cdot V_i \cdot \frac{c(t)}{\sqrt{c(t)^2 - x^2}} \cdot \frac{\mathrm{d}c(t)}{\mathrm{d}t} - \rho_w \cdot \bar{w}_{,tt} \cdot \sqrt{c(t)^2 - x^2} - \rho_w \cdot \bar{w}_{,t} \cdot \frac{c(t)}{\sqrt{c(t)^2 - x^2}} \cdot \frac{\mathrm{d}c(t)}{\mathrm{d}t} \tag{40}$$

Concerning the hydro-elastic problem, the pressure formulation consists of three terms, the first term is the excitation force, the second term is proportional to deflection acceleration and is the added

mass. The last term is proportional to deflection velocity and is regarded as the added hydrodynamic damping.

Only the free vibration stage, which takes place once the wedge bottom is completely wetted is currently considered. Therefore the excitation force and added hydrodynamic damping are neglected. Therefore, the pressure formulation for the free vibration stage is reduced to equation (41).

$$p(t,x) = -\rho_w \cdot \bar{w}_{,tt} \cdot \sqrt{c(t)^2 - x^2} \tag{41}$$

The modal space-averaged acceleration is calculated as per (42).

$$\bar{w}_{,tt} = \frac{1}{c(t)} \int_0^{c(t)} \Psi_n dx \cdot a_{n,tt} = \frac{1}{c(t)} \int_0^{c(t)} \Psi_n dx \cdot \omega_{w,n} \cdot a_{n,t} \tag{42}$$

Substituting (42) in (41) and considering that the first mode is governing, the pressure formulation in the modal space is obtained as follows.

$$p(t,x) = -\rho_w \cdot \frac{1}{c(t)} \int_0^{c(t)} \Psi_1 dx \cdot \omega_{w,n} \cdot a_{1,t} \cdot \sqrt{c(t)^2 - x^2} \tag{43}$$

$$p(t,x) = \rho_w \cdot \omega_{w,1} \cdot V_i \cdot \frac{\int_0^{c(t)} \Psi_1 dx}{\int_0^{c(t)} \Psi_1^2 dx} \cdot sin(\omega_{w,1} \cdot t) \cdot \frac{1}{c(t)} \cdot \int_0^{c(t)} \Psi_1 dx \cdot \sqrt{c(t)^2 - x^2} \tag{44}$$

The space averaged pressure is computed as below:

$$p_{av} = \frac{1}{c_2 - c_1} \int_{c_1}^{c_2} p(t,x) dx \tag{45}$$

Space Dependant Solution for Clamped Clamped Beam

To compute the values of the above coefficients, an expression for the space dependant part of the free vibration solution $\Psi(x)$ is required. Consider the general solution for the space dependant part of the free vibration solution $w(t,x)$:

$$\Psi(x) = C_1 \cos(\beta_n x) + C_2 \sin(\beta_n x) + C_3 \cosh(\beta_n x) + C_4 \sinh(\beta_n x) \tag{46}$$

This formulation is based on the assumption of an exponential solution for the space dependant part. The following boundary conditions are used.

At the clamped ends, the deflection is 0:

$$\Psi(x=0) = 0 \rightarrow C_1 \cos(\beta_n \cdot 0) + C_2 \sin(\beta_n \cdot 0) + C_3 \cosh(\beta_n \cdot 0) + C_4 \sinh(\beta_n \cdot 0) = 0 \rightarrow C_1 + C_3 = 0 \tag{47}$$

$$\Psi(x=L) = 0 \rightarrow C_1 \cos(\beta_n \cdot L) + C_2 \sin(\beta_n \cdot L) + C_3 \cosh(\beta_n \cdot L) + C_4 \sinh(\beta_n \cdot L) = 0 \tag{48}$$

At the clamped ends, the rotation is also 0:

$$\Psi'(x=0) = 0 \rightarrow \beta_n \left[-C_1 \sin(\beta_n \cdot 0) + C_2 \cos(\beta_n \cdot 0) + C_3 \sinh(\beta_n \cdot 0) + C_4 \cosh(\beta_n \cdot 0)\right] 0 \rightarrow B_1 + D_1 = 0 \tag{49}$$

$$\Psi'(x=L)=0 \rightarrow -C_1\beta_n \sin(\beta_n \cdot L) + C_2\beta_n \cos(\beta_n \cdot L) + C_3\beta_n \sinh(\beta_n \cdot L) + C_4\beta_n \cosh(\beta_n \cdot L) = 0 \tag{50}$$

Compiling the determinants into a matrix, and solving for the determinant is equal to 0:

$$\begin{bmatrix} 1 & 0 & 1 & 0 \\ 0 & 1 & 0 & 1 \\ \cos(\beta_n L) & \sin(\beta_n L) & \cosh(\beta_n L) & \sinh(\beta_n L) \\ -\sin(\beta_n L) & \cos(\beta_n L) & \sinh(\beta_n L) & \cosh(\beta_n L) \end{bmatrix} \tag{51}$$

The allowable values for $\beta_n \cdot L$ are found from setting the determinant for system of equations (51) equal to 0 for a non-trivial solution.

$$\cos^2(\beta_n L) - 2\cos(\beta_n L)\cosh(\beta_n L) + \sin^2(\beta_n L) + \cosh^2(\beta_n L) - \sinh^2(\beta_n L) = 0 \tag{52}$$

Which simplifies to:

$$\cos(\beta_n L)\cosh(\beta_n L) = 1 \tag{53}$$

The solutions for the first, second and third mode shape respectively for $\beta_n \cdot L$ are 4.730, 7.853, 10.996. The wave numbers β_n yield the natural frequencies for each mode n, and L is the length of the plate strip being considered.

Due to the nature of the formulation, D_1 was set to 1 for the purpose of normalisation. Consequently, the other coefficients were expressed as a function of D_1 as follows:

$$A_1 = D_1 \cdot \frac{-\sinh(\beta_n L) + \sin(\beta_n L)}{-\cosh(\beta_n L) + \cos(\beta_n L)} \tag{54}$$

$$B_1 = -D_1 \tag{55}$$

$$C_1 = -D_1 \cdot \frac{-\sinh(\beta_n L) + \sin(\beta_n L)}{-\cosh(\beta_n L) + \cos(\beta_n L)} \tag{56}$$

D_1 is set to 1 for normalisation of the space dependant part of the boundary condition. Mathematically, the value used for the normalisation will cancel out for the deflection w due to being involved in the numerator of Ψ and the denominator of Φ.

Coefficient Formulations

Consider the Euler Beam equation of motion in modal space.

$$\rho_s \cdot A \cdot w(t,x)_{,tt} + EI \cdot w(t,x)_{,xxxx} = p(x,t) \tag{57}$$

Using the formulation in (39) and (40) for the RHS of (57):

$$\begin{aligned} \rho_s \cdot A \cdot \int_0^L \Psi_m^2 dx \cdot a_{m,tt} + EI \cdot \int_0^L \Psi_m \cdot \Psi_{m,xxxx} dx \cdot a_m = \\ \rho_w \cdot V_i \cdot c \cdot \frac{dc}{dt} \cdot \int_0^c \frac{\Psi_m}{\sqrt{c^2-x^2}} dx - \rho_w \cdot \int_0^c \Psi_m \cdot \sqrt{c^2-x^2} dx \cdot \frac{1}{c} \int_0^c \Psi_n dx \cdot a_{n,tt} \\ -\rho_w \cdot c \cdot \frac{dc}{dt} \cdot \int_0^c \frac{\Psi_m}{\sqrt{c^2-x^2}} dx \cdot \frac{1}{c} \int_0^c \Psi_n dx \cdot a_{n,t} \end{aligned} \tag{58}$$

By grouping the time derivatives of $a(t)$ and arranging, the following coupled system of equations will be obtained for $0 \leq c(t) \leq (s_s)$.

$$[M + A(t)] \cdot \{a(t)_{tt}\} + [D(t)] \cdot \{a(t)_t\} + [K] \cdot \{a(t)\} = \{F(t)\} \tag{59}$$

For the free vibration, the excitation force and added hydro-dynamic damping are equal to 0. The system of equations for the free vibration case is therefore:

$$[M + A(t)] \cdot \{a(t)_{tt}\} + [K] \cdot \{a(t)\} = 0\} \tag{60}$$

For the **structural stiffness**:

$$K_{nn}(E, \nu, t_p, \Psi_n(x), L) = EI \cdot \beta_n^4 \cdot \int_0^L \Psi_n^2 dx \tag{61}$$

A modification is made to EI to account for the additional plate bending. EI is therefore replaced by the modified plate flexible rigidity. However, ψ for the clamped beam was used for simplicity.

$$K_{nn}(E, \nu, t_p, \Psi_n(x), L) = \frac{E \cdot {t_p}^3}{12(1-\nu^2)} \cdot \beta_n^4 \cdot \int_0^{s_s} \Psi_n^2 dx \tag{62}$$

For the **added mass** (note that the density of water is being used).

$$A_{nn}(\rho_w, \Psi_1(x), L, L) = \rho_w \cdot \int_0^c \Psi_n \cdot \sqrt{c^2 - x^2}\, dx \cdot \frac{1}{c} \int_0^c \Psi_n\, dx \tag{63}$$

To find c(t) for the wedge when the wedge length is completely wetted via the modal analysis, assuming that the velocity remains constant. Refer to Figure 13 for a simplified illustration of $c(t)$.

Table 14: Hydro–structural and hydroelastic natural frequencies for varying plate thickness t_p.

t_p (mm)	**1**	**2**	**3**
f_{hs} (Hz)	559	1118	1600
$f_{he,1,modal}$ (Hz)	192	515	907
$f_{he,1,analytical}$ (Hz)	182	526	909
$f_{he,2,modal}$ (Hz)	1541	3082	4623

Appendix 3: DIC

A3.1 Connection and Wiring

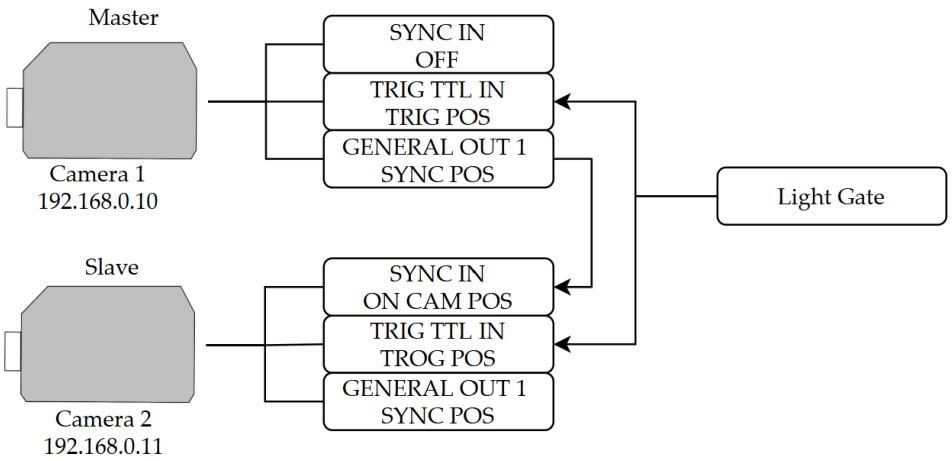

Figure 67: Schematic of camera wiring.

A3.2 Calibration Parameters

Table 15: Sample camera calibration parameters

Intrinsic Parameters - Camera 1	
Focal length {x; y}	{4150.0 ± 1.4; 4144.9 ± 1.4}
Principal point {x; y}	{500.6 ± 1.5; 145.3 ± 1.1}
Radial distortion {r_2; r_4}	{0.358 ± 0.003; 29.1 ± 0.4}
Tangential distortion {p_x; p_y}	{0.0004 ± 0.0003; -0.0029 ± 0.0003}
Extrinsic Parameters - Camera 1	
Rotation vector {x; y; z}	{0.03055 ± 0.00014; 3.0388 ± 0.0004; -0.7653 ± 0.0004}
Translation vector {x; y; z}	{-74.7 ± 0.4; 23.7 ± 0.3; 1182.8 ± 0.4}
Intrinsic Parameters - Camera 2	
Focal length {x; y}	{4160.6 ± 1.4; 4154.7 ± 1.4}
Principal point {x; y}	{512.4 ± 1.1; 288.0 ± 1.2}
Radial distortion {r_2; r_4}	{0.344 ± 0.003; 25.9 ± 0.4}
Tangential distortion {p_x; p_y}	{-0.0004 ± 0.0002; 0.0039 ± 0.0002}
Extrinsic Parameters - Camera 2	
Rotation vector {x; y; z}	{3.1369 ± 0.0003; -0.02953 ± 0.00007; -0.0286 ± 0.0004}
Translation vector {x; y; z}	{62.3 ± 0.3; 6.0 ± 0.4; 1201.1 ± 0.4}
Stereo Parameters	
Angle	27.6064°
Baseline	559.609 mm

A3.3 Calibration Methodology

Several calibration frames are shown in the below figures. The calibration plate at an initial angle matching the deadrise angle was moved around the region of interest and captured by both the master and the slave cameras.

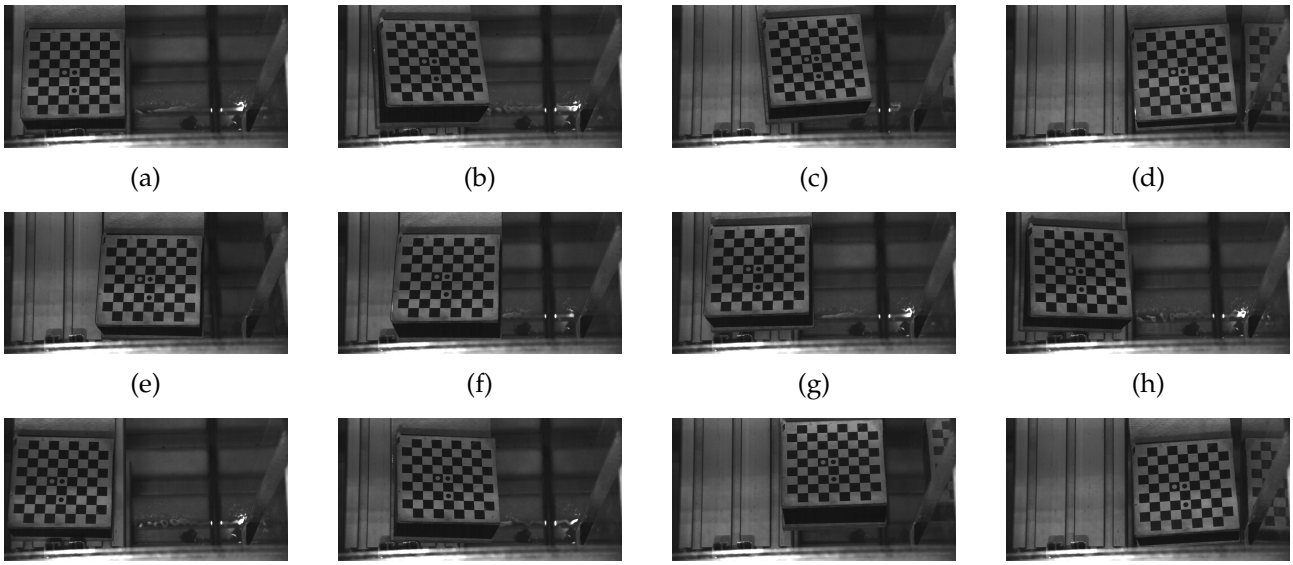

(a) (b) (c) (d)

(e) (f) (g) (h)

(i) (j) (k) (l)

Figure 68: Master camera calibration frames.

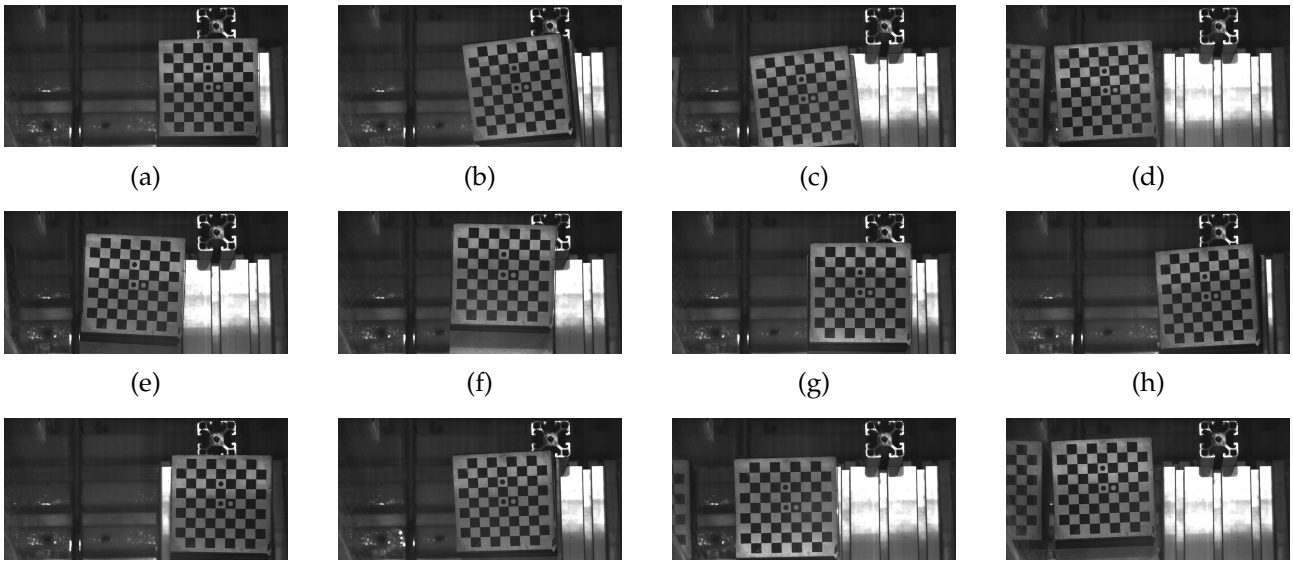

(a) (b) (c) (d)

(e) (f) (g) (h)

(i) (j) (k) (l)

Figure 69: Slave camera calibration frames.

A3.4 Calculation of Impact Velocity

A3.4.1 Mean Impact Velocity

This section describes how the rigid-body velocity of the carriage assembly v_c and displacement z_c of the falling carriage are obtained from the accelerometer on top of the rigid carriage. The light-gate voltage is used to determine the times when the trigger on the carriage enters and leaves the optical beam. Let t_{in} and t_{out} denote the times at which the trigger of known length $L_{trigger}$ first crosses and leaves the light gate respectively, shown in Figure 70. t_{in} will be 0 s as the datum at which all the measurements are synchronised when the light gate leading edge goes to 5V.

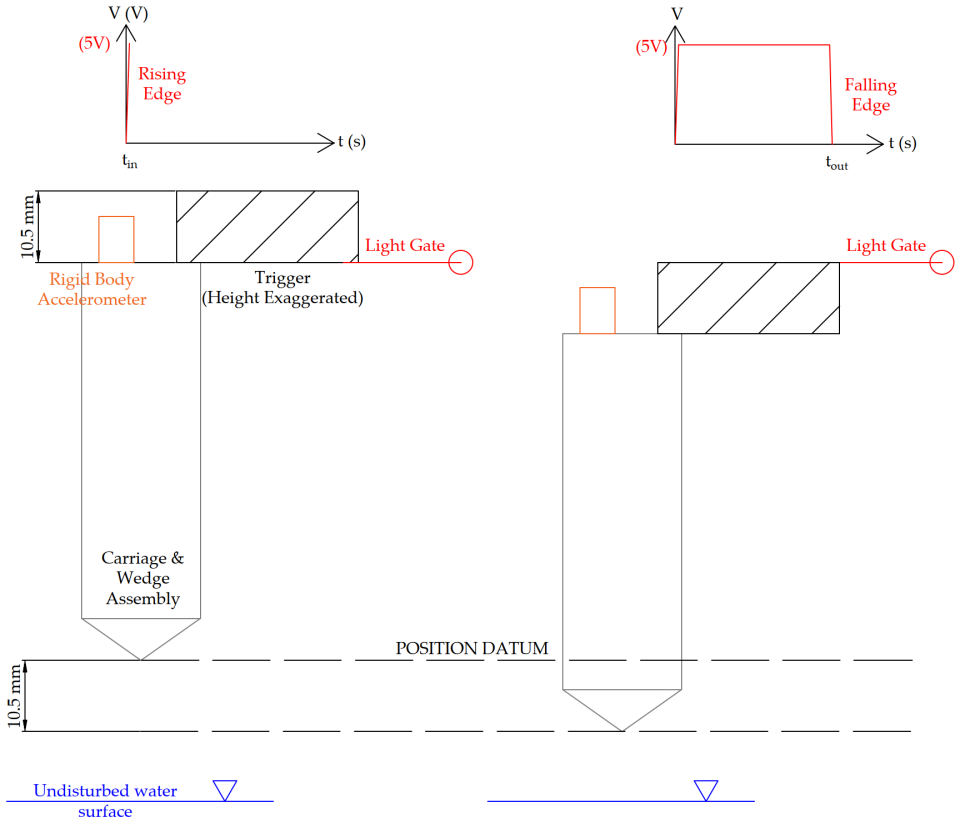

Figure 70: Schematic for displacement calculation. First rising edge t_{in} and falling edge t_{out} are shown.

$$\bar{v}_{gate} = -\frac{L_{trigger}}{t_{out} - t_{in}}, \tag{64}$$

A3.4.2 Displacement

The displacement was calculated from an integration of the signal from accelerometer $a_{sig}(t)$ on top of the carriage capturing rigid body motion. The accelerometer signal in Volts was first converted to m/s^2 with the calibration $a_{cal}(t) = C_a\, a_{sig}(t)$ with C_a from Table 6. To remove small constant sensor offsets, the mean acceleration before the light–gate trigger ($t < t_{in}$) was computed and subtracted from the entire signal. This ensures that integration does not accumulate an artificial drift from a tiny constant bias:

$$\tilde{a}(t) = a_{cal}(t) - \frac{1}{t_{in} - t_0} \int_{t_0}^{t_{in}} a_{cal}(\tau)\, d\tau. \tag{65}$$

where $a_{cal}(t)$ is the calibrated acceleration in SI units, $\tilde{a}(t)$ is the bias–corrected acceleration, t_0 is the start of the measurement record, and t_{in} is the instant the carriage first enters the light gate. A zero–phase Butterworth

high–pass filter with cut–off $f_c = 0.5\,\text{Hz}$ was then used to suppress low–frequency drift. Let $a_{\text{hp}}(t)$ denote the high-pass filtered signal. An FFT was used to integrate in time with the DC term set to zero. To obtain velocity or displacement, the signal is transformed to the frequency domain, divided by $(i\omega)^r$, and transformed back.

Let $\mathcal{F}\{\cdot\}$ denote the Fourier transform and define

$$\hat{a}(\omega) = \mathcal{F}\{a_{\text{hp}}(t)\},$$

where $a_{\text{hp}}(t)$ is the high–pass filtered acceleration signal, $\omega = 2\pi f$ is the angular frequency (rad/s), and f is the ordinary frequency (Hz). The key property used is that integration in time corresponds to division by $i\omega$ in the frequency domain. For the r–fold time integral ($r = 1$ for velocity, $r = 2$ for displacement),

$$\mathcal{F}\Big\{ \underbrace{\int \cdots \int}_{r} a_{\text{hp}}(t)\, dt \Big\} = \frac{\hat{a}(\omega)}{(i\omega)^r}. \tag{66}$$

The first integration gives velocity $v_c(t)$; a second gives displacement $z_c(t)$. The constant terms of integration for the velocity was set as $\overline{v}_{\text{gate}}$ at light gate falling edge, and for the displacement as L_{trigger} for this same position.

A3.5 Calculation of Local Deformation

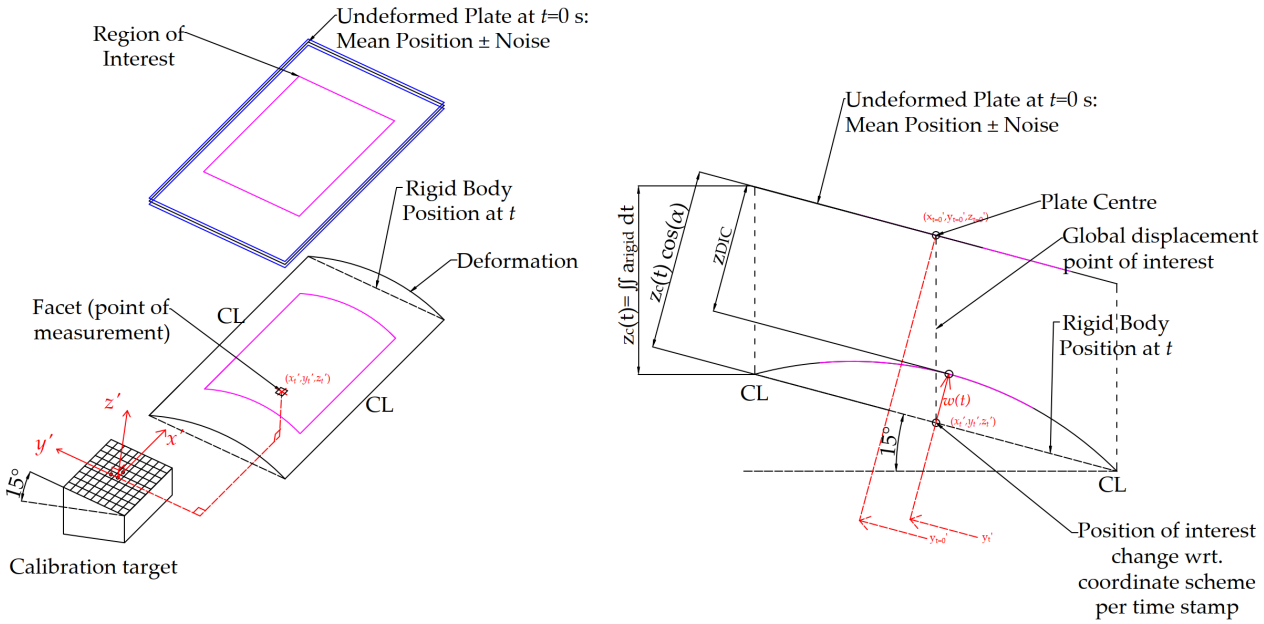

Figure 71: Calculation of local plate deformation from the 3D-DIC setup.

This section outlines how the local out-of-plane deformation of the plate, $w(x, y, t)$, is obtained by combining (i) rigid-body kinematics inferred from the accelerometer/light gate and (ii) 3D-Digital Image Correlation (DIC) fields conditioned in space and time.

The raw DIC output at each time t consists of facet measurements of out-of-plane displacement, denoted by $z_{\text{DIC}}(x_i', y_i', t)$. The following steps were adapted from an Pan et al. [68] to obtain a coherent displacement field to evaluate the local deformation $w(x', y', t)$ while appropriately handling the signal noise.

(1) Data Point Cloud to Grid Displacement Map: Facet samples are interpolated onto a Cartesian grid (x, y) using natural-neighbour or triangulation-based interpolation to obtain a dense displacement image. Let $W_{\text{meas}}(x, y, t)$ denote the interpolated data. Gaps in the data were filled by the nearest-neighbour interpolation, and non-finite values discarded. This step provides a well-defined field for spatial operations.

(2) Spatial regularisation: To attenuate pixel–scale noise while preserving amplitudes and smooth spatial features, a framewise quadratic regulariser adapted from that in Pan et al. [68] was applied to the gridded displacement $W_{\text{meas}}(x, y, t)$:

$$\min_{W} \lambda \sum_{(i,j)\in\Omega} \big(W_{i,j} - W_{\text{meas},i,j}\big)^2 + (1-\lambda) \sum_{(i,j)\in\Omega} \sum_{(p,q)\in\mathcal{N}(i,j)} \big(W_{i,j} - W_{p,q}\big)^2, \qquad 0 < \lambda < 1, \tag{67}$$

where Ω is the image grid and $\mathcal{N}(i,j) = \{(i\pm1, j), (i, j\pm1)\}$ is the four-neighbour stencil. The parameter λ balances data fidelity and smoothness: as $\lambda \to 1$, W approaches W_{meas}; as $\lambda \to 0$, W approaches a discrete harmonic (Laplacian-smoothed) field.

The regularised map is obtained by solving the following equation:

$$\big(\lambda I + (1-\lambda)L\big)\, \mathbf{w} = \lambda\, \mathbf{w}_{\text{meas}},$$

where L is the 4-neighbour discrete Laplacian. A Gauss–Seidel sweep on a Cartesian grid with reflective (zero-normal-gradient) boundaries is used. At each facet (i, j) the update

$$W_{i,j} \leftarrow \frac{\lambda\, W_{\text{meas},i,j} + (1-\lambda)\big(W_{i-1,j} + W_{i+1,j} + W_{i,j-1} + W_{i,j+1}\big)}{\lambda + 4(1-\lambda)},$$

is repeated until the relative ℓ_∞ change falls below a tolerance. This iteration enforces the pointwise optimality of (67) and converges to its unique minimiser.

(3) Pre-impact baseline and rigid-motion removal: A small static bias is removed by subtracting the pre-impact baseline

$$\bar{w}_0 = \frac{1}{N_0} \sum_{t\in\text{pre}} \text{median}\big\{W(x', y', t)\big\},$$

followed by removal of the rigid out-of-plane translation inferred from the accelerometer/light gate:

$$W_{\text{smoothened}}(x', y', t) \;=\; W(x', y', t) \;-\; z_c(t)\cos\alpha \;-\; \bar{w}_0. \tag{68}$$

(4) Reference frame and material-point sampling: A reference frame t_{ref} is first identified as the instant for which the facet coordinates are ≈ 0 matching the calibration plate position. This step is taken for consistency of position of interest. To evaluate the local deformation at a fixed material point as the plate moves downwards, the in-plane sampling abscissa is held fixed, $x_{\text{search}}(t) = x_{\text{ref}}$, while the y' ordinate is shifted by the rigid motion:

$$y_{\text{search}}(t) = y_{\text{ref}} + \text{sgn}\big(t - t_{\text{ref}}\big)\, \tan\alpha\, \big|z_c(t) - z_c(t_{\text{ref}})\big|. \tag{69}$$

This keeps the evaluation tied to the same material location on the wedge surface.

(5) Local displacement definition: The required local out-of-plane deformation is obtained by sampling the corrected displacement field at the convected coordinates:

$$w(x', y', t) \;=\; W_{\text{smoothened}}\big(x_{\text{search}}(t),\, y_{\text{search}}(t),\, t\big). \tag{70}$$

Appendix 4: Pressure Results

Table 16: Experimental pressure peak data with different aeration levels.

t_p (mm)	V_i (m/s)	β_g(%)	P_1 (Pa)	σ_{P_1} (Pa)	P_2 (Pa)	σ_{P_2} (Pa)	P_3 (Pa)	σ_{P_3} (Pa)
1	2	0	4.33×10^4	5.51×10^3	5.08×10^4	5.18×10^3	4.97×10^4	5.46×10^2
		1	4.48×10^4	2.04×10^3	5.45×10^4	9.01×10^1	4.45×10^4	2.58×10^2
		2	4.98×10^4	1.96×10^3	5.16×10^4	2.78×10^3	3.99×10^4	2.78×10^2
	3	0	8.78×10^4	2.62×10^3	9.32×10^4	2.74×10^3	8.07×10^4	4.02×10^3
		1	8.86×10^4	3.52×10^3	9.00×10^4	4.65×10^3	7.86×10^4	4.83×10^3
		2	8.02×10^4	5.01×10^3	8.71×10^4	2.62×10^3	6.92×10^4	4.06×10^3
	4	0	1.69×10^5	9.91×10^3	1.55×10^5	1.35×10^4	1.43×10^5	2.66×10^3
		1	1.92×10^5	6.17×10^3	1.34×10^5	1.11×10^4	1.43×10^5	6.42×10^3
		2	1.66×10^5	3.32×10^4	1.22×10^5	8.89×10^3	1.11×10^5	2.85×10^4
	5	0	2.98×10^5	7.44×10^4	2.09×10^5	1.49×10^4	1.91×10^5	4.68×10^3
		1	2.25×10^5	2.45×10^4	2.08×10^5	2.36×10^2	1.58×10^5	7.02×10^3
		2	2.50×10^5	3.15×10^4	1.95×10^5	1.15×10^4	1.65×10^5	9.64×10^3
2	2	0	3.52×10^4	4.63×10^3	5.29×10^4	5.26×10^2	4.34×10^4	2.33×10^3
		1	3.84×10^4	6.66×10^1	4.71×10^4	5.06×10^2	4.08×10^4	1.00×10^3
		2	3.28×10^4	5.84×10^3	3.72×10^4	1.84×10^3	3.10×10^4	2.16×10^3
	3	0	8.84×10^4	4.22×10^3	1.12×10^5	4.47×10^3	9.27×10^4	7.40×10^3
		1	9.09×10^4	4.36×10^3	1.12×10^5	2.78×10^3	8.64×10^4	3.71×10^3
		2	9.07×10^4	5.39×10^3	1.03×10^5	8.92×10^3	8.63×10^4	8.09×10^3
	4	0	1.64×10^5	4.98×10^3	2.00×10^5	3.63×10^3	1.61×10^5	2.38×10^3
		1	1.67×10^5	1.01×10^4	1.99×10^5	9.67×10^3	1.50×10^5	1.04×10^4
		2	1.61×10^5	7.09×10^3	1.71×10^5	1.14×10^4	1.18×10^5	1.17×10^4
	5	0	2.10×10^5	1.41×10^4	2.51×10^5	1.22×10^4	1.95×10^5	7.84×10^3
		1	2.12×10^5	1.12×10^4	2.34×10^5	9.45×10^3	1.93×10^5	9.77×10^3
		2	2.20×10^5	1.70×10^4	2.45×10^5	8.03×10^3	1.72×10^5	1.48×10^4
3	2	0	5.21×10^4	1.24×10^3	6.85×10^4	1.52×10^3	5.38×10^4	8.18×10^2
		1	5.03×10^4	1.14×10^3	5.38×10^4	4.56×10^3	4.69×10^4	8.21×10^3
		2	4.99×10^4	2.44×10^3	5.80×10^4	7.68×10^3	4.06×10^4	3.79×10^3
	4	0	1.56×10^5	2.51×10^3	1.89×10^5	7.15×10^3	1.50×10^5	2.92×10^3
		1	1.57×10^5	3.59×10^3	1.83×10^5	4.86×10^3	1.41×10^5	9.44×10^3
		2	1.59×10^5	9.73×10^3	1.59×10^5	3.53×10^3	1.27×10^5	1.89×10^4
	5	0	2.30×10^5	6.42×10^3	2.64×10^5	9.78×10^3	2.04×10^5	4.17×10^3
		1	2.23×10^5	1.71×10^4	2.59×10^5	6.04×10^3	1.79×10^5	1.08×10^4
		2	2.26×10^5	1.03×10^4	2.04×10^5	4.31×10^4	1.69×10^5	1.83×10^4

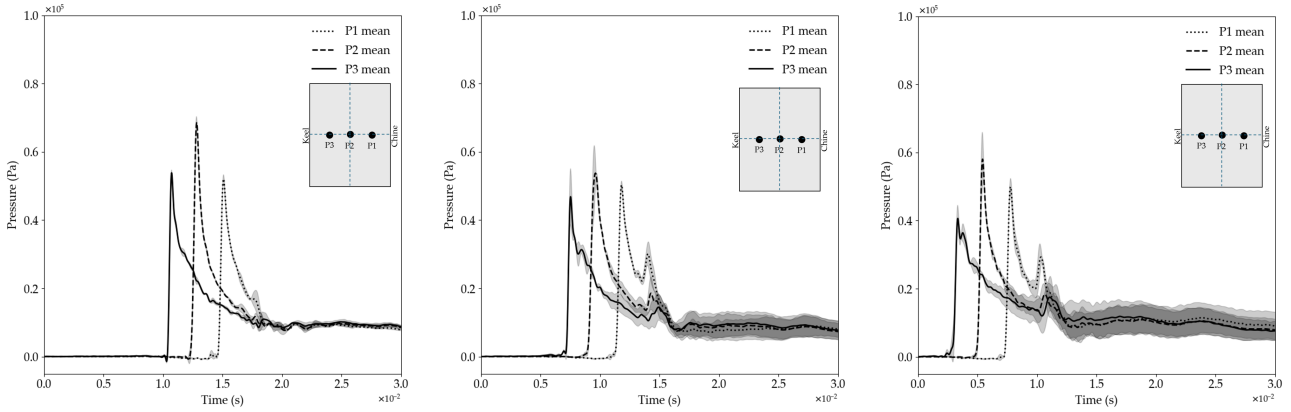

(a) $\beta_g = 0\%$ **(b)** $\beta_g = 1\%$ **(c)** $\beta_g = 2\%$

Figure 72: Pressure–time traces for the 3 mm plate at $V_i = 2$ m/s.

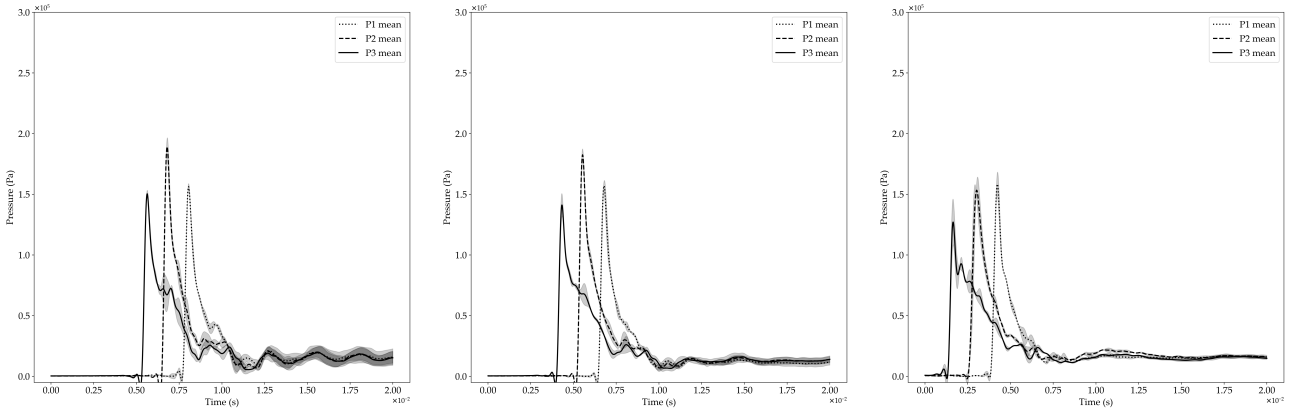

(a) $\beta_g = 0\%$ **(b)** $\beta_g = 1\%$ **(c)** $\beta_g = 2\%$

Figure 73: Pressure–time traces for the 3 mm plate at $V_i = 4$ m/s.

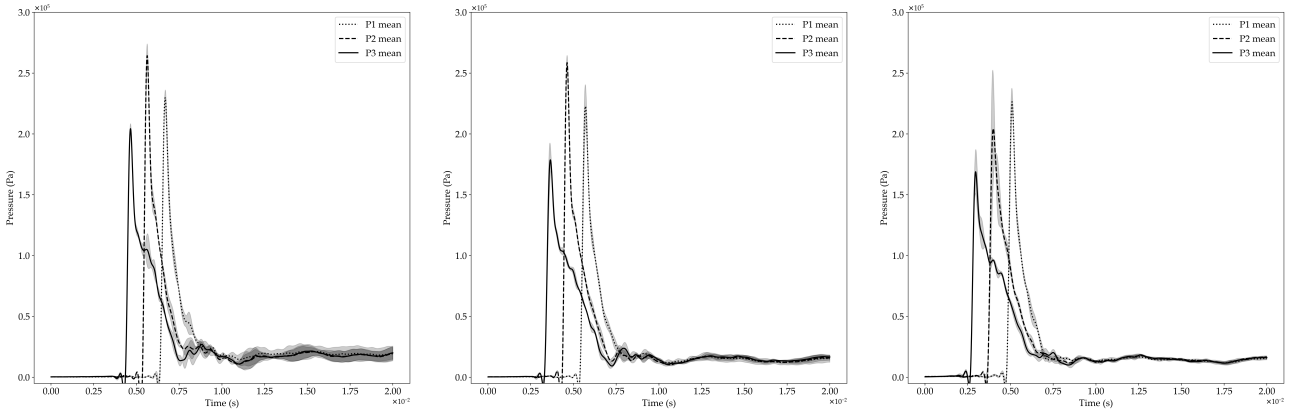

(a) $\beta_g = 0\%$ **(b)** $\beta_g = 1\%$ **(c)** $\beta_g = 2\%$

Figure 74: Pressure–time traces for the 3 mm plate at $V_i = 5$ m/s